Materials Design and Engineering for High Energy-Density Rechargeable Zinc-air Batteries

Dissertation

To attain the doctoral degree (Dr.rer.nat.)

of the Faculty of Forest Science and Forest Ecology

Georg-August-Universität Göttingen

Submitted by

Hua Zhang

born on the 20th December 1991 in P.R. China

Göttingen, April 2022

Thesis Committee

Prof. Dr. Kai Zhang, Abteilung Holztechnologie und Holzwerkstoffe, Georg-August-Universität Göttingen

Prof. Dr. Franc Meyer, Institut für Anorganische Chemie, Georg-August-Universität Göttingen

Dr. Minshen Zhu, Center for Materials, Architectures and Integration of Nanomembranes (MAIN), Chemnitz University of Technology

Member of the Examination Board

Reviewer:

Prof. Dr. Kai Zhang, Abteilung Holztechnologie und Holzwerkstoffe, Georg-August-Universität Göttingen

Second reviewer:

Prof. Dr. Franc Meyer, Institut für Anorganische Chemie, Georg-August-Universität Göttingen

Further members of the Examination Board:

Dr. Minshen Zhu, Center for Materials, Architectures and Integration of Nanomembranes (MAIN), Chemnitz University of Technology

Date of the oral examination: **12th April 2022**

Acknowledgements

I would first like to extend my deepest gratitude to my supervisor Prof. Dr. Kai Zhang, who gave me the opportunity to pursue my Ph.D. study in Germany, and who guided and encouraged me throughout my Ph.D. studies. Thanks for giving me the freedom and great support to pursue various research ideas. His enthusiasm and openness made me feel comfortable working on several different projects during my studies. Thanks for always being there when help was needed.

I would also like to thank my thesis committee member, Dr. Minshen Zhu, for providing additional guidance and support as well as the opportunity to work in his lab and collaborate with members of his research group. My sincere thanks should also go to another committee member, Prof. Dr. Franc Meyer, not only for his insightful comments and encouragement, but also for the valuable questions which incented me to widen my research from various perspectives.

I also want to dedicate my great thanks to my colleagues from Prof. Zhang's group, especially to Dr. Peiwen Liu, Dr. Heqin Huang, Dr. Huan Liu, Dr. Xiaojie Wang, Dr. Pascal Fuchs, Dr. Jiaxiu Wang, Dr. Stefanie Rühlicke, Dr. Shuang Wang, Ting Yang, Dan Xu, Wenbo Chen, Yang Yang, and Houjuan Qi for helping me with setting up experiments, giving me suggestions and feedback on my writing and presentations. Especially, my gratitude to my officemates in Büsgenweg 3, Bo Pang, Yawen Yao, Qingli Wang, and Kui Zeng for the stimulating discussions and the sleepless nights working together, and for all the jokes and fun we have had in the past four years. I would also like to thank secretaries and technicians from the wood faculty and our group, Dr. Gerhard Büttner, Brigitte Junge, Doris Waldmann, Martina Ackermann, Mirko Küppers, Eva Maichner, and Lukas Becker, for their continuous assistance with lab and administrative tasks.

Many thanks also go to the colleagues from the Energy group during my visiting period in IFW Dresden. In particular, Hongmei Tang, Qu Zhe, Jiang Qu, Yang Li, Xiaoyu Wang, Yi Liu, Chi Pang, Yaping Yan, Dr. Lixiang Liu, Dr. Yin Yin, Dr. Haiyun Dong, and Prof. Oliver G. Schmidt greatly helped me with my work. They also inspired me with many ideas and offered me knowledge from different perspectives.

Acknowledgements

Without their precious support, it would not be possible for me to conduct the research smoothly and finish my dissertation.

My sincere thanks also go to Dr. Loren B. Andreas, Dr. Rıza Dervişoğlu, Dr. Marcel C. Forster, Mr. Robert Koehler, Qiongqiong Lu, Dr. Xia Wang, Dr. Andrea Voß, Dr. Minghao Yu, and Prof. Dr. Christoph Gerhard, for their kind help in measurements supporting and fruitful discussion during my study.

Besides, I also want to thank the China Scholarship Council (CSC) and the finishing grant established by the German Exchange Service DAAD for the financial support. I would also like to express my sincere gratitude to Robert Grenzdörffer and Dr. Inga Mölder from the GFA office, for their help and patience over the past four years.

Last but not the least, I would like to give my greatest thanks to my wife-Dan Yao, and my family for their unconditional love, support, and company throughout my life.

Special thanks go to all the people I met, thanks for fulfilling my life!

Abstract

The growing demands for energy and the associated environmental pollution have sparked a great deal of interest in the development of clean energy technologies including fuel cells, metal-air batteries, supercapacitors, and hydrogen production. Among them, Zinc-air batteries (ZABs) are potential possibilities because of their low cost, high theoretical energy density, high-level safety, and environmental friendliness. In addition, zinc (Zn) is abundant in the environment and far less expensive than lithium metals. Thus, ZABs have been proposed as promising energy sources for grid-scale energy storage systems, as well as to replace or supplement lithium-ion batteries for next-generation electric vehicles. However, the development of rechargeable ZABs with high energy output and long lifespan remains a big challenge. For instance, a typical ZAB has a nominal cell voltage of 1.65 V, while most of the reported ZAB devices are capable of only 1.3 V or 1.4 V, which is much far below lithium-ion batteries. As a result, the energy density of ZABs is often lower than 1000 Wh kg^{-1}, far away from the predicted value of 1353 Wh kg^{-1} (excluding oxygen). In this regard, it is vital to investigate the synthesis of advanced materials and unique structural designs to further increase the operating voltage and energy density of ZABs. Besides, due to the rapid development of lightweight and portable smart electronic devices, the miniaturization of ZABs with high energy density is highly desirable but challenging. To this end, this thesis mainly focuses on the development of high-performance catalyst and separator materials accompanied by engineering and configuration design to fabricate high energy-output ZAB systems including miniaturization ZABs at the microscale and asymmetric-electrolyte ZABs with high voltage.

This work starts with an overview of the current status and scientific challenges of rechargeable ZABs. We first provide the operating principle and current configurations of ZABs, as well as their advantages and disadvantages. Then, the chemistry and major developments of key factors determining the performance of ZABs are conscientiously discussed, such as the Zn electrode, electrolytes, separators, and bifunctional air electrode. Briefly, an understanding of the issues hindering the electrochemical performance (e.g., efficiency, durability, and cycle-life) of ZABs are presented, which are mainly

caused by serious corrosion of the Zn electrode, unsatisfied bifunctional electrocatalysts, and the carbonate formation at the air cathode. Particularly, bifunctional electrocatalysts with high activity and durability on the air cathode are highly desirable, but they are challenging to create.

To address this issue, a Co^{2+}-coordinated porphyrin-based organic covalent framework (POF) was fabricated as an effective bifunctional electrocatalyst for ZABs by blending Co catalytic units into the POF and then hybridizing with conductive scaffold CNTs. Controlling the C-N coordination and the valence of Co units can regulate the bifunctional catalytic activity of the CoPOF@CNT catalyst. The CoPOF@CNT catalyst was then combined with a porous gas diffusion layer to create a high-performance carvable air cathode. In a poly(vinyl alcohol-co-poly(acrylic acid) hydrogel (PVA-co-PAA) electrolyte, the resultant air cathode demonstrated a high peak power density of 89 mW cm^{-2} and cycling durability for 110 cycles. Based on the high-performance carvable air cathode and highly adhesive PVA-co-PAA gel, a microimprint manufacture route was proposed for assembling an on-chip Zn-air rechargeable microbattery (μZAB), which avoids the difficulty of the catalyst integration on the chip at a target location. Impressively, the on-chip μZAB demonstrated a record-high volumetric power density of 570 mW cm^{-3} and a volumetric energy density of 413 Wh L^{-1}, about 3 times that of a commercial compact primary ZAB. The on-chip μZAB also reaches a lifecycle capacity of 4.5 mAh, which is roughly double that of the current commercial on-chip tiny lithium-ion battery. Our method closes the gap between advanced material production and on-chip integration, opening the door for high-performance on-chip ZABs.

After that, a quasi-solid-state ZAB with asymmetry-electrolyte (sAZAB) having both improved discharge voltage and substantially high energy density is presented. To achieve such a sAZAB, we proposed a combination strategy including the fabrication of a low-cost Zn^{2+}-conductive polyimide (ZnPI) separator and an efficient COF-based bifunctional electrocatalyst (CoPOF@MXene). The coordination of carbonyl groups and Zn^{2+} ions renders ZnPI with highly selective transportation of Zn^{2+} ions. In terms of the bifunctional catalyst, the synergistic interaction between Co-N_x active sites and highly conductive MXene substrate contributes to

high catalytic activity in an acidic medium. The sAZAB was then assembled by using a Zn anode, a CoPOF@MXene based air cathode, and a ZnPI separator sandwiched in between the alkaline anolyte (PAA-co-PVA + 6 M KOH) and the acidic catholyte (PAM-co-PVA gel + 3 M H_3PO_4). As a result, the as-fabricated sAZAB demonstrated excellent rate performance and cycling stability (~100 h), as well as a high open-circuit voltage of up to 2.1 V and an average round-trip efficiency of 70%. Moreover, to improve the battery performance at a high discharge of depth, an optimized sAZAB with the enhanced power density and specific capacity was further constructed by combining the (002)-textured Zn electrode and $Zn_3(PO_4)_2$-based catholyte. At a current density of 5 mA cm^{-2}, the optimized sAZAB coin cell achieves an impressive specific capacity of 742.4 mAh g_{Zn}^{-1} and an energy density of 1425.4 Wh kg_{Zn}^{-1}, outperforming reported conventional quasi-solid-state ZABs. At the cell level, an ultrahigh project energy density of 55.5 Wh kg_{cell}^{-1} is attainable, which has surpassed most of the reported works. This work closes the gap between fundamental research and the practical application of rechargeable ZABs, paving the way toward advances in materials science and structural engineering for electrochemical energy and storage systems.

The presented study is a monography work containing two publications. One of them has been already published and the other one is under submission. The general background and main topic blocks are presented in chapters 2-4.

Zusammenfassung

Der wachsende Energiebedarf und die damit verbundene Umweltverschmutzung haben ein großes Interesse an der Entwicklung sauberer Energietechnologien wie Brennstoffzellen, Metall-Luft-Batterien, Superkondensatoren und Wasserstofferzeugung geweckt. Zink-Luft-Batterien (ZABs) sind aufgrund ihrer geringen Kosten, hohen theoretischen Energiedichte, hohen Sicherheit und Umweltfreundlichkeit eine potenzielle Möglichkeit. Darüber hinaus ist Zink (Zn) in der Umwelt reichlich vorhanden und weitaus preiswerter als Lithiummetalle. Daher wurden ZABs als vielversprechende Energiequellen für Energiespeichersysteme im Netzbereich sowie als Ersatz oder Ergänzung von Lithium-Ionen-Batterien für Elektrofahrzeuge der nächsten Generation vorgeschlagen. Die Entwicklung von wiederaufladbaren ZABs mit hoher Energieleistung und langer Lebensdauer bleibt jedoch eine große Herausforderung. So hat eine typische ZAB eine nominale Zellenspannung von 1,65 V, während die meisten der gemeldeten ZAB-Bauteile nur 1,3 V oder 1,4 V liefern können, was weit unter den Lithium-Ionen-Batterien liegt. Infolgedessen liegt die Energiedichte von ZABs oft unter 1000 Wh kg^{-1}, weit entfernt von dem vorhergesagten Wert von 1353 Wh kg^{-1} (ohne Sauerstoff). In diesem Zusammenhang ist es wichtig, die Synthese fortschrittlicher Materialien und einzigartiger struktureller Designs zu untersuchen, um die Betriebsspannung und Energiedichte von ZABs weiter zu erhöhen. Aufgrund der raschen Entwicklung leichter und tragbarer elektronischer Geräte ist die Miniaturisierung von ZABs mit hoher Energiedichte sehr wünschenswert, aber auch eine Herausforderung. Aus diesem Grund konzentriert sich diese Arbeit hauptsächlich auf die Entwicklung hochleistungsfähiger Katalysator- und Separatormaterialien in Verbindung mit der Konstruktion und dem Konfigurationsdesign zur Herstellung von ZAB-Systemen mit hoher Energiedichte, einschließlich Miniaturisierungs-ZABs im Mikrobereich und asymmetrischen Elektrolyt-ZABs mit hoher Spannung.

Diese Arbeit beginnt mit einem Überblick über den aktuellen Stand und die wissenschaftlichen Herausforderungen von wiederaufladbaren ZABs. Zunächst werden das Funktionsprinzip und die aktuellen Konfigurationen von ZABs sowie ihre Vor- und Nachteile beschrieben. Anschließend werden die Chemie und die wichtigsten Entwicklungen der Schlüsselfaktoren, die die Leistung von ZABs

bestimmen, gewissenhaft erörtert, wie z. B. die Zn-Elektrode, Elektrolyte, Separatoren und die bifunktionale Luftelektrode. Kurz gesagt, werden die Probleme, die die elektrochemische Leistung (z.B. Effizienz, Haltbarkeit und Zykluslebensdauer) von ZABs behindern, vorgestellt, die hauptsächlich durch schwere Korrosion der Zn-Elektrode, unzureichende bifunktionale Elektrokatalysatoren und die Karbonatbildung an der Luftkathode verursacht werden. Insbesondere bifunktionale Elektrokatalysatoren mit hoher Aktivität und Haltbarkeit an der Luftkathode sind sehr wünschenswert, aber schwierig herzustellen.

Um dieses Problem anzugehen, wurde ein Co^{2+}-koordiniertes organisches kovalentes Gerüst (POF) auf Porphyrinbasis als effektiver bifunktioneller Elektrokatalysator für ZABs hergestellt, indem katalytische Co-Einheiten in das POF gemischt und dann mit leitfähigen CNTs hybridisiert wurden. Durch die Steuerung der C-N-Koordination und der Wertigkeit der Co-Einheiten kann die bifunktionale katalytische Aktivität des CoPOF@CNT-Katalysators reguliert werden. Der CoPOF@CNT-Katalysator wurde dann mit einer porösen Gasdiffusionsschicht kombiniert, um eine leistungsstarke, schnitzbare Luftkathode zu schaffen. In einem Poly(vinylalkohol-co-poly(acrylsäure)-Hydrogel (PVA-co-PAA)-Elektrolyt wies die so entstandene Luftkathode eine hohe Spitzenleistungsdichte von 89 mW cm^{-2} und eine Zyklenfestigkeit von 110 Zyklen auf. Auf der Grundlage der leistungsstarken schnitzbaren Luftkathode und des stark haftenden PVA-co-PAA-Gels wurde ein Mikrodruck-Herstellungsverfahren für die Montage einer wiederaufladbaren Zn-Luft-Mikrobatterie (μZAB) auf dem Chip vorgeschlagen, das die Schwierigkeiten bei der Integration des Katalysators auf dem Chip an einer bestimmten Stelle vermeidet. Beeindruckend ist, dass die On-Chip-μZAB eine rekordverdächtige volumetrische Leistungsdichte von 570 mW cm^{-3} und eine volumetrische Energiedichte von 413 Wh L^{-1} aufweist, was etwa dem Dreifachen einer kommerziellen kompakten Primär-ZAB entspricht. Die On-Chip-μZAB erreicht außerdem eine Lebenszykluskapazität von 4,5 mAh, was etwa doppelt so hoch ist wie die der derzeitigen kommerziellen winzigen On-Chip-Lithium-Ionen-Batterie. Unsere Methode schließt die Lücke zwischen fortschrittlicher Materialherstellung und On-Chip-Integration und öffnet die Tür für leistungsstarke On-Chip-ZABs.

Danach wird eine Quasi-Festkörper-ZAB mit Asymmetrie-Elektrolyt (sAZAB) vorgestellt, die sowohl eine verbesserte Entladungsspannung als auch eine wesentlich höhere Energiedichte aufweist. Um eine solche sAZAB zu erreichen, haben wir eine Kombinationsstrategie vorgeschlagen, die die Herstellung eines kostengünstigen Zn^{2+}-leitenden Polyimid-Separators (ZnPI) und eines effizienten bifunktionalen Elektrokatalysators auf COF-Basis (CoPOF@MXen) umfasst. Die Koordination von Carbonylgruppen und Zn^{2+}-Ionen macht ZnPI hochselektiv für den Transport von Zn^{2+}-Ionen. Beim bifunktionalen Katalysator trägt die synergistische Wechselwirkung zwischen den aktiven Co-Nx-Stellen und dem hochleitfähigen MXen-Substrat zu einer hohen katalytischen Aktivität in einem sauren Medium bei. Der sAZAB wurde dann unter Verwendung einer Zn-Anode, einer Luftkathode auf CoPOF@MXen-Basis und eines ZnPI-Separators, der zwischen dem alkalischen Anolyten (PAA-co-PVA + 6 M KOH) und dem sauren Katholyten (PAM-co-PVA-Gel + 3 M H_3PO_4) liegt, zusammengesetzt. Im Ergebnis zeigte die so hergestellte sAZAB eine hervorragende Ratenleistung und Zyklenstabilität (~100 h) sowie eine hohe Leerlaufspannung von bis zu 2,1 V und eine durchschnittliche Round-Trip-Effizienz von 70%. Um die Batterieleistung bei einer hohen Entladetiefe zu verbessern, wurde außerdem eine optimierte sAZAB mit erhöhter Leistungsdichte und spezifischer Kapazität konstruiert, indem die (002)-texturierte Zn-Elektrode und der $Zn_3(PO_4)_2$-basierte Katholyt kombiniert wurden. Bei einer Stromdichte von 5 mA cm^{-2} erreicht die optimierte sAZAB-Knopfzelle eine beeindruckende spezifische Kapazität von 742,4 mAh g_{Zn}^{-1} und eine Energiedichte von 1425,4 Wh kg_{Zn}^{-1} und übertrifft damit berichtete konventionelle Quasi-Festkörper-ZABs. Auf Zellebene ist eine ultrahohe Projekt-Energiedichte von 55,5 Wh kg_{cell}^{-1} erreichbar, die die meisten der bisher veröffentlichten Arbeiten übertrifft. Diese Arbeit schließt die Lücke zwischen der Grundlagenforschung und der praktischen Anwendung von wiederaufladbaren ZABs und ebnet den Weg zu Fortschritten in der Materialwissenschaft und Strukturtechnik für elektrochemische Energie- und Speichersysteme.

Bei der vorliegenden Studie handelt es sich um eine Monografie, die zwei Veröffentlichungen umfasst. Eine davon wurde bereits veröffentlicht, die andere ist in Vorbereitung. Der allgemeine Hintergrund und die Hauptthemenblöcke werden in den Kapiteln 2-4 vorgestellt.

Table of Contents

Abbreviations

EES	Rechargeable energy storage
MABs	Metal-air batteries
ZABs	Zn-air batteries
2D	Two dimensional
3D	Three dimensional
HER	Hydrogen evolution reaction
ORR	Oxygen reduction reaction
OER	Oxygen evaluation reaction
SHE	Standard hydrogen electrode
RHE	Reversible hydrogen electrode
COFs	Covalent organic frameworks
EV	Electrical vehicle
ZAFCs	Zn-air fuel cells
GDL	Gas diffusion layer
CNTs	Carbon nanotubes
POFs	Porphyrin-based organic covalent framework
CoPOF	Cobalt embedded POF
PVA	Poly(vinyl alcohol)
PAA	Poly(acrylic acid)
PAM	Polyacrylamide
μZAB	Zn-air rechargeable microbattery
LSV	Linear sweep voltammetry
RRDE	Rotating ring-disk electrode
SEM	Scanning electron microscopy
TEM	Transmission electron microscope
EDS	Energy-dispersive X-ray spectroscopy
XPS	X-ray photoelectron spectroscopy
XRD	X-ray diffraction
FTIR	Fourier-transform infrared spectroscopy

Chapter 1: Motivation and Scope of This Work

1.1 Motivation

The shift from fossil fuels to clean renewable energy has been expedited by rapidly rising energy needs and increased awareness of climate change.[1-5] Although solar and mechanical energy may be captured and converted to electricity, they are constrained to specific areas and time periods, making widespread use within the global energy mix a difficulty.[6-9] In this regard, the development of electrically rechargeable energy storage (EES) technologies, specifically batteries, is of vital importance towards the integration effectively. Rechargeable batteries have been known for storing chemical energy and converting them to electrical power on demand. Lithium-ion batteries (LIBs) are currently dominating the rechargeable battery industry, with a wide range of uses in our everyday lives, including computers, cellphones, electric cars, and smart grids.[10-12] However, the restricted energy density, high cost, safety difficulties arising from Li flammability and organic electrolytes, and a future Li supply crisis are all obstacles to the ongoing development of LIBs.[13-15] As a result, developing more environmentally friendly, efficient, and safe rechargeable battery technologies is extremely desirable.[16, 17]

Because of their low cost and high energy density, metal-air batteries (MABs), which are based on the coupled electrochemical processes of metal anodes and oxygen-consuming cathodes, have received a lot of interest as emerging EES technologies.[18-20] During the past years, several metals have been utilized to prepare rechargeable MABs, including zinc (Zn), magnesium (Mg), aluminium (Al), iron (Fe), and alkaline metals such as Li, sodium (Na), and potassium (K).[21-24] The theoretical gravimetric/volumetric energy density and cell voltage of various MABs are compared in Figure 1.1.[25] Li-air batteries can theoretically deliver the highest energy density (5928 Wh kg^{-1}) and high cell voltage (2.96 V) due to the lightweight nature of Li. However, all MABs using alkaline metals suffer from safety issues because they are highly sensitive to water and oxygen.[18] Aqueous Al- and Mg-air batteries can match the energy densities of Li-air batteries.[21] However, due to their low reduction potentials (e.g.,

-2.372 V for Mg and -1.662 V for Al), they have the problems of fast self-discharge via hydrogen evolution reaction (HER), resulting in severe parasitic corrosion on Mg and Al electrode surfaces.[21] Furthermore, Mg and Al electrodeposition in aqueous electrolytes is thermodynamically impossible, limiting their broad use. Zn-air batteries (ZABs) and Fe-air, on the other hand, are rechargeable and have great stability when used in an aqueous media.[26] Owing to its greater volumetric energy density (6136 Wh L^{-1}) and cell voltage (1.66 V), ZABs appear to be more viable for large-scale applications than Fe-air batteries.

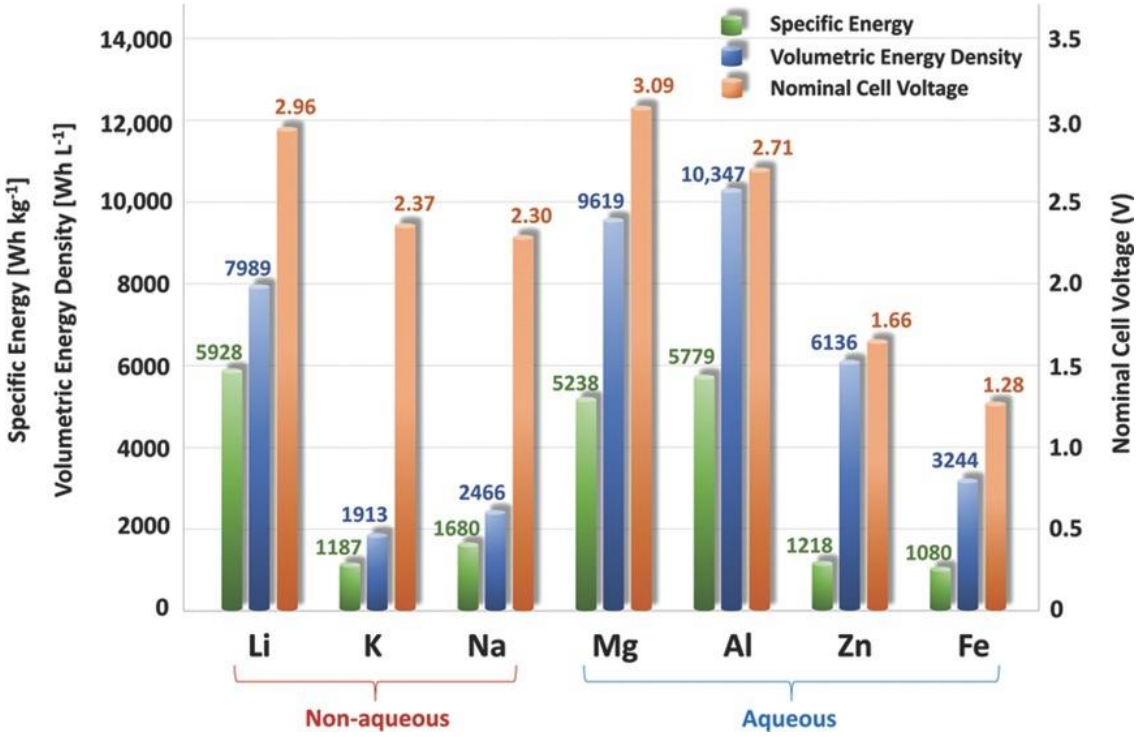

Figure 1.1. Comparison of various MAB technologies in terms of their theoretical specific energies, volumetric energy densities, and cell voltages. Reproduced with permission.[25]

The primary ZABs have already been commercialized and are widely used in the medical and telecommunication areas, including as hearing aids, navigation lights, and railway signaling systems. [27, 28] For broadening applications, it is necessary to upgrade primary ZABs into rechargeable ones that can be recycled for thousands of cycles. Although the development of practically rechargeable ZABs has achieved great progress, it is still a long way to their large-scale applications due to the low power-

output capability. Current ZABs, for example, operate at roughly 1.0-1.2 V, much below the theoretical value of 1.65 V. At the same time, a charging potential of over 2 V is often in demand to revert electrochemical reactions during cycling, which results in low round-up efficiency of less than 60%.[29] This low energy efficiency mainly stems from the following issues 1) air electrodes suffer from insufficient catalytic activities, sluggish kinetics for the oxygen redox reactions, and the formation of solid carbonate deposit; 2) the Zn electrode faces the problems of dendrite growth, passivation, and severe corrosion, leading to a significant capacity decrease. Therefore, developing advanced electrode materials and battery structural designs are important for the practical applications of rechargeable ZABs.

The oxygen reduction reaction (ORR) and oxygen evaluation reaction (OER) activities of oxygen catalytic materials at the air cathode are particularly important in determining the battery performance. In this regard, Pt- and/or Ru-based noble metals or their oxides (e.g., RuO_2 and IrO_2) are current state-of-the-art electrocatalysts.[30, 31] For instance, Pt is the best ORR electrocatalyst in both alkaline and acid electrolytes, whereas RuO_2 and IrO_2 have the best OER activity.[32, 33] However, the high cost, inherent scarcity, and poor long-term durability of these noble-based electrocatalysts severely limit their widespread utilization. As a result, there has been a lot of interest in developing low-cost, high-efficiency electrocatalysts made from earth-abundant elements to replace noble-metal-based catalysts.[30-33] In the past decades, tremendous efforts and great progress have been made in the development of non-noble-metal electrocatalysts, including transition-metal-based materials, such as layered metal hydroxides,[34-38] perovskite oxides,[39-43] transition metal oxides/nitrides/borides,[44-51] metal alloys,[52-55] and metal-free heteroatom-doped carbon nanomaterials (e.g., heteroatom-doped graphene,[56-58] doped carbon nanotubes (CNTs),[59-61] porous nanocarbon[62-64]). Although most of them hold great promise in energy-conversion reactions, only a few other electrocatalysts can outperform noble-metal-based catalysts in terms of electrochemical performance. Particularly, a deep understanding of the catalytic processes and mechanism is still lacking, as well as the real active sites are poorly recognized. For example, heteroatom-doped metal-free carbon compounds have shown high electrocatalytic activity equivalent to noble metals. However, these materials are often generated using standard high-

temperature carbonization or heteroatom doping techniques, making it difficult to precisely regulate the density of active sites and establish the veracity of active centers.[65]

In this regard, covalent organic frameworks (COFs) linked by strong covalent bonds have presented the significant potential for new-generation energy-related electrocatalysis, such as highly crystalline materials with large surface area and tunable pore sizes, allowing for devolving highly ordered network structures with excellent mass transportability.[66] Furthermore, using the right building blocks, linkage motifs, and synthesis routes, COFs can be used to design precisely controllable structures with desirable components and functions, making them an ideal platform for developing efficient electrocatalysts with predictable properties at the molecular level.[67-69] By selecting the right building blocks, linking motifs, and synthesis methods, substantial progress has recently been achieved in the creation of efficient COF-based electrocatalysis.[66] Xiang et al., for example, synthesized a class of 2D COFs with metal (e.g., Fe, Co, Mn) macrocycles and employed them as metal-free electrocatalysts for ORR catalysis.[68, 69] In both alkaline and acid media, these COF-based catalysts shown high catalytic activity, long-term stability, and away from any methanol-crossover/CO-poisoning effects. The COFs also include a lot of porous structures with open channels for effective gas permeability and ion transportation, which is beneficial for catalyzing ORR and OER. Furthermore, COFs can hybridize with conductive scaffolds (e.g., 1D CNTs, 2D MXene) through intermolecular interactions, resulting in efficient conductive channels and adequate effective surface area, enhancing their catalytic activity even further. All these merits render COFs more amazing catalytic characteristics than a simple blend of catalytic and conductive host materials.

1.2 Thesis Objectives and Structures

With the aim of improving the practical energy density of ZABs for extensive applications, the main objectives of this dissertation include (i) the evaluation of scientific and technical challenges for the practical applications and commercialization of ZABs, (ii) the development of advanced COF-based electrocatalyst and separator materials that stably operate in an alkaline and/or acidic electrolyte, to produce an electrically rechargeable ZABs with excellent durability and highly energy-dense, and (iii)

corresponding engineering design of quasi-solid-state on-chip ZABs and high-voltage asymmetric-electrolyte ZABs through combining these materials. As a result, in this thesis, we focused on the design and characterization of high-performance ZAB electrode and separator materials, as well as their physical, chemical, and electrochemical features. The integration of these materials accompanied by engineering techniques and structural design were then presented to fabricate high-energy-output ZAB systems.

This thesis includes five chapters, in which **Chapter 1** describes the thesis' motivation and scope. **Chapter 2** provides an overview of the history, scientific principles, and problems of rechargeable ZABs, with a special focus on the material research paths necessary to develop long-lasting, high-energy-density ZABs. **Chapter 3** combines a high-performance carvable COF-based air electrode with a microimprint manufacturing route to create an on-chip zinc-air rechargeable microbattery, bridging a long-standing gap between advanced material synthesis and on-chip processing and opening the door for high-performance on-chip ZABs. **Chapter 4** details an asymmetric-electrolyte ZAB constructed with a polyimide-based Zn^{2+}-conductive separator and a highly active Co^{2+}-coordinated COF electrocatalyst supported by a layered Ti_3C_2 MXene. The assembled battery shows enhanced operating voltage and energy density outperforming most of the conventional alkaline ZABs. Ultimately, **Chapter 5** summarizes the major findings of this thesis and suggests some future research possibilities for developing high energy density rechargeable ZABs.

Chapter 2: Fundamentals of Rechargeable Zn-air Batteries

2.1 History

Zn-air batteries (ZABs) are well-known as one of the oldest and most economically feasible battery technologies available. In the 19th century, significant research activities devoted to the precursors of ZABs including both Zn-carbon batteries and fuel cells were gradually and constantly conducted. The concept was first proposed by Smee in 1840 based on the work by William Robert Grove and Robert Bunsen.[70] Grove invented the Grove Cell in 1839, which consisted of Zn and Pt electrodes in diluted and mixed sulfuric and nitric acid solutions separated by a ceramic porous-pot structure. One year later, Bunsen improved the Grove Cell by using a cheaper carbon cathode to replace the Pt electrode.[70] Unfortunately, both the Grove and Bunsen cells suffered from the problem of evolving the noxious gas NO_2 during the discharging process. Notably, Grove was also at work developing the first H_2-O_2 fuel cell (Figure 2.1) between 1838 and 1842, paving the way to develop the air electrode.[71, 72]

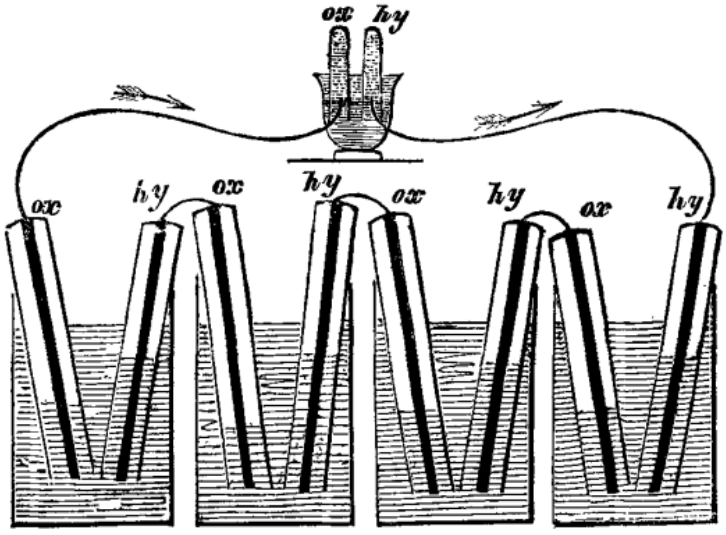

Figure 2.1. Schematic of "gaseous voltaic battery" developed by William Robert Grove, which was widely recognized as the first H_2-O_2 fuel cell.[71,72]

In 1866, Georges Leclanché introduced manganese dioxide (MnO_2) into the carbon cathode and invented the Leclanché cell consisting of a Zn alloy anode, a MnO_2 and carbon composite cathode, and an ammonium chloride electrolyte.[73] The Leclanché cell made great success in powering early telegraphs and telephones. At that time, an enhanced performance was observed when the jar was only half-full of electrolytes. Coincidentally, Leclanché exposed the cathode to the air and then created a special environment with a three-phase interface (e.g., gas, liquid, and solid), creating the prototype of the first primary Zn-air battery.[74] In 1878, Frenchman L. Maiche used a platinized carbon electrode to replace the MnO_2 electrode, truly realizing the first widely recognized Zn-air battery.[74, 75] Then, a true gas diffusion electrode was presented in a so-called Walker-Wilkins battery made of porous carbon black and nickel current collector. In 1932, the first commercial products of primary ZABs were patented and introduced to the market by George Heise and Erwin Schumacher.[76, 77] In this invention, Heise and Schumacher used the wax on the surface of the porous air cathode, successfully avoiding the flooding issue. Since then, the primary ZABs have become widespread and are commonly employed as "button cells" in timepieces and railway signal lights because of their high energy density of more than 440 Wh/kg and long lifespan of over 3 years when sealed. Initially, the market for ZABs only comprised low current industrial electronics such as railway signals and navigational buoys. Beginning in the 1960s, significant advances have been achieved in gas diffusion electrodes, paving the way for ZABs to new applications in medical and telecommunication. In 1977, the primary ZABs were further integrated into pagers and hearing aids, which eventually emerged as the main power source and dominated the market for forty years. The global market for primary ZABs exceeded $3 billion in 2017.[75]

Since the 1960s, extensive efforts have been devoted to developing ZABs for electric vehicle (EV) applications. For example, ZABs were used to power two concept automobiles shown by Gulf General Atomics (a mini-moke jeep with a 20-kWh battery) and General Motors (a 35-kWh battery). Regrettably, due to technological limits, they were never further developed. Pilot EV experiments using mechanically rechargeable Zn-air fuel cells (ZAFCs) have been running since the 1990s, with recycled zinc pastes physically removed and replaced with new ones. The Israeli business Electric Fuel devised

a unique Zn-air storage concept for solar energy in 1990 (Figure 2.2). In 1991, a Honda CRX powered by a 45-kWh ZAB won a 200-kilometer race for electric automobiles, attaining a top speed of 111 km/h while only utilizing 66% of its initial capacity.[78] The German company ZOXY exhibited a ZAB-powered vehicle in Utah in the end of the 1990s, with maximum mileages of 760 km at temperatures below freezing and 1650 km at higher temperatures.[79] In 1995, 64 Deutsche Post vehicles were outfitted with ZAFCs that could be recharged manually.[80, 81] Unfortunately, this concept was never further pursued because to the expensive expense of building a network of zinc replenishment stations.

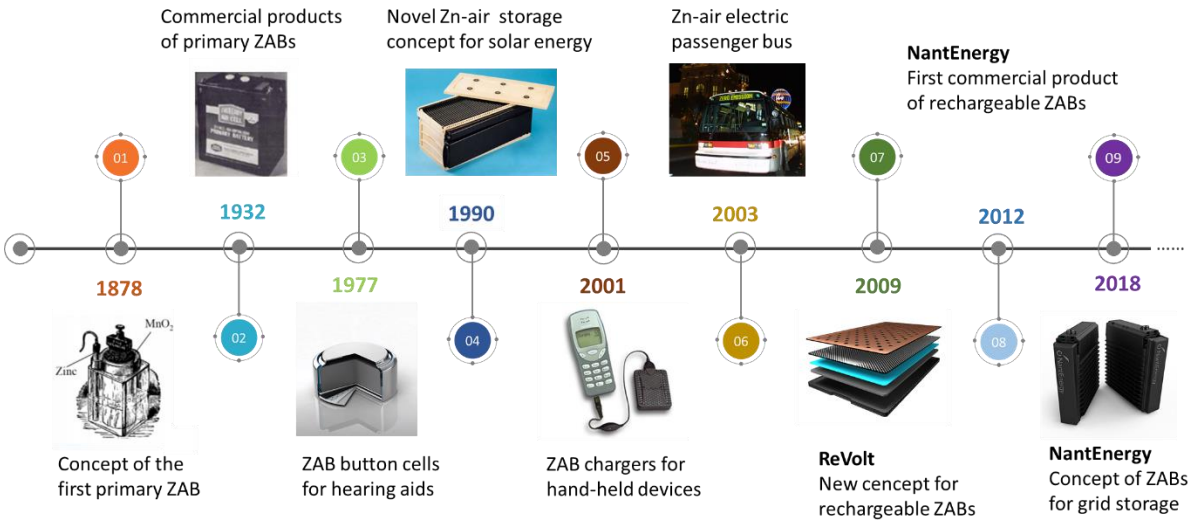

Figure 2.2. Roadmap and significant progress for the development of ZAB technology.

Even though the feasibility of ZABs for EV applications were demonstrated by these aforementioned concept projects, the scale-up commercialization has yet to be adopted. The main challenges include a shortage of supplying and processing Zn fuel, limited battery lifetime, and low power output. At the end of the 20th century, high-performance and affordable Li-ion batteries raise, which eclipsed ZABs and eventually sapped researchers' enthusiasm. As the future material supply of LIBs becomes uncertain, the development of advanced electrode materials and the huge energy demand have reignited great interest in rechargeable ZABs in both academia and industry. In 2010, the United States Department of Energy initiated an ARPA-E project for the development of electrically rechargeable ZABs. Several companies including Eos Energy Storage, ZincNyx Energy Solutions, and Fluidic

Energy attempted to commercialize ZABs for stationary storage applications and did excellent work. For example, EOS Energy Storage created an Aurora product with a 1 MW/4 MWh Zn-air battery for utility-scale grid storage that costs as little as 160 US dollars per kWh.[25] Fluidic Energy offered approximately 250 MWh ZABs for storing photovoltaic solar energy in 500 distant settlements in collaboration with Caterpillar and Indonesia's state utility. In 2012, the first commercially rechargeable ZABs were achieved by NantEnergy (formerly Fluidic Energy). Despite the early start, rechargeable ZABs are still far from fulfilling their full potential due to their limited energy densities (~35 Wh kg^{-1} as of 2017).[82]

Rechargeable ZABs are one of the possible alternatives for energy conversion and storage technologies as the need for flexible and wearable electronic devices grows. The development of rechargeable ZABs for power sources, on the other hand, is still in its early stages. As a result, much effort has gone into developing rechargeable ZABs with exceptional electrochemical performance. The future of rechargeable ZABs for both stationary and mobile applications is promising, but technical hurdles remain.[18] The main challenges are the relatively low durability and energy density of rechargeable ZABs when practical applications are considered. It is critical in this case to increase the cycle stability of bifunctional oxygen catalysts and zinc electrodes while retaining high operating voltage and energy density, resulting in very energy-dense rechargeable ZABs with a long lifetime.[83-85] In the following sections, we reviewed the battery configuration and operating mechanism of alkaline ZABs, as well as some of the main challenges influencing the battery performance. To improve the service life of rechargeable ZABs, it is of great importance to reduce or eliminate carbon in the air electrodes,[86] since carbon-based materials tend to be corroded under the high concentration of alkaline electrolytes.[87] To overcome these issues, commercial rechargeable ZABs need circulating electrolytes, electrolyte filtration, or multi-electrode designs to maintain long-term performance, which increases complexity and limits the system-level energy density.[88-91] Therefore, this chapter discusses the special problems and techniques for developing electrodes for highly energy-dense rechargeable ZABs.

2.2 Battery Configuration and Operating Principle

Typically, a ZAB comprises the following four main components including an air cathode, an aqueous KOH electrolyte, a separator, and a Zn metal anode. The air cathode, also known as a bifunctional air electrode (BAE), is made up of a porous gas diffusion layer (GDL) and a bifunctional catalyst layer, which is in charge of both the ORR and OER. The GDL functions as open channels for air permeation and as porous substrates for loading catalytic active materials, which surfer wettability has a great impact on determining the performance of the air electrode. The hydrophilic and hydrophobic properties of the GDL can be tuned using polymer binders (e.g., polytetrafluoroethylene (PTFE)), thus forming a liquid-gas-solid three-phase interface between the electrolyte, air, and catalyst.

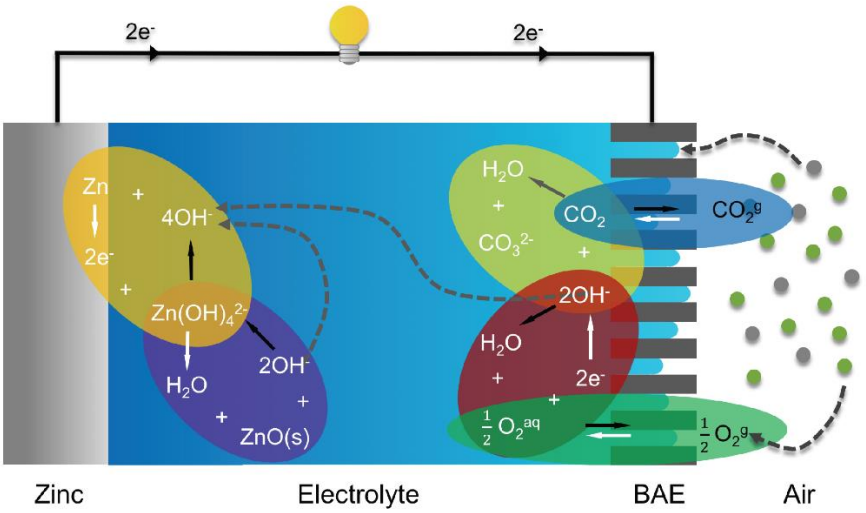

Figure 2.3. Working mechanism of a typical alkaline ZAB. The white and black arrows indicate electrochemical reactions during discharging and charging processes. Reproduced from with permission.[92]

Figure 2.3 illustrates the operating principle of a typical alkaline ZAB. During discharging, the ZAB acts as a power generator via the electrochemical interaction of the Zn metal with the endless oxygen from the air. The oxygen spreads into the porous BAE and is then converted to hydroxyl ions by the ORR. Then, the resultant hydroxyl ions in the electrolyte migrate to the Zn anode, where they combine with Zn ions to produce soluble zincate ions ($Zn(OH)_4^{2-}$). As the reaction proceeds, the solubility of

$Zn(OH)_4^{2-}$ will reach its limit value, culminating in the precipitation of ZnO on the Zn anode's surface. Upon charging, the ZAB is responsible for storing energy via the OER that occurs at the air cathode, which is accompanied by the deposition of Zn. The elementary and overall reactions for an ideal alkaline ZAB are summarized as follows.

The air cathode reaction:

$$O_2 + 2H_2O + 4e^- \leftrightarrow 4OH^-,\ E = 0.40\ V\ vs.\ SHE \quad (2.1)$$

The Zn anode reactions:

$$Zn \rightarrow Zn^{2+} + 2e^- \quad (2.2)$$

$$Zn^{2+} + 4OH^- \rightarrow Zn(OH)_4^{2-} \quad (2.3)$$

$$Zn(OH)_4^{2-} \rightarrow ZnO + H_2O + 2OH^- \quad (2.4)$$

Total:

$$Zn + 2OH^- \rightarrow ZnO + H_2O + 2e^-,\ E = -1.25\ V\ vs.\ SHE \quad (2.5)$$

The overall reaction:

$$2Zn + O_2 \leftrightarrow 2ZnO,\ E = 1.65\ V\ vs.\ SHE \quad (2.6)$$

Table 2.1 presents the standard thermodynamic values of the main species during the operation of alkaline ZABs. Thermodynamically, the coupled redox reaction of a typical alkaline ZAB can yield a nominal cell voltage of 1.65 V versus a standard hydrogen electrode (SHE). Based on the generalized Nernst equation, the theoretical specific capacity (Q), specific energy (N_{mass}) and energy density (N_{vol}) of the ZAB can be calculated as follows:

$$Q = \frac{nF}{M_{Zn}} = \frac{2*96500/3.6}{65.38} = 820\ mAh\ g_{Zn}^{-1} \quad (2.7)$$

$$N_{mass} = \frac{U_{OCV}*Q*M_{Zn}}{M_{ZnO}} = \frac{1.65*820*65.38}{81.38} = 1086\ Wh\ kg_{ZnO}^{-1} \quad (2.8)$$

$$N_{vol} = N_{mass} * \rho_{ZnO} = 1086 * 5.61 = 6093\ Wh\ L_{ZnO}^{-1} \quad (2.9)$$

Consequently, the ZAB can achieve a high theoretical energy density ($6093\ \mathrm{Wh\ L}_{ZnO}^{-1}$) and high specific energy ($1086\ \mathrm{Wh\ kg}_{ZnO}^{-1}$). Unfortunately, the practical working voltage is often below 1.2 V because of the internal loss of the battery and sluggish air-electrode reactions. A charging voltage of 2 V or greater is frequently necessary to reverse electrochemical processes. Thus, most of the current rechargeable ZABs have a low round-up efficiency of less than 60%, which can be ascribed to the following issues: i) the lack of efficient bifunctional oxygen electrocatalysts to effectively catalyze the ORR/OER on air-electrodes; ii) the severe self-corrosion of Zn electrodes caused by the parasitic hydrogen evolution reaction:

$$\mathrm{Zn} + 2\mathrm{H_2O} \rightarrow \mathrm{Zn(OH)_2} + \mathrm{H_2} \tag{2.10}$$

iii) the dendrite formation and shape change caused by non-uniform dissolution and deposition of Zn during battery charging; iv) the persistent ingression of CO_2 from air produces insoluble carbonate blocking the air channels in the GDL.

Table 2.1 Standard thermodynamic values of the major species in a typical alkaline ZAB. [93]

Species	Physical state	Molar mass (g mol^{-1})	Density (g cm^{-3})	$\Delta_f H^0$ (kJ mol^{-1})	$\Delta_f G^0$ (kJ mol^{-1})	S^0 (J mol^{-1} k^{-1})
Zn	s	65.38	7.14	0	0	41.63
Zn^{2+}	aq	65.38	---	-153.39	-147.1	109.8
$Zn(OH)_4^{2-}$	aq	133.43	---	---	-858.52	---
ZnO	s	81.38	5.61	-350.46	-320.52	43.65
O_2	l	31.9988	---	-11.7	16.4	110.9
H_2O	aq	18.02	1	-285.83	-237.14	69.95
OH^-	aq	17.01	---	-230.015	-157.28	-10.9
H^+	aq	1.01	---	0	0	0

Generally, rechargeable ZABs can be categorized into three varieties based on their configurations: conventional planar ZABs, Zn-air flow batteries, and flexible ZABs (Figure 2.4). The conventional planar configuration has a sandwich structure, which was originally designed for primary ZABs. This configuration allows for the simple assembly using plastic plates and gaskets, and quick disassembly of the electrode materials and electrolytes to be further investigated.[94-96] Due to these advantages, this configuration is currently the most widely used one in academic activities. Although current rechargeable ZABs with traditional planar configurations have not yet entered the commercial market, they hold great potential as promising candidates for EVs that require minimal weights and volumes owing to their simplicity in design and prioritizing high energy density.

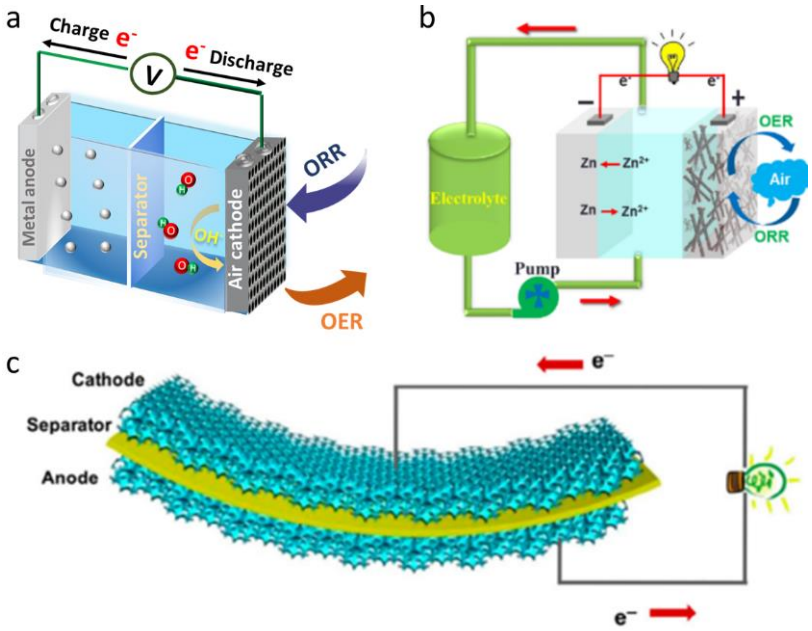

Figure 2.4. Schematic illustration of various types of rechargeable ZABs: (a) conventional aqueous ZABs, (b) a Zn-air flow battery, and (c) a flexible ZAB. Reproduced with permission.[97, 98]

Nowadays, the large-scale rechargeable ZABs for grid-scale energy storage usually use the flow battery configuration, which prioritizes long service lifetimes. The liquid electrolytes between the Zn and air electrodes are needed to be refreshed and pumped from time to time.[97] The circulating electrolyte minimizes the degradation of the Zn electrode and removes insoluble carbonate particles on air electrodes, giving rise to significantly enhanced battery life and stable battery performance.[99, 100]

Therefore, higher cycling lifetimes can be achieved by rechargeable Zn-air flow batteries rather than conventional configurations using static electrolytes. Accordingly, due to the necessity for tubing, pumps, and additional electrolyte volume, the Zn-air flow batteries suffer from higher complexity and worse energy efficiency, leading to lower specific and volumetric energy densities for the overall device. Its bulky nature makes it suitable for large-scale grid storage applications without strict requirements of weight and space. Therefore, the flow battery configuration is currently the most successful type of rechargeable ZABs in practical applications.

With the rapid development of wearable and portable electronics, flexible ZABs have gained great interest and are considered as a hot research direction.[101, 102] To achieve this configuration, each component of the battery such as electrodes and solid-state electrolytes should be mechanically flexible while maintaining a stable electrochemical performance.[98] Alternatively, the components of these flexible batteries can be configured into other forms such as coaxial cables, allowing the assembly of cable-type flexible batteries.[103] The major challenge of current flexible ZABs is to develop a solid-state electrolyte with excellent ionic conductivity while maintaining mechanically durable. At the same time, the electrodes materials also need to undergo large deformation such as bending and twisting.[62, 103-105]

2.3 Chemistry of Zn Electrode

Given that ZABs are supplied with endless sources of oxygen from the air, the Zn electrode is critical in determining the overall capacity of the ZAB. An ideal Zn electrode should possess a high material utilization and be capable of high efficiency, thereby giving rise to outstanding capacity and reversibility. In the following sections, the fundamental insights into understanding these challenges and the strategies that recent studies devoted to overcoming them.

2.3.1 Major Issues of Zn Electrodes

Figure 2.5 shows that the performance of Zn electrodes is primarily restricted by four issues, including i) dendrite formation, ii) shape change, iii) surface passivation, and iv) hydrogen evolution. It is worth

noting that these four factors often interact one another and impact the battery performance over time, eventually resulting in battery failure.[25]

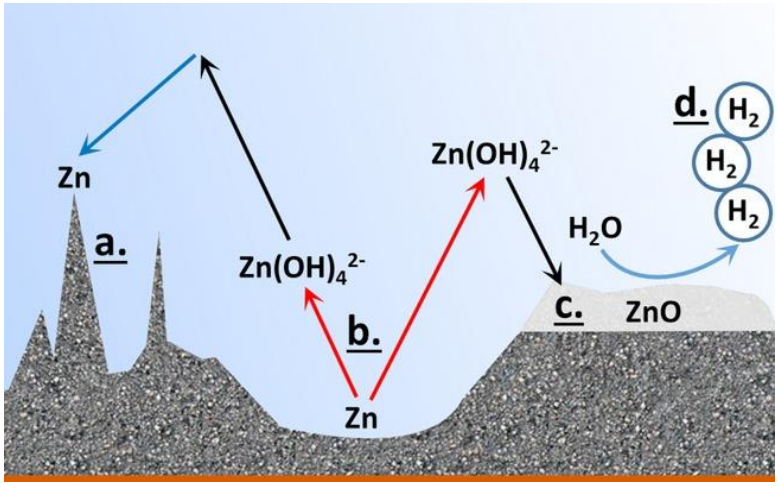

Figure 2.5. Schematic of four major issues occurring at Zn electrode. Reproduced with permission.[25]

i) *Dendrite growth*. Zinc dendrites refer to sharp and needle-like metallic protrusions that formed under certain conditions (e.g., high current density) during electrodeposition.[106-109] Theoretically, the dendritic morphologies result from the inhomogeneous electrodeposition of Zn controlled by the concentration. In a strong alkaline electrolyte, the metal Zn will dissolve and generates a solution saturated or supersaturated with $Zn(OH)_4^{2-}$ ions in the subsequent cycling process. During charging, the Zn species in the electrolyte are reduced and subsequently redeposited on the surface of Zn electrode, starting from the regions near electrolytes with a higher Zn ion concentration.[109] Ideally, the Zn ion concentration distribution over the whole surface of the zinc metal electrode should be uniform. However, the charge distribution is usually non-uniform on Zn electrodes, resulting in concentration variations in local electrolyte regions near the electrode surface. $Zn(OH)_4^{2-}$ ions are preferentially deposit on elevated surface regions and expand into initial protuberances in this situation. The tips of protuberances have higher potentials and consist of high-density low-coordination steps and links with low activation energy, facilitating rapidly dendrites growth.[110] These needle-like dendrites can fracture and disconnect from the Zn electrodes, thus giving rise to losses in battery capacity. They could even puncture the separators and directly contact the air cathode if grows long enough, causing a short-circuit.

ii) *Shape change*. The shape change is formed due to the uneven zinc deposition at different locations on the zinc electrode upon charging. Along with long-time charging-discharging processes, the phenomena can lead to electrode densification followed by significant capacity loss.[111, 112] Generally, shape change occurs as a consequence of non-uniform current distribution and reaction zones over the zinc electrode, as well as the convection driven by the electro-osmotic forces on the cell.[113-116]

iii) *Surface passivation*. The surface passivation of Zn electrodes is the third issue related to the failure of the Zn electrode. Over repeat charging and discharging cycles, the concentration of $Zn(OH)_4^{2-}$ ions in electrolytes reaches its solubility limit and precipitates insulating ZnO film on electrode surface.[113, 117] The formation of such an insulating layer not only raises the internal resistance of the battery but it also inhibits the discharge product and/or OH^- ions from migrating. As a result, this phenomenon usually results in a voltage loss upon discharging and a rise in voltage during charging, thus decreasing battery efficiency. Zinc utilization is a common indicator for evaluating the performance of zinc electrodes, which is greatly influenced by the complete passivation and subsequent increased internal resistance. However, the zinc utilization for conventional powder-based electrodes is usually less than 60-80%.[118-120] For practical applications, it is urgent to further improve the zinc utilization value to 90% or higher.

iv) *Hydrogen evolution.* The last performance-limiting phenomenon is the hydrogen evolution reaction (HER) that occurs on the Zn electrodes surface. The Zn/ZnO standard redox potential is -1.26 V vs. SHE in an aqueous KOH solution at pH 14, leading to a much higher overpotential than that of the HER (e.g., the redox potential for the HER is -0.83V). As a result, the HER process is thermodynamically favorable, which results in the corrosion of Zn electrode and the self-discharge of the battery. Therefore, the zinc electrode cannot be 100% charged, because the HER will consume electrons supplied to the zinc electrode during charging.

$$H_2O + 2e^- \leftrightarrow 2OH^- + H_2 \tag{2.11}$$

$$Zn + 2H_2O \rightarrow ZnO + H_2 \tag{2.12}$$

Notably, in realistic conditions, the four issues discussed above often take place simultaneously in ZABs and reduce the battery performance progressively. For instance, shape change usually results in the

densification of Zn electrodes and thus increases the overpotential during charging. The higher charging potential promotes the formation of dendrite. At the same time, surface passivation also increases the shape change caused by the deterioration of current distribution.[111-113] Moreover, the convective electrolyte flow stemming from the HER process can accelerate the shape change.[112] Therefore, the improvement of Zn electrodes should be performed in consideration of specific battery designs. In this regard, the most suitable solution can be determined by different characteristics of the zinc electrode such as electrolyte volume, thickness, and porosity.

Table 2.2. Strategies and their effects on the performance-limiting phenomenon of Zn electrodes

Strategies	**The performance-limiting phenomenon on Zn electrodes**			
	Dendrite formation	**Shape change**	**Surface passivation**	**Hydrogen evolution**
Electrode structure design				
i) 3D electrode structure	Suppressed	Suppressed	Suppressed	Promoted
ii) Metal foams as the substrate	Suppressed	Suppressed	Suppressed	Promoted
Electrode composition optimization				
i) Adding heavy metals additives	Suppressed	Suppressed	Suppressed	Suppressed
ii) Adding carbon additives	------	Suppressed	Suppressed	------
iii) Polymer coating	Suppressed	Suppressed	------	------
Electrolyte composition optimization				
i) Inorganic additives	------	Suppressed	------	------
ii) Small molecule organic additives	Suppressed	Suppressed	Promoted	Suppressed

2.3.2 Strategies for Alleviating the Surface Side Reactions

A perfect Zn electrode is capable of a long cycle life, a high specific capacity, and a high Columbic efficiency, in which capacity and Columbic efficiency are determined by the ratio of Zn utilization and

the extent of HER, respectively. In the last few years, numerous approaches have been explored to boost the effectiveness of Zn electrodes, including i) the structure design of Zn electrodes, for example, the introduction of 3D porous structure; ii) electrode composition optimization, such as polymeric binders, electrode additives, and coatings; and iii) electrolyte composition optimization, mainly the electrolyte additives. These strategies and their corresponding effects on the performance-limiting phenomenon are summarized in Table 2.2. Notably, these strategies are mostly centered on the improvement of zinc electrodes with static electrolytes, since the circulating electrolyte of the electrolyte in the Zn-air flow battery can greatly alleviate the problems of the Zn electrode.

2.3.2.1 Designing 3D Electrode Structure

Generally, a typical Zn electrode is made up of Zn foils or Zn powders. The geometry of the zinc electrode is important in affecting the performance of Zn electrodes.[121, 122] An effective approach is to introduce a 3D porous structure, which increases the surface area of Zn electrodes, thereby enhancing the interface contact between electrodes and electrolytes. This method allows for a lower overpotential of Zn-deposition and suppresses the formation of Zn dendrites upon charging due to the increased surface area. Additionally, surface passivation can also be reduced by incorporating a 3D structure into the zinc electrode and/or current collector. For instance, Long et al. designed a 3D sponge-like Zn electrode that includes interconnected Zn domains and integral void space (Figure 2.6a).[121] The 3D porous architecture not only maintains fully metallic and interconnects pathways within the core of the electrode structure, but also amplifies the electrified interface in 3D with uniform current distribution throughout the electrode structure (Figure 2.6b). Owing to these advantaged features, this sponge-like electrode reached a high Zn utilization of up to ~90%. Figure 2.6c compares the difference of a powder-based Zn electrode and a 3D sponge-like Zn electrode.[122] As a result, the capacity of 3D sponge-like cell maintained more than 90% of its initial value during discharging at 10 mA cm^{-2}. During subsequent charging operation, over 95% capacity can be restored with a half-cycle voltage hysteresis of less than 300 mV (Figure 2.6d). Thanks to the rich porous structure, ZnO is uniformly deposited in the void space of the electrode, endowing over 100 cycles operation at a depth of discharge of 40%.

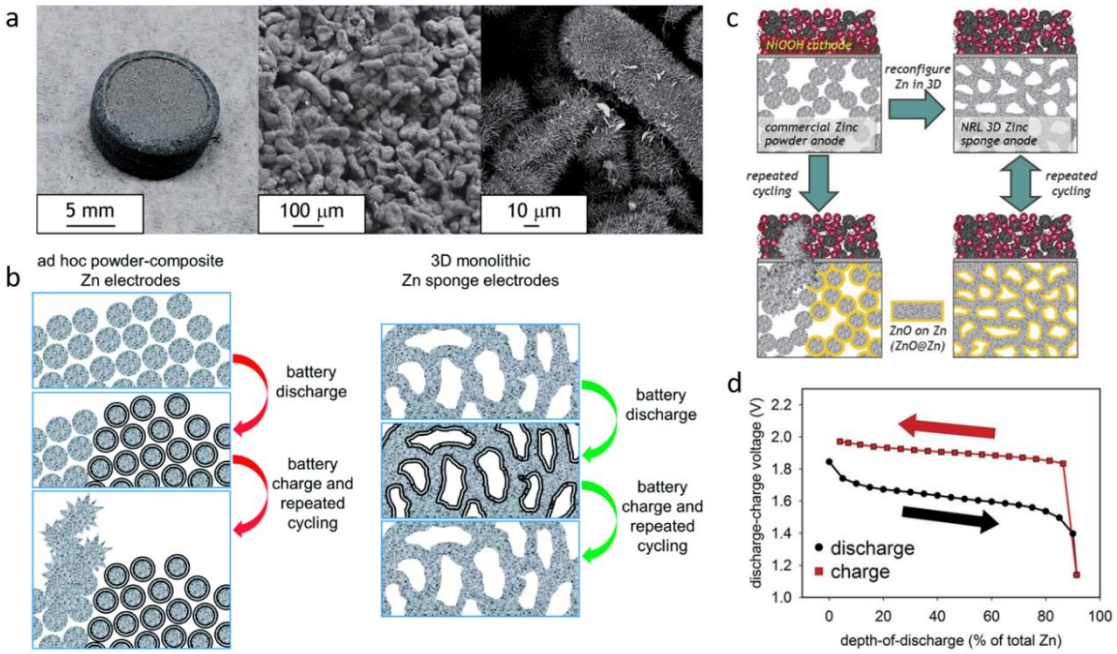

Figure 2.6. (a) SEM images of a 3D sponge-like Zn electrode. (b) Schematic of the discharging and charging processes of 3D sponge-like and traditional Zn powder-based electrodes. Reproduced with permission.[121] (c) Comparison between conventional powder electrodes and the 3D porous electrodes. (d) Discharging and charging profiles of the 3D sponge-like cell. Reproduced with permission.[122]

Alternatively, metal foams with open pores (e.g., copper foam) are widely used as a current collector to construct 3D Zn electrodes as they possess high specific surface area, outstanding mechanical rigidity, and high porosity (ca. more than 95%). In this case, electrodeposition is usually employed to produce Zn coating into the metal foam.[123, 124] For example, a 3D Zn/Cu foam electrodes was developed through the pulse Zn electrodeposition on porous copper foam, in which the interconnected skeleton can offer fast electron transfer and facilitate mass transport.[125] As a result, the Zn utilization of the 3D electrode in primary Zn-O_2 batteries reached about 92%. In a prototype Zn/Ni battery, such an electrode achieved superior cycling and rate performance. However, due to the challenges in achieving thick and uniform metal electrodeposition, the volumetric capacity density is normally far away from the theoretical value for conventional Zn electrodes.

It should be noted that the use of 3D Zn electrodes also has a disadvantage. The high surface area significantly accelerates the Zn corrode and facilitates the HER, which leads to increased self-discharge and worse Coulombic efficiency, as well as reduced battery life (Table 2.2).

2.3.2.2 Optimizing the Composition of Zn Electrodes

In addition to the structure design, optimizing the composition of Zn electrodes can also significantly improve their performance including i) the incorporation of heavy metals or heavy-metal oxides/hydroxides, ii) the addition of carbon additives or polymeric binders, iii) the introduction of polymer coating on the electrode surface. Table 2.2 compares and summarises the benefits and drawbacks of different techniques.

First of all, the incorporation of heavy metals (e.g., Bi, In, Al, Sn, and Pb, etc.)[126-129] or their oxides/hydroxides[130-132] can greatly improve the electrical conductivity of Zn electrodes. For instance, Yang et al. reported a composite Zn electrode by hydrothermally synthesizing Zn-Al layered double oxides and then calcining them.[129] In a Ni-Zn battery, such a Zn-Al composite electrode displayed high reversibility and long-term cycling stability for over 1000 cycles due to the increased electrode conductivity. It is reported that these metallic additives possess a higher overpotential for the HER than that of Zn and ZnO, thus enhancing battery life. Therefore, second metal additives are usually further introduced in the Zn-Al system to enhance the charge distribution in electrodes.[127] As a result, the Zn-Al-In ternary composite electrode exhibits higher HER overpotential and less shape change, giving rise to improved cycling performance.

Secondly, the incorporation of carbon additives or polymeric binders in electrodes can also improve their electrical conductivity or surface area. In this regard, the use of polymer binders such as carboxymethyl cellulose (CMC),[121, 133] polytetrafluoroethylene (PTFE),[111, 121] and poly(vinylidene fluoride) (PVDF), [25, 134] can not only improve the surface area, but also increase the mechanical strength of Zn electrode, which is beneficial for reducing dendrite growth and avoiding shape change. It should be noted that due to their non-conductive nature, the use of polymeric binders increases internal

resistance and results in low zinc utilization. To address this issue, carbon-based additives have been explored because of their high conductivity and excellent chemical stability to the alkaline electrolytes.[134-136] As expected, the use of carbon additives can significantly avoid surface passivation and improve zinc utilization. The zinc utilization significantly increased from 68% to 95% after adding 2 wt.% Super P carbon black.[137]

Alternatively, coating polymer layer on Zn electrodes is another attractive strategy to improve the performance of Zn electrodes, which enables effective migration of OH^- ions but blocks or reduces the $Zn(OH)_4^{2-}$ migration during charging and discharging processes. The decreased rate of $Zn(OH)_4^{2-}$ ions migration not only avoids shape change, but also suppresses dendritic growth by reducing concentration gradients during charging. For instance, Zhou et al. fabricated a polyvinyl alcohol (PVA)/poly(diallyldimethylammonium chloride) (PDDA) composite coating on the Zn electrode surface.[138] As expected, the obtained electrode exhibited enhanced discharge capacity and reduced dendrite growth after 60 cycles as compared to a bare Zn electrode. Unfortunately, coating materials increase the bulk of Zn electrodes, resulting in decreased specific mass capacity. As a result, novel coating materials that may inhibit Zn dendrite formation while also increasing capacity are very sought.

2.3.2.3 Electrolyte Composition Optimization

Besides electrode additives, the utilization of electrolyte additives has also been intensively explored to overcome the challenges that occurred on Zn electrodes. As reported, the performance of Zn electrodes is greatly affected by the concentration of KOH.[25] Typically, the optimal electrolyte for a ZAB is an aqueous KOH solution with a high concentration of roughly 6-7 M (or 25-30 wt.%), since it achieves the maximum electrolyte conductivity and the Zn/Zn^{2+} redox kinetics (Figure 2.7).[139] However, along with the increase in concentration, the solubility of the ZnO discharge product rises, and so does the corrosion of Zn electrodes. To address this issue, a widely used and effective strategy is to pre-saturated KOH solutions with $Zn(OH)_4^{2-}$ ions by dissolving ZnO powder. However, the precipitation of ZnO occurs slowly even in supersaturated $Zn(OH)_4^{2-}$ solutions.

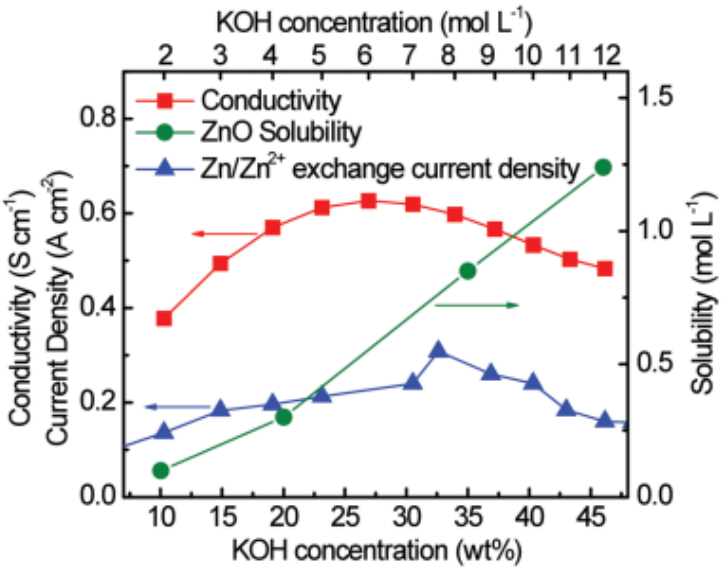

Figure 2.7. Summary of electrolyte conductivity, Zn/Zn^{2+} exchange current density, and ZnO solubility as a function of the KOH concentration. Reproduced with permission.[25]

Therefore, various inorganic additives including KF, As_3O_4, K_2HBO_3, K_3BO_3, K_2CO_3, and K_2CrO_4 have been used in electrolytes to create low Zn solubility.[111, 140] by adding these inorganic additives, the rate of shape change occurring on Zn electrode can be significantly reduced. Alternatively, small molecular organic additives including ionically Zn complexes, citric acid, sorbitol, and tetra-alkyl ammonium hydroxides,[141-143] have also been explored in electrolytes to suppress dendrite growth and HER issues. During charging, these additives tend to be deposited into the Zn electrode's most electrochemically active regions during charging, decreasing these two occurrences. Unfortunately, decreasing the solubility of Zn species or increasing their supersaturation in electrolytes may enhance surface passivation of Zn electrodes. In other words, these methods can only be effective within specified parameters.

2.4 Separators

In batteries, a separator normally acts as a physical barrier that separates the Zn electrode and air electrode, allows for ionic flow, and prevents physical contact of electrodes. The main role of the separator is to avoid short circuits caused by zinc dendrite formation during cycling. Generally, an ideal separator should possess the following features including i) being electrochemically stable and inactive in a strongly alkaline environment, 2) having a broad electrochemical stability window (ca., ≥2.5 V), and has low resistance and a high ionic conductivity.[144, 145] However, up to now, the separators in ZABs have not received its deserved attention since most of them are usually taken from lithium-based batteries, but not designed specifically.

For the specifical separator used in ZABs, a fine porous structure is crucial for allowing the migration of OH^- ions yet preventing the transportation of $Zn(OH)_4^{2-}$ ions.[146, 147] But the transfer of $Zn(OH)_4^{2-}$ ions through the separator may result in the formation of ZnO precipitates on the air cathode, thereby increasing the polarization of air electrodes. The commonly used separators in most studies of ZABs are polypropylene based porous membranes such as Celgard 5550 and Celgard 4560. These separators possess excellent mechanical strength to undergo dendritic penetration and have a wide working potential window.[144, 145] Their shortcoming is the relatively large pore size, which is insufficient for preventing $Zn(OH)_4^{2-}$ ions migration and thus leads to poor long-term durability. Therefore, developing the separators with high ionic selectivity is crucial, for example, the alkaline anion-exchange membranes. In this regard, a cationic polysulfonium membrane was designed to prevent $Zn(OH)_4^{2-}$ ions from migrating to the air electrode.[148] The obtained membrane showed a high ionic selectivity of OH^- ions and was sufficient in preventing the crossover of zincate cations, enabling an increased discharge capacity as compared to a commercial Celgard separator. Unfortunately, the anion-exchange membranes have the problems of poor chemical reliability and high manufacturing costs, which hampers their practical applications. To this end, covering commercial separators with an inorganic barrier layer on has been proposed as an efficient strategy. Various inorganic compounds, such as CaF_2, $Al(OH)_3$, $Mg(OH)_2$, and $Mn(OH)_2$ have been investigated for improving the permeability of $Zn(OH)_4^{2-}$ ions.[149, 150]

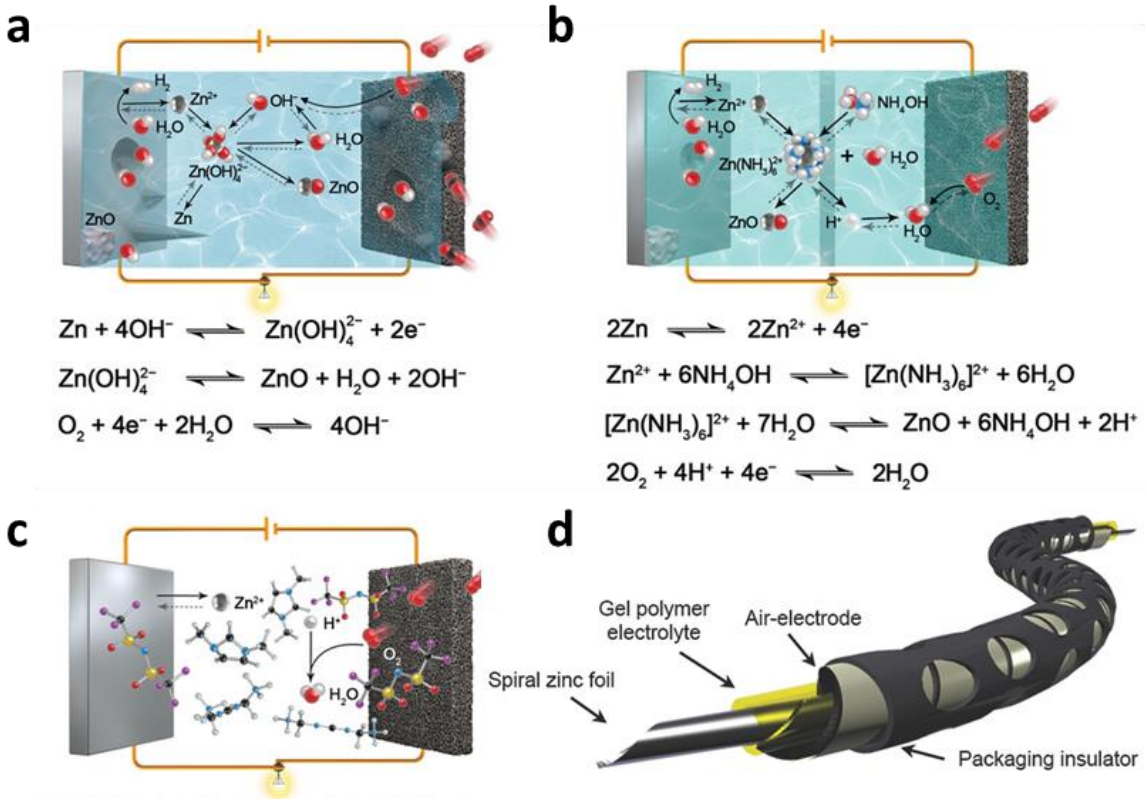

Figure 2.8. Schematic illustration of rechargeable ZABs with (a) alkaline aqueous electrolytes, (b) near-neutral electrolytes, and (c) ILs. Reproduced with permission.[151] (d) Schematic of a cable-type flexible ZAB assembled with gel polymer electrolyte. Reproduced with permission.[103]

2.5 Electrolytes

As compared to electrode materials, the role of electrolytes in ZABs is also significantly underestimated. Electrolytes are considered as the "blood" of batteries and have a profound impact on battery performance. An ideal electrolyte for rechargeable ZABs should possess the following features including i) high ionic conductivity and low electronic conductivity, ii) low electrode corrosion and good ion accessibility at the three-phase zone, iii) good electrochemical stabilities, and iv) low cost and safety. In ZABs, aqueous, ionic liquids, and semisolid-state electrolytes are the main three types of electrolytes (Figure 2.8). To date, ZABs mainly operate in aqueous alkaline electrolytes due to their strong ionic conductivity, high gas diffusion coefficients, and high solubilities of carbonates (K_2CO_3 or $KHCO_3$) that are produced by the electrolyte reacting with CO_2 from the air. As discussed above,

alkaline electrolytes lead to serious Zn corrosion and suffer from the negative effects of carbon dioxide (CO_2). Non-alkaline electrolytes, such as near-neutral electrolytes, acidic electrolytes, and ionic liquids (ILs), have been developed to address these concerns.[151] Furthermore, semisolid-state electrolytes have been extensively researched to realize flexibility and minimize battery leakage concerns, extending the possibilities of rechargeable ZABs for powering flexible and portable devices.[103]

2.5.1 Aqueous Electrolyte

Alkaline, acid, and near-neutral electrolytes are the three types of aqueous electrolytes found in ZABs. Among them, alkaline electrolytes are the most popular ones due to their better Zn-corrosion resistance, better electrochemical kinetics, higher ionic conductivity, and the wider availability of electrocatalysts.[152] Typically, a 25-30 wt.% corresponding to 6-7 M KOH aqueous electrolyte is applied in ZABs to achieve desirable ionic conductivity and reaction kinetics for both the ORR and OER. Nevertheless, the phenomena of nonuniform dissolution and inhomogeneous redeposition of zinc occur upon cycling, which promotes dendrite growth and degrades the cycle life. In addition, due to the sensitivity to CO_2 in the air, alkaline electrolytes suffer from the degradation issue that affects battery performance.[153] Therefore, increasing attention has also been focused on developing non-alkaline electrolytes such as acidic and near-neutral electrolytes.

Electrolytes with pH levels close to neutral should prevent the formation of zinc dendrite and avoid electrolyte carbonation.[154, 155] The commonly used near-neutral electrolytes in ZABs applications are aqueous inorganic salts (e.g., $ZnCl_2$ and NH_4Cl) solutions. The first rechargeable ZABs using a near-neutral electrolyte were reported by Thomas Goh et al. in 2014.[155] The electrolyte with a pH of 6 consisted of 2.34 M NH_4Cl, 0.51 M $ZnCl_2$, and a small amount of PEG and thiourea. As a result, no carbonate formation was observed after 120 cycles corresponding to 1440 h operation. Although Cl-based neutral electrolytes have been proven for rechargeable ZABs, there are still several challenges. First, during battery charging, an inevitable chlorine evolution reaction occurs and competes with the OER due to the similar overpotential, resulting in a decreasing Columbic efficiency. Second, in near-

neutral electrolytes, the ORR and OER reaction kinetics are substantially slower than that in alkaline electrolytes. Consequently, the ORR and OER polarization becomes larger, thereby decreasing the discharge voltage and increasing the charge voltage during cycling. As a result, optimizing catalytic processes in near-neutral electrolytes is extremely desirable for practical applications in ZABs.

Very recently, Wang et al. proposed a rechargeable ZAB with a novel $2e^-$ ORR process based on a non-alkaline aqueous $Zn(OTf)_2$ electrolyte.[156] Owing to the establishment of Zn^{2+}-rich and H_2O-poor inner Helmholtz layer, the Zn utilization ratio (ZUR) in the adopted OTf^- anions-based electrolyte achieved an impressive value of 83.1%, ten times higher than that in the common used KOH electrolyte (8.1%) (Figure 2.9a). Furthermore, the ZABs with OTf^- anions-based electrolyte exhibited excellent cycling stability in the ambient atmosphere and essentially no visible pH change during charging and discharging processes (Figure 2.9b-c). The Zn^{2+}-rich and H_2O-poor structure, as well as the weak interaction between Zn^{2+} cations and OTf^- anions, support a novel $2e^-/O_2$ chemistry (Figure 2.9d).

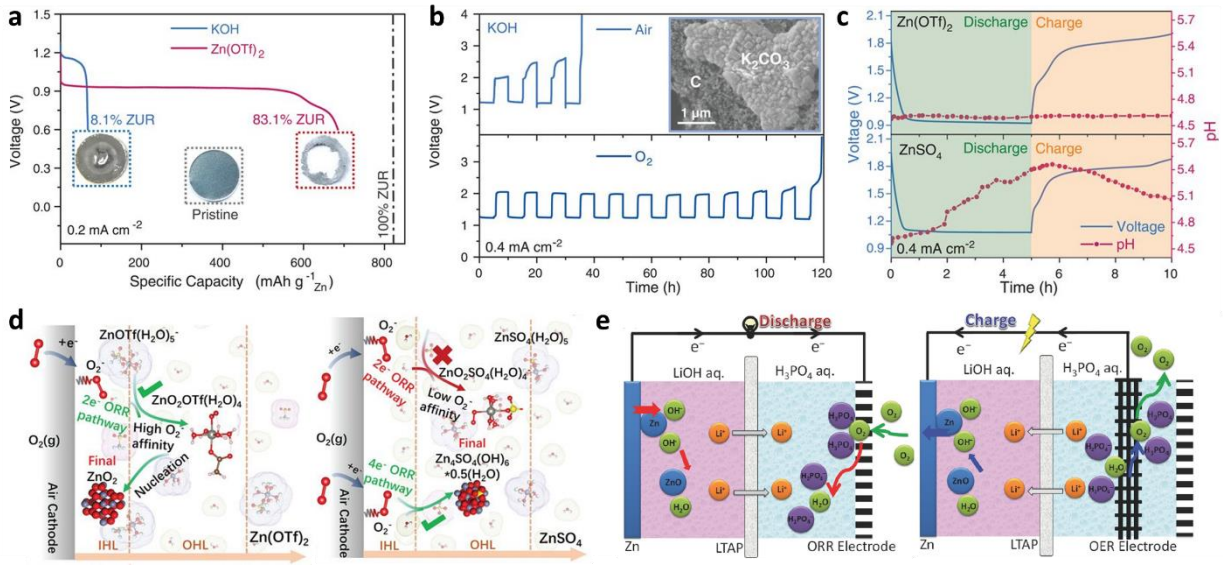

Figure 2.9. (a–b) Electrochemical performance of ZABs with $Zn(OTf)_2$ and KOH electrolytes. (c) Discharge and charge curves of $Zn(OTf)_2$ and $ZnSO_4$ electrolytes based batteries, and their associated pH values during cycling. (d) Schematic of the mechanism of the inner and outer Helmholtz layer in various electrolytes, respectively. Reproduced with permission.[156] (e) Working mechanism of an asymmetric-electrolyte Zn-air battery. Reproduced with permission.[157]

Similarly, acidic electrolytes also show promising potential in preventing electrolyte carbonation and short circuits produced by dendrite growth. By offering a greater ORR redox potential (1.23 vs SHE) than near-neutral electrolytes, the use of acidic electrolytes can avoid the catalytic limiting problem, increasing the output voltage and energy density of practical devices. However, metallic Zn undergoes serious dissolution accompanied by hydrogen evolution in an acidic media. In this regard, the design of alternative cell configurations can be considered as an interesting strategy. In 2016, Li and Manthiram first proposed an attractive concept of asymmetric-electrolyte ZABs by using decoupled electrolytes and a decoupled air electrode (Figure 2.9e).[157] The use of acidic catholyte can effectively alleviate the common problems in alkaline electrolytes, such as carbonation and low cell voltage. Consequently, the asymmetric ZAB delivered a high working voltage of ~1.92 V and stably operated for more than 200 h. The concept of asymmetric ZABs inspires a new route to achieve high-energy-density ZABs for future practical applications.

2.5.2 Ionic Liquids

In addition, ionic liquids (ILs) consisting of large organic cations and organic/inorganic anions, have also attracted special attention as effective electrolytes for rechargeable ZABs.[158] Compared with aqueous electrolytes, ILs possess the advanced properties of superior thermal stability, wide electrochemical windows, and low vapor pressure owing to their intrinsically high concentrations. These superior properties can potentially address the issues of zinc corrosion, water loss, and CO_2 poisoning caused by aqueous electrolytes.[158-161] However, the application of ILs-based electrolytes in rechargeable ZABs is still in its early stage with only a few systematic studies being conducted.

ILs can be classified as either protic ILs or aprotic ILs depending on the ability to form a hydrogen bond network in the solvent. The aprotic ILs rely on the presence of hydroxide ions or protons, which are incompatible with the current O_2 electrochemistry. By contrast, protic ILs that can dissociate protons are more favorable to support O_2 electrochemistry through a $2e^-$ process, generating hydrogen peroxide.[162] Unfortunately, ILs also suffer from a low conductivity ranging from 0.1-40 mS cm^{-1} due to their low ionic mobility caused by high viscosity.[162] Consequently, both the Zn/Zn^{2+} and O_2/O_2^- chemistry are kinetically sluggish. Therefore, to address these issues, the optimization of IL

composition by adding additives such as water and ethylene glycol is of great importance, which can decrease the viscosity and facilitate ion mobility. In addition, ILs also suffer from high costs, which greatly limits their practical application in cost-competitive ZABs.

2.5.3 Semisolid-State Electrolyte

Portable and wearable energy devices that require flexible power sources have recently attracted considerable attention. As a key component for flexible batteries, semisolid-state electrolytes that having good shape consistency are highly desirable to serve as both ion conductors and separators for achieving ion transport and flexibility. Currently, gel polymer electrolytes (GPEs) consisting of polymer matrix and electrolyte solutions, are the most extensively studied electrolyte.[163-165] Because GPEs can combine the advantages of good mechanical properties from polymeric solids and high ion conductivity from liquids. Due to the randomly distribution of conductive ions within the electrolyte polymer matrix, the ionic conductivity of OH^- in semisolid-state electrolytes is about 10^{-4}-10^{-1} S cm^{-1}, much lower than aqueous electrolytes. Conversely, semisolid-state electrolytes possess good mechanical flexibility and serve as a separator to prevent internal short circuits and suppress dendrite formation in the battery. Therefore, a trade-off between mechanical strength and ionic conductivity should be considered according to the special requirements.

It should be noted that the electrolyte/electrode interfacial properties are crucial in determining the battery performance, but its improvement remains challenging in the solid configuration.[166] For example, bifunctional catalysts with high surface area have complete access to the electrolyte in aqueous systems, allowing for an effective reaction zone for oxygen electrochemistry.[167, 168] By contrast, the oxygen redox reactions in the solid systems are greatly limited owing to low wettability of the "immobilized" electrolyte. Therefore, the interfacial resistance for hydroxide ion transport is substantially higher, resulting in undesirable low current rates and high overpotentials.[105, 166, 169, 170]

Overall, the electrolyte governs the electrochemistry of ZABs and largely determine their lifespan, rechargeability and operating voltage. However, as previously said, each type of electrolyte has its own

set of benefits and drawbacks. An perfect electrolyte with desired qualities of extended lifetime, high operating voltage, and high energy output has yet to be produced due to trade-offs between different performance criteria.

2.6 Bifunctional Air Electrodes

The performance and energy efficiency of ZABs are also influenced by the air electrodes. This stems from the fact that both the OER during charging and ORR during discharging have a larger energy barrier that needs to be overcome as compared to the Zn electrode reactions.

A typical air electrode serves a variety of purposes including supplying O_2 diffusion channels, promoting ion transport and electron transfer, assuring oxygen electrochemical catalytic activity, etc. To achieve these functions, four key parameters concerning the surface/interface properties of the air electrode are of great importance.[171] Firstly, sufficient reaction areas are crucial for both electrocatalysts and air electrodes. Electrocatalysts with a large specific surface area can offer enough active sites for catalyzing oxygen redox reactions, while an air electrode with sufficient reaction area can support enough electrocatalyst and provide pore channels for efficient mass transfer and oxygen diffusion at the three-phase zone. Secondly, the electrical conductivity of the electrocatalyst and air electrode cannot be ignored. Electrons can quickly access active centers due to the high electrical conductivity, facilitating the charge transfer process and reducing electrochemical polarization. Third, electrocatalysts with rationally designed atomic and electronic surfaces can significantly reduce the reaction energy barriers for ORR and OER, thereby enhancing catalytic activity. Finally, the fast mass transfer capability of the air electrode can provide sufficient oxygen and ions for oxygen electrochemistry to reduce the concentration polarization during the reaction.

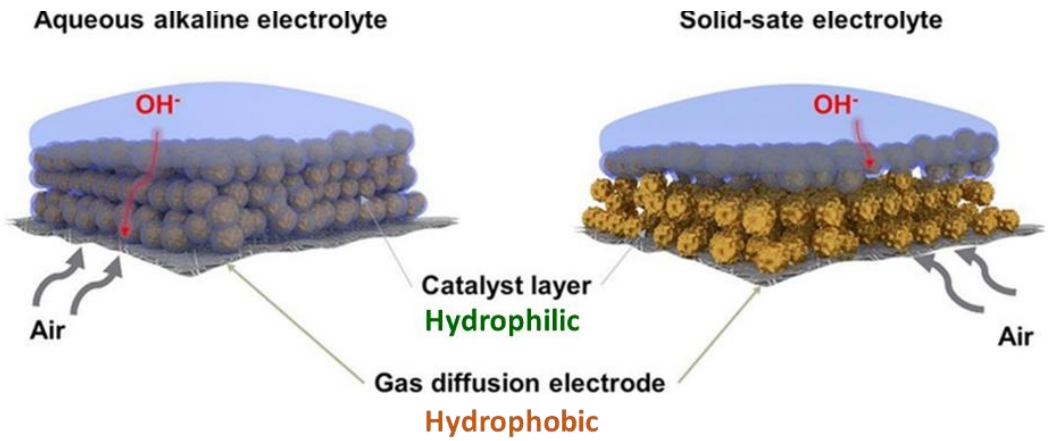

Figure 2.10. Schematic illustration of the air cathode architecture with different electrolytes. Reproduced with permission. Reproduced with permission.[25]

Generally, the architecture of an air electrode is mainly made up of a hydrophobic gas diffusion layer (GDL) and a hydrophilic catalyst layer (Figure 2.10).[25] The GDL with porous structure provides physical support for the catalysts and offer gas channels accessible for oxygen to active centers. The catalyst layer containing electrocatalysts faces with the electrolyte to construct a so-called three-phase interfaces for oxygen redox reactions. Due to the limitation of oxygen solubility in liquids, air electrodes not only require high specific surface area to provide enough reaction space for oxygen reactions, but also possess favorable hydrophobicity to facilitate the rapid mass transfer and oxygen diffusion. Therefore, rational air electrode design with appropriate interfacial structure and hydrophilicity, as well as strong electrical conductivity for rapid electron transit, is critical. In addition, the development of high-performance bifunctional air electrodes is also extremely challenging. Both the ORR and the OER should overcome significant overpotentials, necessitating the use of a bifunctional electrocatalyst to promote oxygen processes.

2.6.1 Gas-diffusion Layer Design

Typically, The GDL of ZABs should have the following characteristics, including i) providing physically support for the catalyst, ii) allowing the rapid diffusion of oxygen into the catalyst, iii) preventing electrolyte leakage, and iv) providing a conductive channel for electrons. the GDL should

be very porous and hydrophobic to promote air transport in ZABs. The degree of hydrophobicity impacts the polarization behavior of the cell in terms of conductivity (Ohmic resistance) and gas permeability (mass transfer), which can be obtained by utilizing hydrophobic binders such as PTFE,[172, 173] PVDF,[174] and fluorinated ethylene propylene (FEP)[175, 176]. For improved performance, it should be able to prevent electrolyte evaporation and resist electrolyte flooding in harsh situations.[177] Furthermore, an ideal GDL should have efficient gas diffusion, high electrolyte repellency, high mechanical integrity, excellent electrical conductivity, and consistent electrochemical and chemical stability in strong alkaline environments.

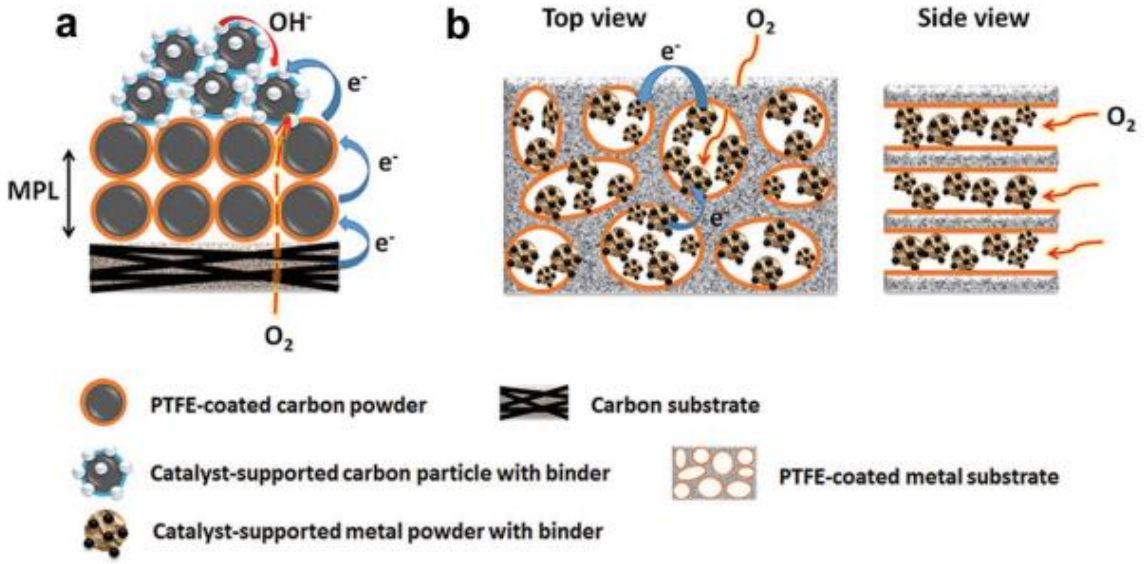

Figure 2.11. Schematic of the architecture of (a) carbon-based and (b) metal based GDLs. Reproduced with permission. Reproduced with permission.[25]

As shown in Figure 2.11a, these carbon-based GDLs generally have a bilayer architecture consisting of a macroporous gas diffusion substrate and a thin microporous layer (MPL). The substrate is a porous and hydrophobic carbon cloth or carbon paper that can provide sufficient gas diffusion channels, while MPL is a thin and relatively hydrophilic porous activated carbon layer that can support the catalytically active material and minimize interface contact resistance between these two layers.[178] The most widely used GDL is carbon cloth, as it has excellent mechanical flexibility and then serves as a robust catalyst

layer support for flexible ZAB applications. However, there are still significant issues with the stability of these improved carbon-based GDLs during oxygen evolution (charging) and exposure to strong alkaline electrolytes. Because carbon materials are prone to corrosion in this case, resulting in the loss of the active surface area of oxygen electrochemistry, uneven current distribution on the electrode surface, and serious electrolyte leakage.[140, 168] Meanwhile, dissolved carbonate species stemmed from carbon corrosion of GDLs have an adverse effect on the ionic conductivity and pH of the electrolyte. Therefore, for sufficient operation, the use of highly corrosion-resistant graphitized carbon materials or metal-based materials are required to prevent corrosion of the GDL. Metal substrates comprised of stainless-steel mesh and nickel/copper foam are now popular, and their performance is comparable to that of carbon-based GDLs in ZAB. Metal-based GDLs are typically made by pouring and pressing a catalyst, metal powder, and PTFE binder into a porous metal foam (Figure 2.11b). Over a wider potential range, such GDLs can provide higher electrical conductivity and better electrochemical oxidation stability.

2.6.2 Bifunctional Oxygen Electrocatalysts

2.6.2.1 Oxygen Electrochemistry

ORR. Essentially, ORR is a multi-electron transfer process that includes two different reaction pathways according to the electrolyte: an indirect two-electron ($2e^-$) process to form H_2O_2 and a direct four-electron ($4e^-$) process to generate H_2O or OH^-.[179] As shown in Figure 2.12, in acidic electrolyte, O_2 can be directly converted to H_2O through a $4e^-$ process or partially reduced to H_2O_2 via a $2e^-$ process, and subsequently converted to H_2O. In an alkaline electrolyte, O_2 can be reduced by either a direct $4e^-$ process to yield OH^- or a two-step $2e^-$ process to produce HO_2^- and then OH^-. The related reactions can be described as follows:

Acidic media

$$O_2 + 4H^+ + 4e^- \rightarrow 2H_2O \quad (2.13)$$

$$O_2 + 2H^+ + 2e^- \rightarrow H_2O_2 \quad (2.14)$$

$$H_2O_2 + 2H^+ + 2e^- \rightarrow 2H_2O \quad (2.15)$$

Alkaline media

$$O_2 + 2H_2O + 4e^- \rightarrow 4OH^- \quad (2.16)$$

$$O_2 + H_2O + 2e^- \rightarrow OOH^- + OH^- \quad (2.17)$$

$$OOH^- + OH^- + 2e^- \rightarrow 3OH^- \quad (2.18)$$

The ORR pathway is surface sensitive and extremely complex, involving the adsorption and dissociation of various intermediates generated on the catalyst surface during the reaction.[180] These intermediates include oxidative (O*), hydroxyl (OH*), and superhydroxyl (OOH*) species, where * represents a catalytically active site on the catalyst surface. Thermodynamically, the selectivity of the $4e^-$ or $2e^-$ route is mainly determined by the reactant and intermediate adsorption energies, as well as their dissociation reaction barriers on the active surface.[181] The direct $4e^-$ process for the ORR is more efficient and preferable in practical applications than the $2e^-$ process,

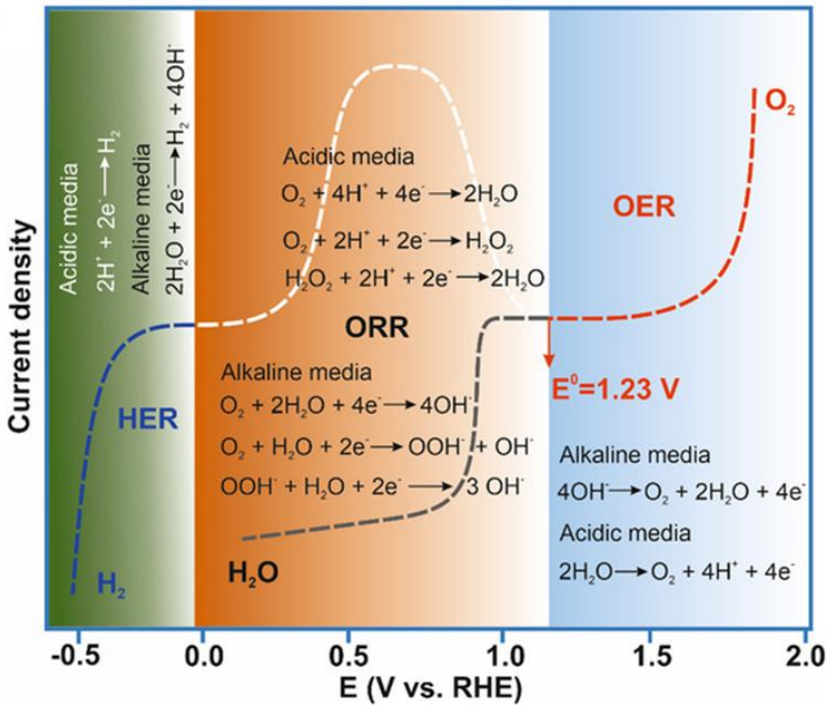

Figure 2.12. Polarization curves and related mechanism of the typical oxygen redox reactions in both alkaline and acid electrolytes.

Two possible mechanisms for the 4e- process in alkaline media (similar in acid media, not depicted here) have been proposed: a dissociative mechanism and an associative mechanism.[181] The dissociation mechanism can be described as the following process: First, O_2 is adsorbed to the catalyst surface, followed by breaking the O-O bond and forming two adsorbed atomic O* species. The resulting O* species then react with hydrogen to create OH* and eventually OH^-.[182] The ORR procedure can alternatively be carried out through the following associative mechanism: The oxygen adsorption in the active center produces O_2*, which first combines with hydrogen to make OOH*, and then the O-O bond is broken to produce O* and OH*. Finally, the products O* and OH* combine with hydrogen to generate the final product OH^-. Therefore, whether the reaction proceeds in a dissociative or associative way is determined by the reaction energy barrier for O-O bond breakage and first O_2 dissociation. According to the reaction mechanism described above, an ideal ORR electrocatalyst should have a porous structure with a large specific surface area, great electrical conductivity, and a low reaction energy barrier, allowing rapid reaction kinetics to catalyze the ORR.

OER. The OER process is essentially the converse of the ORR. During ORR, O_2 is reduced to form H_2O or OH^-, whereas H_2O is oxidized to produce O_2 during OER.[183]

Alkaline media:

$$4OH^- \rightarrow O_2 + 2H_2O + 4e^- \quad (2.19)$$

Acidic media:

$$2H_2O \rightarrow O_2 + 4H^+ + 4e^- \quad (2.20)$$

During charging OER occurs as an anodic reaction of rechargeable ZABs. Unlike ORR, OER needs not only several electron transfers processes, but also the crossing of substantial reaction energy barriers, resulting in extremely sluggish kinetics. Four O-H bonds are broken, and four O-O bonds are formed in the corresponding chemical process. The majority of the published OER reaction mechanisms mostly contain the two probable pathways: 1) direct binding of two O* to produce O_2; or 2) production of

OOH*, which is then transformed to O_2.[184, 185] RuO_2 and IrO_2 are now cutting-edge electrocatalysts for OER in alkaline and acidic environments. Unfortunately, they suffer from a lack of resources, a high cost, and low durability, all of which limit their practical implementation. Therefore, innovative OER electrocatalysts with cheap cost, high activity, and outstanding durability are critical for effective water splitting.[186]

2.6.2.2 Oxygen Electrocatalysts

The energy efficiency of rechargeable ZABs significantly relies on the ORR and OER activities. However, it is still challenging for efficient electrocatalysts that are capable of catalyzing two reactions. Current commercial electrocatalysts cannot meet the market requirements for rechargeable ZABs. For instance, the noble metal Pt is a cutting-edge electrocatalyst for ORR in both alkaline and acid conditions, yet the deposition of oxide layers on Pt results in low OER activity. Noble-metal oxides, such as RuO_2 and IrO_2, dominate the OER environment but are inactive for ORR.[32, 33] Besides, the high price, scarcity, limited selectivity, and poor long-term durability of noble-based catalysts limit their practical utilization. As a result, creating cost-effective and efficient electrocatalysts from earth-abundant elements to replace noble-metal-based catalysts is highly desirable.[30, 187-189]

In some cases, decoupled air cathodes are introduced separately by loading different electrocatalysts toward the ORR and OER processes, but the use of decoupled electrodes usually complicates the battery configuration. Thus, the design and development of highly effective bifunctional electrocatalysts is crucial for the practical applications of ZABs. In recent years, numerous electrocatalysts that effectively accelerate the ORR and OER process have been demonstrated for ZAB air electrodes. In the following section, recent widely used bifunctional electrocatalysts that are explored in rechargeable ZABs are discussed, involving i) heteroatom-doped carbon materials, ii) transition metal-nitrogen-carbon materials (M-N-C, M= Fe, Co, Ni, etc.), iii) transition metal oxides, iv) perovskites, and v) COF-based materials.

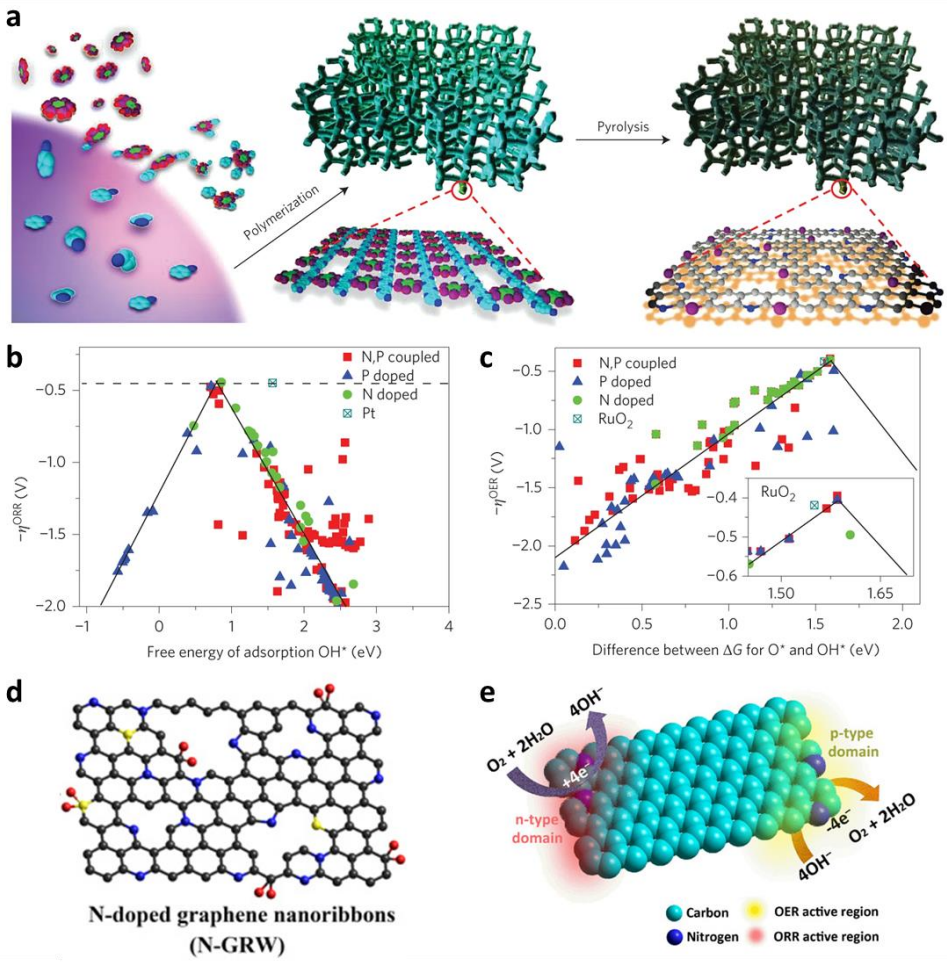

Figure 2.13. (a) Preparation of the 3D mesoporous carbon foams. Volcano plots of (b) ORR overpotential versus the adsorption energy of OH* and (c) Volcano plot of OER overpotential versus the adsorption energy of O* and OH*. Reproduced with permission.[191] (d) Schematic illustration of the N-GRW. (e) Schematic of ORR and OER processes occurring at n- and p-type domains on the N-GRW. Reproduced with permission.[192]

Heteroatom-Doped Carbon Materials. Traditional carbon nanomaterials (e.g., graphene, CNTs, porous nanocarbons, etc.) have been extensively studied as effective electrocatalysts because they possess high surface area, excellent electrical conductivity, and low cost. However, the properties of pure carbon materials are still unsatisfactory. Doping heteroatoms (e.g., N, P, S, F, and B) has considered as a viable technique for improving the electrochemical activity of these carbon compounds.[190] The incorporation of heteroatoms into the carbon matrix not only tunes the charge distribution and electronic properties,

but also induces defects, thereby enhancing the OER and ORR catalytic activities of the material. Zhang and his coworkers provided the first example of N- and P-doped carbon materials being used as bifunctional electrocatalysts for ZABs.[191] Pyrolysis of a PANI aerogel with phytic acid yielded 3D mesoporous carbon foams co-doped with N and P (NPMCs) with high bifunctional activities (Figure 2.13a). Density functional theory (DFT) calculates the lowest overpotentials of N, P co-doped graphene for ORR and OER to be 0.44 and 0.39 V, respectively (Figures 2.13b and 2.13c), substantially lower than those of noble metals.

Yang et al. experimentally identified the truly catalytic sites for ORR and OER in N-doped graphene in another key paper.[192] The first N-doped 3D graphene nanoribbon (N-GRW) networks were created by pyrolyzing carbon nitrides produced by polymerizing melamine with L-cysteine (Figure 2.13d). The N-electron-withdrawing GRW's pyridinic N moieties served as active sites for OER, while the electron-donating quaternary N sites were responsible of ORR. The separated active sites at the n- and p-type domains, as shown in Figure 2.13e, contribute to avoid ORR and OER cross-deactivation.

Metal-Nitrogen-Carbon Materials. M-N-C materials have attracted a lot of interest owing to their high catalytic activities for oxygen redox processes.[193] Unfortunately, the active catalytic sites of M-N-C materials are still unclear. There are three major explanations proposed and widely recognized as the true active sites, such as metal-N moieties embedded in carbon matrix (MN_xC_y), metal species encapsulated in N-doped carbon ($M@N_xC_y$), and N-doped carbon moieties (N_xC_y). For instance, the MN_4C_4 species were proposed as the active centers in a sample of N-doped graphene embedded with Fe, Co, and Ni (Figure 2.14a). Depending on the number of *d* electrons of the metal, the OER process occurs on Fe or Co single -atom active sites, and simultaneously on both Ni and C sites.[194]

Generally, the use of M-N-C materials as efficient bifunctional electrocatalysts focuses on the following two strategies. The first strategy is to expose more active sites by increasing mass loading or altering the shape and size of the catalyst to increase the active sites amount. For example, Meng et al. fabricated a chemically crosslinked hydrogel with atomically dispersed Fe ions through a rapid implosion (Figure 2.14b).[195] After pyrolysis, highly effective catalysts with evenly Fe-N-C active centers were obtained. Compared with Pt/C, the obtained catalyst demonstrated superior catalytic activity and excellent

durability for both ORR and OER, rendering it a high-performance cheap bifunctional electrocatalyst. Another option is to tune the catalyst's composition to increase its inherent catalytic activity. In another work, a FeCo-N-C bimetallic composite was fabricated by incorporating bimetallic FeCo nanoparticles in N-doped CNTs, which served as a bifunctional catalyst (Figure 2.14c).[196] The ORR and OER catalytic activity may be rationally adjusted using the ideal catalyst by carefully altering the Co and Fe concentrations. The overall performance outperforms noble metal benchmarks (e.g., Pt/C for ORR and IrO_2 for OER), displaying lower overpotential, higher current density, and more favorable thermal properties.

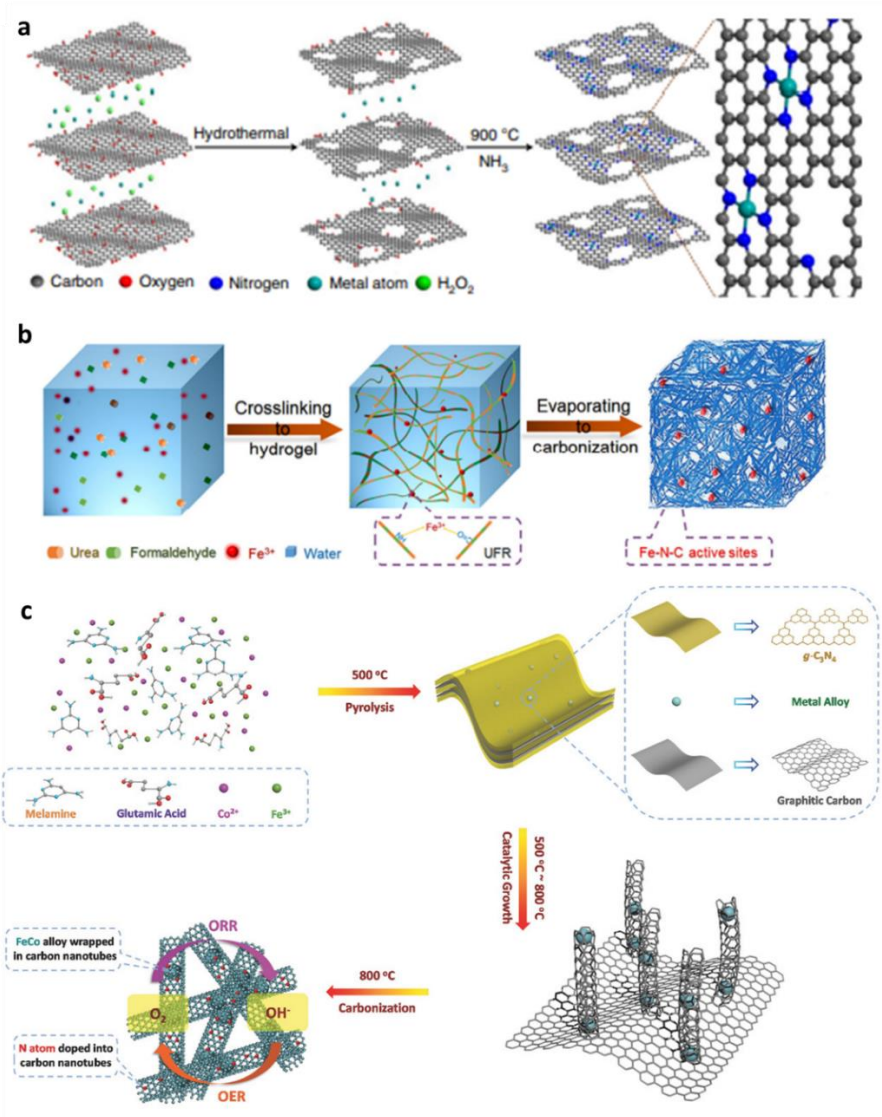

Figure 2.14. (a) Schematic illustration of the fabrication of FeCo-N-C bimetallic composite. Reproduced with permission.[194] (b) Schematic illustration of the preparation of the Fe-N-C catalyst

derived from a crosslinked hydrogel. Reproduced with permission.[195] (c) Schematic illustration for the fabrication of FeCo-N-C composite catalysts. Reproduced with permission.[196]

Transition Metal Oxides. In addition to M-N-C materials, transition metal oxides[197, 198] have also considered as promising candidate owing to their superior properties, including i) low-cost and composed of earth-abundant elements; ii) easy to hybrid with other transition metal oxides to create hybrid electrocatalysts with enhanced catalytic activity; iii) possess multiple oxidation states, enabling the toleration of constant oxidation and reduction conditions during operation; and iv) have diverse crystalline and amorphous structures, allowing for structural pre-engineering and tailoring to enhance electrocatalytic activities. However, the bifunctional activity of oxide catalysts is significantly limited by their inherent low conductivity and the aggregation of metal oxide nanoparticles. Several strategies have been proposed to improve the performance of transition metal oxide-based electrocatalysts, including tuning their elemental composition, constructing nanoscale hierarchical structures to increase the density of active sites, and hybridization with conductive carbon materials to improve electrical conductivity.

Dai et al. reported a Co_3O_4-N-doped reduced graphene oxides (Co_3O_4-N-rmGO) as high-performance bifunctional catalysts (Figures 2.15a, b).[199] Surprisingly, although Co_3O_4 or GO possesses poor catalytic activity, their hybrid exhibits greater activity and stability towards both ORR and OER compared to Pt/C. The X-ray absorption near-edge structure (XANES) results showed that interfacial Co-O-C and Co-N-C bonds formed in the Co_3O_4-N-rmGO, considerably enhancing the bonding environment for C, O, and Co atoms (Figure 2.15c). The high activity is due to the synergistic impact of the Co catalytic units and the N-doped rGO substrate. In another work, Chen et al. fabricated a novel type of core-shell bifunctional catalyst (CCBC) with nitrogen-doped carbon nanotubes (NCNTs) as the shell and lanthanum nickelate ($LaNiO_3$) as the core (Figures 2.15e, f).[200] The NCNTs and $LaNiO_3$ show high ORR and OER activities, respectively. Thanks to the synergistic effects between the NCNTs and $LaNiO_3$, the obtained CCBC exhibited superior catalytic activity in rechargeable ZABs, as well as outstanding cycling stability for 75 cycles without degradation.

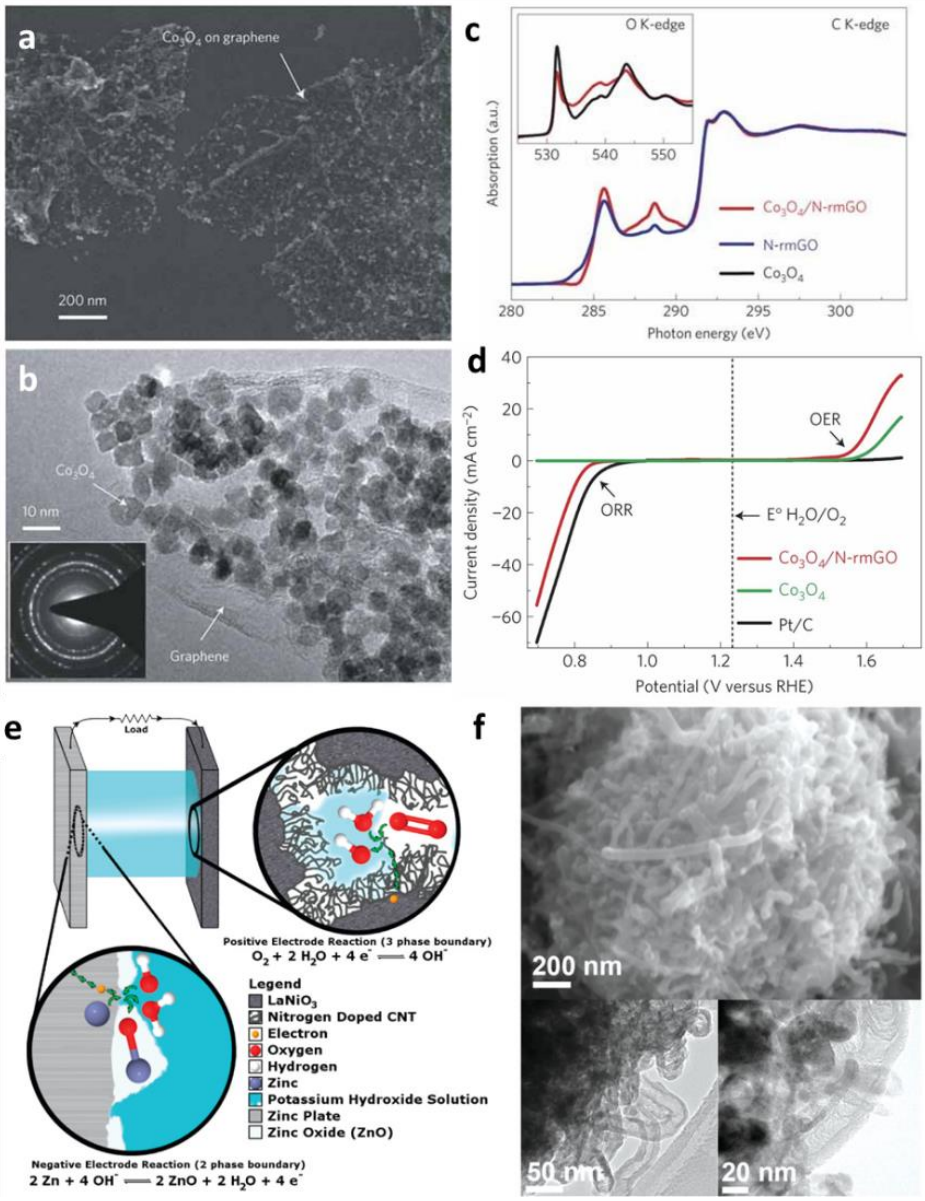

Figure 2.15. (a) SEM and (b) TEM images of the Co_3O_4-N-rmGO hybrid. (c) C K-edge XANES of the Co_3O_4-N-rmGO hybrid and N-rmGO. (d) ORR and OER potential windows of the Co_3O_4-N-rmGO hybrid, Co_3O_4 nanocrystal, and Pt/C catalysts in O_2-saturated 0.1 M KOH. Reprinted with permission.[199] (e) Schematic of the ZAB with CCBC catalyst and the reactions performing on the electrodes. (f) SEM and TEM images of the core-shell structured CCBC. Reprinted with permission.[200]

Perovskites. As a class of compounds with ABO_3 cubic crystal structure, Perovskites have been widely studied for their bifunctional catalytic activities in alkaline solutions. In general, cubic perovskite lattices are robust hosts for various mixed transition metal oxides. The A-site ions are alkali or rare

earth metals placed in the corners of the lattice, whereas the B-site ions are 3*d*, 4*d*, or 5*d* transition metal elements positioned in the center of the lattice. (Figure 2.16a).[183] In electrochemical reactions, the substitution at the A site determines the oxygen adsorption capacity of the material, while the substitution at the B site has a significant impact on the activity of adsorbing oxygen. The oxidation state of the metal can be adjusted to modify the electrocatalytic activity. Narayanan et al. reported that the binding energy of Co 2p3/2 level increases with increasing annealing temperature, which correlates with the OER activity of the catalyst.[201] The results also show that the greater the oxidation state of surface sites, the stronger the oxygen electrocatalyst's OER activity.

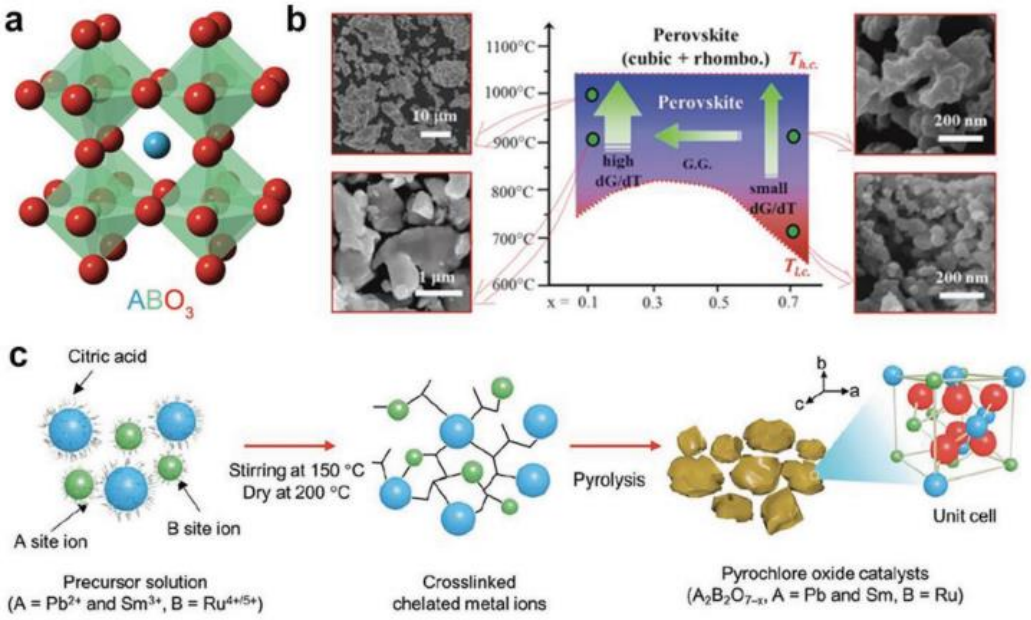

Figure 2.16. (a) Schematic of the typical ABO_3 cubic crystal structure of perovskite. Reproduced with permission.[183] (b) Phase diagram of $La_x(Ba_{0.5}Sr_{0.5})_{1-x}Co_{0.8}Fe_{0.2}O_{3-\delta}$ particle size versus La concentration and calcination temperature. Reproduced with permission.[202] (c) Schematic illustrations of the preparation of high-purity single-crystal pyrochlore oxide nanoparticles. Reproduced with permission.[203]

Additionally, increasing phase purity and decreasing crystallite size can also improve the activity of perovskites. By adjusting the La concentration and calcination temperature, Jung et al. synthesized a series of perovskite crystals $La_x(Ba0.5Sr_{0.5})_{1-x}Co_{0.8}Fe_{0.2}O_{3-\delta}$ variation in sizes (ca. 50-1000 nm) (Figure

2.16b).[202] As a result, the perovskite crystals with the size of 50 nm exhibited the highest activity and stability while the yield of H_2O_2 is below 5%. To prevent undesired perovskites phases and impurities, Park et al. proposed a facile approach to generate high-purity single crystals and conductive $Pb_2Ru_2O_{6.5}$ pyrochlore oxide nanoparticles by combining sol-gel and pyrolysis processes (Figure 2.16c).[203]

Covalent Organic Frameworks (COFs). As an emerging family of efficient bifunctional electrocatalysts, COFs have attracted widespread interest for catalyzing ORR and OER.[204-209] COFs possess a number of unique characteristics, including 1) a large surface area capable of providing sufficient active sites, 2) a periodic porous structure that can promote fast ion transport and increase the reaction rate, and 3) an abundant π-conjugated organic structure capable of improving charge carriers transport. Furthermore, COFs with robust frameworks can be considered as a superior material platform to create COF-derived materials with desirable properties for oxygen electrocatalysis.

For the first time, COFs-derived N and P co-doped carbon (denoted as RM-COP-PA-900) was synthesized by Xiang and coworkers (Figure 2.17a).[205] The resultant material showed superior bifunctional activity, excellent durability, and good resistance to the crossover effects due to the co-doping of N and P and the macroporous structure (Figures 2.17b,c). The potential difference (ΔE), characterizing the overall activity of RM-COP-PA-900, displayed a small value of 0.84 V. In addition, Jiang and coworkers also synthesized COFs-derived 2D graphitic carbons with N and P co-doping using PA as a template.[206] The obtained carbons possessed abundant N- and P-doped heteroatom catalytic edges and achieved ultrahigh activity and stability towards the ORR and OER processes.

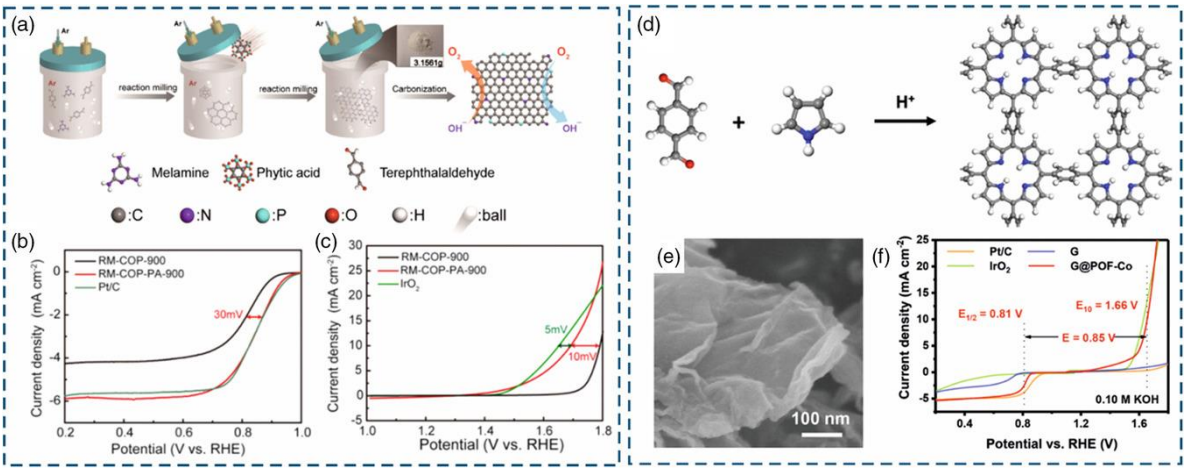

Figure 2.17. (a) Preparation of the RM-COP-PA-900 via reaction milling and carbonization processes. Corresponding (b) ORR and (c) OER activities of RM-COP-PA-900. Reproduced with permission.[205] (d) Schematic of the preparation of the G@POF-Co. (e) SEM image of G@POF-Co. (f) LSV profiles of Pt/C, IrO_2, G, and G@POF-Co towards the ORR and OER. Reproduced with permission.[206]

It is demonstrated that porphyrin-based COFs coordinated with cobalt ions (POF-Co) exhibit excellent bifunctional catalytic performance.[207-209] A big problem is the poor electrical conductivity of pristine POF-Co, as it affects catalytic efficiency significantly. Thanks to the presence of π-conjugated structures on their molecular backbones, COFs are easy to grow on conductive carbon scaffolds (e.g., CNTs or graphene) with similarly conjugated surfaces. Zhang and coworkers developed a cobalt-coordinated COF hybridized with graphene (G@POF-Co) and used it as a bifunctional electrocatalyst towards OER and ORR (Figure 2.17d).[207, 208] The COF layer was uniformly formed over the graphene surface due to the intermolecular π-π interaction between POF and graphene (Fig. 2.17e). Benefiting from the synergistic effect between the cobalt catalytic units and conductive graphene, the resultant G@POF-Co exhibits excellent bifunctional electrocatalytic activity: ORR half-wave potential of 0.81 V (vs RHE) and overpotential of only 0.85 V at 10 mA cm^{-2} (Fig. 2.17f).

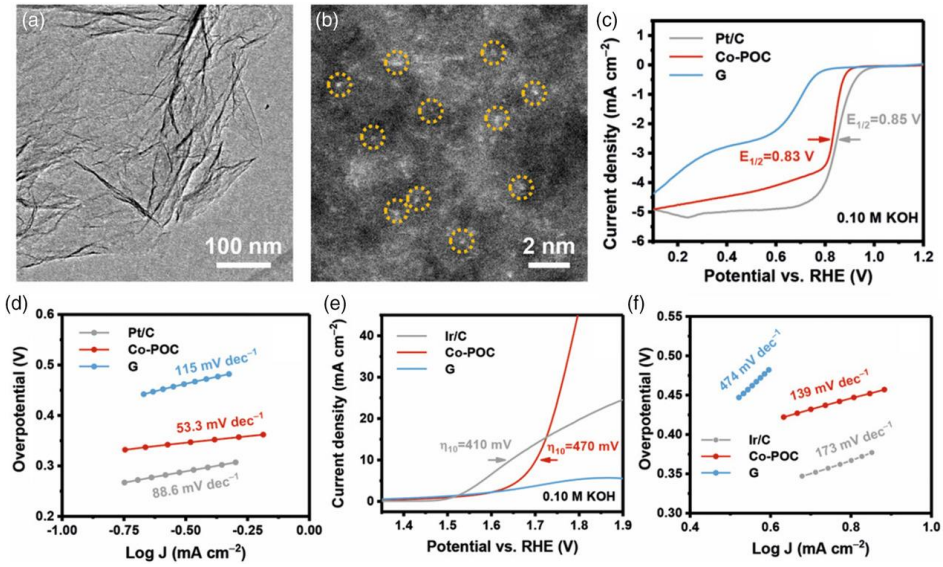

Figure 2.18. (a, b) High-resolution TEM images of Co-COF. The cobalt single atoms in Co-COF were highlighted by yellow circles. (c) ORR LSV profiles and (d) corresponding Tafel plots for various electrocatalysts. (e) OER LSV profiles and (f) corresponding Tafel plots of various electrocatalysts. Reproduced with permission.[210]

Due to their greatest atom efficiency, SACs have recently been recognized as effective electrocatalysts. Yet, the preparation of SACs materials remains difficult, necessitating substantial research into precursors with tailor-made properties. Benefiting from the designability of their molecular frameworks, COFs can coordinate with metal ions to form promising precursors for single-atom M-N-C electrocatalysts. For example, effective single-atom Co-Nx-C electrocatalysts can be obtained by pyrolysis of cobalt-coordinated COFs hybridizing with graphene (termed Co-G@COF) (Figure 2.18).[210] As a result, no aggregation of Co nanoparticles isolated cobalt single atoms were visible in the carbon framework (Figure 2.18a-b). The electrocatalyst produced had good bifunctional catalytic performance with a small overpotential gap of 0.83 V (Figure 2.18c), fast kinetics with reduced Tafel slopes (Figures 2.18d-f) and long-term durability. Such outstanding performance can be ascribed to the following three factors such as Co-coordinated catalytic units, 2D framework structure, and graphene hybridization.

Chapter 3: Covalent Organic Framework Based Catalysts for High Energy Density Zn-Air Microbattery

3.1 Introduction

On-chip smart microsystems, such as smart dust, show great potential to provide computing power that is seamlessly incorporated into the environment and accessible at any time and from anywhere.[211-213] An on-chip power source is required to drive these systems. Although renewable energy sources such as solar and wind can be gathered and turned into power, they can't be supplied stably and are only available at special times and locations.[6-9] To fully exploit the promise of energy-autonomous microsystems, microbatteries that store and release electrical power independently are highly desirable.[214] However, because microsystems are usually made from discrete components, it is difficult to check and replenish the energy units on a regular basis. Therefore, developing available on-chip power sources with with extended service durations and rigorous safety requirements necessitates the development of batteries with low environmental impact and high output energy. Zinc-air batteries (ZABs) are attractive candidates for on-chip power sources because of their safety, environmental friendliness, and high energy density.[215-217]

Over the past forty years, primary ZABs have previously been utilized to power small hearing aids devices to tight safety rules and long-term maintenance. Miniaturized rechargeable ZABs for on-chip microsystems, on the other hand, are facing significant challenging as the manufacturing technology of the battery is not compatible with on-chip processing. A typical ZAB is manufactured by progressively inserting a Zn anode, a separator, and an air cathode into a preconfigured mold, followed by filling with aqueous electrolytes (Figure 3.1a). The mold is then sealed with a ventilated cap, allowing contact with air.[218] Current effects for ZABs miniaturization have succeeded in shrinking these components, but they cell architecture remains the same.[219, 220] Maintaining the similar design for on-chip manufacturing is

challenging because it is difficult to precisely place materials in designated locations. For instance, patterning the Zn anode onto a target position is achievable with conventional photolithography procedures,[220-223] but the technology to layer down the separator and air cathode on the chip is lacking. Second, due to the semi-open structure of ZABs, the final packaging usually leaves open pores (Figure 3.1b), rendering the liquid electrolyte unusable.

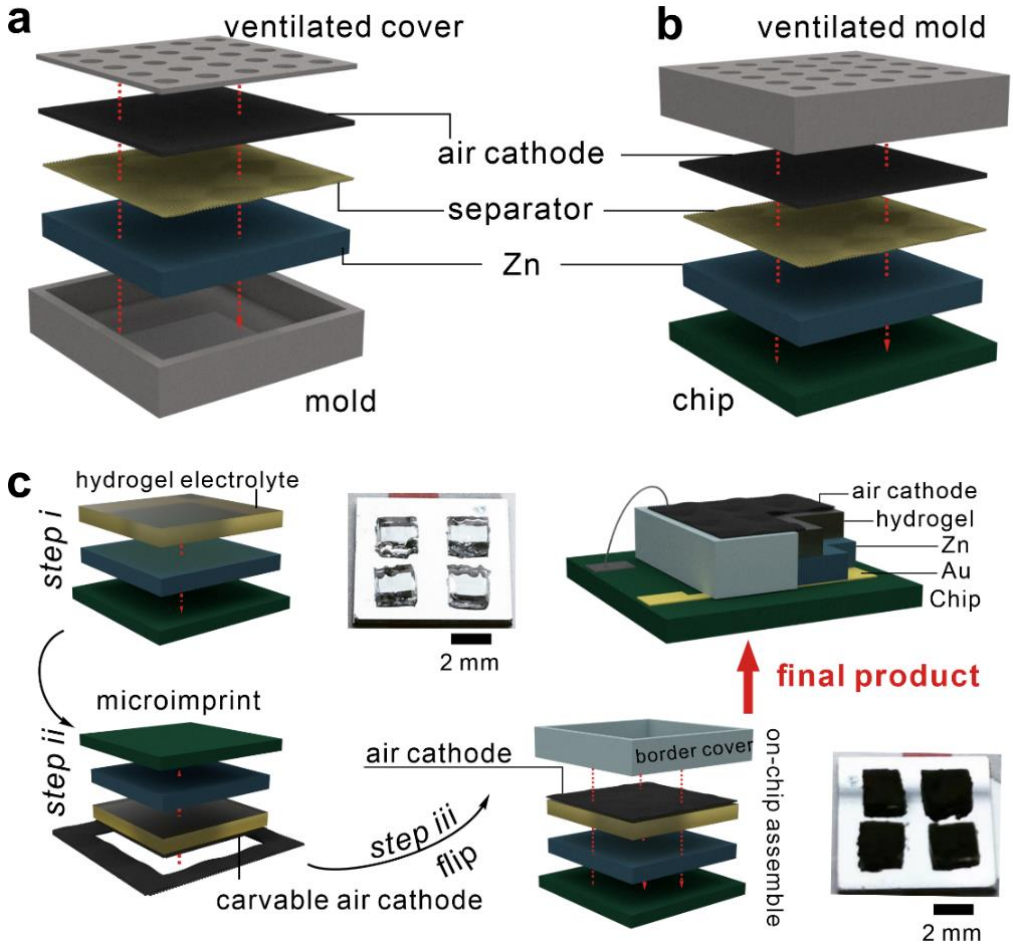

Figure 3.1. On-chip microfabrication process for COF-based Zn-air microbattery. Schematic illustrations of a Zn-air battery with (a) common multilayer architecture, (b) traditional on-chip design with the same architecture, and (c) microimprint manufacturing route (inset images show the on-chip integration of a hydrogel electrolyte and a carvable air cathode).

To address the abovementioned manufacturing issues, we reported a microimprint technique capable of positioning a bifunctional air cathode at a target position. To this end, a highly sticky hydrogel electrolyte is in-situ polymerized and patterned on the chip, thus solving the problem that on-chip

devices aren't compatible with liquid electrolytes (Figure 3.1c, step i). Specifically, a hydrogel (2×2 mm^2) array was first patterned on a chip with the size of 10×10 mm^2. Such a hydrogel can then be used as the electrolyte for rechargeable on-chip ZABs. Subsequently, the chip is flipped and imprinted onto a carvable air cathode (Figure 3.1c, step ii), achieving a good match between the air cathode and patternable hydrogel electrolyte in terms of the position and dimension. This alternate top-down technique avoids the difficulty of on-chip integration with the air cathode (Figure 3.1c, step iii). Furthermore, the construction process can be completed by flipping the hydrogel again and closing the outer boundaries to increase liquid electrolyte retention.

It is well-known that the rechargeability of ZABs is mainly achieved through oxygen redox electrochemistry occurring on air cathodes. Generally, a porous and electrically conductive air cathode is required and highly appealing to catalyze oxygen electrocatalysis.[171, 224-226] Freestanding carbon nanotubes (CNTs) films are porous and mechanically flexible, which are good hosts for electrocatalysts. At the same time, they can be torn apart and therefore are promising candidates for carvable air cathodes. As for the catalysts, precious metal catalysts have the issues of high cost and low durability, which greatly hinders their widespread application.[227] Alternatively, covalent organic frameworks (COFs) with periodic pore structures can be formed by strong covalent linkages, exhibiting high programmability and stability in predesigning catalytic functions.[228, 229] At the same time, COFs have efficient gas permeability and ion conductivity, thereby promoting the ORR and OER processes taking place at the three-phase interface.[230-232] Furthermore, due to the intermolecular π–π interactions, COFs can be hybridized with CNT hosts to form hybrid materials.[233] All these merits endow COFs with superior catalytic properties as compared to the mixture of the catalyst and the host material.

Hence, we report the fabrication of an on-chip Zn-air microbattery (μZAB) using a microimprint technique in conjunction with a high-performance COFs-based air cathode. The carvable air cathode was synthesized by incorporating cobalt (Co) catalytic units into a porphyrin organic covalent framework (POF), followed by hybridizing with CNT hosts. The catalytic activity of the CoPOF can be improved by tuning the C-N binding and the Co valence. Subsequently, we developed a carvable air cathode with a CNT-based gas diffusion layer (GDL) through a two-step filtration process. The resulting air cathode in a hydrogel (polyvinyl alcohol networking with polyacrylic acid, PVA-co-PAA)

electrolyte, exhibited a high peak power density of 89 mW cm^{-2} and a stably operation for 110 hours. As a result, the on-chip μZAB shows a record-high volumetric power density of 570 mW cm^{-3} and energy density of 413 Wh L^{-1}, approximately 3 times that of a commercial primary ZAB. The on-chip μZAB also achieves a lifecycle capacity of 4.5 mAh, which is double that of the smallest commercially available on-chip lithium-ion batteries.[234] We also show that the μZAB can run complicated electronic devices and can wirelessly recharged for prolonging the lifespan .

3.2 Experimental Methods

Materials

Carbon nanotube (CNT, 500-1000 μm) was purchased from NANOGRAFI Co. Ltd, America. Pyrrole (min. 98.0%), acetic acid (min. 99.5%), benzene-1,4-dialdehyde (BDA) (min. 99.0%), trifluoroacetic acid (min. 99.0%) and nitrobenzene (min. 99.0%) were all received Sigma-Aldrich. Polyvinyl alcohol (PVA) powder (Mw=89000-98000, 99+% hydrolyzed) and cobalt acetate (99.99%) were purchased from The Geyer. The carbon cloth was purchased from CoTech Co., Ltd.

Synthesis of CoPOF@CNTs

CoPOF@CNTs were fabricated by in-situ growth of CoPOF thin layer onto the CNT scaffold following an acid-catalyzed dehydration reaction. Typically, the mixture of CNT (50 mg), 100 mL of acetic acid, and 50 μL of trifluoroacetic acid was ultrasonicated for 60 min to form a homogenous suspension. Thereafter, reagents including 18.2 μL of pyrrole, 0.90 mL of nitrobenzene, 17.4 mg of BDA, and 24.9 mg of $Co(OAc)_2$ were added into the suspension in turns, followed by ultrasonicated for another 30 min. The final mixture was transferred to a round-bottom flask and held at the desired temperatures (e.g., 80, 100, and 120 ℃) for 24 h under magnetic stirring and reflux. Finally, the as-obtained product was filtrated, washed with ethanol three times, and then vacuum-dried at 60 ℃ overnight.

Fabrication of CoPOF@CNT air cathodes

CoPOF@CNTs catalysts (10 mg) and Nafion solution (5.0 wt.%, 100 μL) were mixed in isopropanol (1.9 mL) and then ultrasonicated for 30 min to produce a homogenous catalyst ink. Subsequently, 1 mL of catalyst ink was coated onto a carbon cloth via a drop-casting method and vacuum-dried overnight.

For comparison, 5 mg of 20 wt.% Pt/C and 5 mg of 20 wt.% Ir/C are mixed to prepare Pt/C+Ir/C air cathodes instead of 10 mg of CoPOF@CNT catalyst. The mass loading is controlled at 1.15 mg cm^{-2}.

Fabrication of carvable and freestanding CoPOF@CNT air cathodes

The freestanding CoPOF@CNT electrodes were fabricated via a two-step vacuum filtration method. First, CNT suspension (2 mg mL^{-1}, 20 mL) was vacuum-filtrated. Subsequently, the homogenous catalyst suspension (8 mg CoPOF@CNT or Pt/C+Ir/C in 20 mL of isopropanol) was filtrated. The as-obtained membrane with a two-layer structure was then vacuum-dried at 60 ℃ overnight and peeled from the nitrocellulose membrane. The air cathode without GDL is fabricated by one-step filtration. The catalyst mass loading in all freestanding CoPOF@CNT air cathodes is about 2.0 mg cm^{-2}.

Synthesis of the hydrogel electrolyte

NaOH (20 M, 0.8 mL) solution was drop-wisely added into acrylic acid (1 mL) solution under an ice bath to form a transparent suspension. The obtained suspension was then mixed with PVA (5.0 wt.%, 2 mL) under vigorous stirring, followed by the addition of 0.1 wt.% N, N'-methylenebisacrylamide as the crosslinker, and α-ketoglutaric acid (0.1 g mL^{-1}, 100 μL) as the photoinitiator. Subsequently, the transparent suspension was purged with nitrogen gas and then exposed to UV irradiation (365 nm) for 2 h to form a PVA-co-PAA gel electrolyte.

Fabrication of the on-chip μZAB

Figure 3.2 displays the fabrication process of the on-chip μZAB. Firstly, silicon wafers were etched by reactive ion etching (RIE) (Plasma Lab 100; Oxford Instruments PLC, Abingdon, UK). Before the etching process, SU8-10 with 20 μm in thickness was spin-coated on the silicon wafer, followed by baking at 65 ℃ for 3 min and 95 ℃ for 5 min. The patterning process was then performed using a maskless aligner (MLA 100, Heidelberg Instruments Mikrotechnik GmbH). The patterned sample was baked at 95 ℃ and 150 ℃, respectively. The etching depth is controlled to be 60 μm. The current collector of 10 nm Cr and 50 nm Au were deposited using magnetron sputtering (nanoPVD-S10 A). A thick zinc film was electrodeposited on the surface of silicon arrays using a three-electrodes system, achieving a 3D zinc anode. Afterward, the precursor solution of PVA-co-PAA was coated on the zinc layer and polymerized under UV light (365 nm). The chip was then flipped over and imprinted onto the

carvable CoPOF@CNT film. Benefiting from the strong adhesion between CoPOF@CNT and PVA-co-PAA hydrogel, a small piece of the CoPOF@CNT film will be torn off and match the hydrogel dimension.

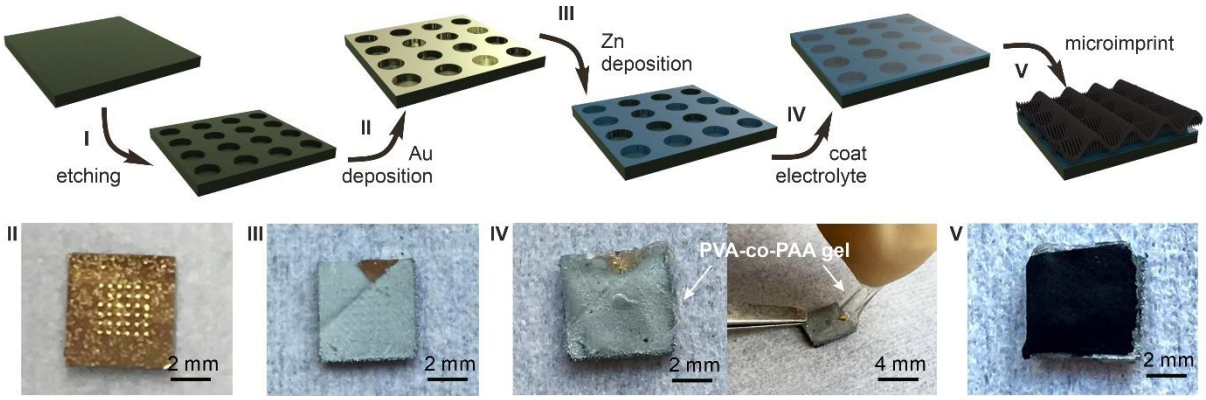

Figure 3.2. Schematic illustration of the μZAB fabrication process, including (I) etching silicon wafer, (II) Au deposition, (III) Zn deposition, (IV) electrolyte coating, and (V) microimprint process.

Materials Characterization

The morphologies and microstructures of the CoPOF-based catalyst were studied using LEO Supra-35 (Carl Zeiss AG, Germany) scanning electron microscope (SEM) operating at 5 kV and CM 12 (Philips, The Netherlands) transmission electron microscope (TEM) operating at 120.0 kV. Raman spectroscopy (LabRAM HR Evolution, HORIBA Scientific) was measured with a laser of 458 nm. X-ray diffraction (XRD) tests were conducted on Philips X'Pert PRO MPD diffractometer (Co Kα radiation, $\lambda = 1.5418$ Å). X-ray photoelectron spectroscopy (XPS) measurements were performed on a PHI VersaProbe II (Ulvac-phi, Inc., Chigasaki, Japan) using a monochromatic Al-Kα source (1486.6 eV) and a power of 100 W by a Thermal Scientific Al Kα XPS spectrometer.

Electrochemical measurements

The ORR and OER activity of the catalysts were evaluated in a standard three-electrode cell using a PINE rotating ring disk electrode (RRDE). The reversible hydrogen electrode (RHE) potential was used to calibrate all the potentials. The ORR and OER performance of the catalysts were evaluated at 1600 rpm in 0.1 M O_2-saturated and 1 M N_2-saturated aqueous KOH solutions. The catalyst loading is

estimated to be around 0.1 mg cm^{-2}. Galvanostatic discharge-charge cycling experiments were performed on a battery test station (Arbin, BT2000) in a room-temperature ambient environment. The polarization profiles were measured using linear sweep voltammetry (LSV) on the electrochemistry workstation (MULTIAUTOLAB/M101, Metrohm Autolab).

3.3 Results and Discussions

The CoPOFs are expected to form a stably and uniformly coating on CNT hosts via the strong intermolecular π–π interaction. To this end, CoPOF@CNTs were synthesized by first dehydrating pyrrole and benzene-1,4-dialdehyde (BDA) to form the POF precursor, and then hybridizing with CNTs and coordinating with Co ions (Figure 3.3a). Porphyrin units can be linked via benzene linkages and then coordinate with Co ions. In the absence of CNT hosts, porphyrin molecules tend to aggerate and then form CoPOF nanospheres with diameters of 20-50 nm. The dense morphology of pristine CoPOF results in limited exposed active sites and is undesired as an air cathode for ZAB. To fully unleash the potential of the CoPOFs, CNTs were explored as a conductive scaffold to support the growth of CoPOFs. As a result, a uniform and smooth CoPOF coating was obtained at 80 ℃ (Figure 3.3b), which facilitates the charge transfer between the CNT host and the CoPOF catalyst. At higher synthesis temperatures (i.e., 100 °C and 120 °C), however, substantial aggregation of the CoPOF spheres on the surface of CNTs was observed on the surface of CNTs due to excessive growth.

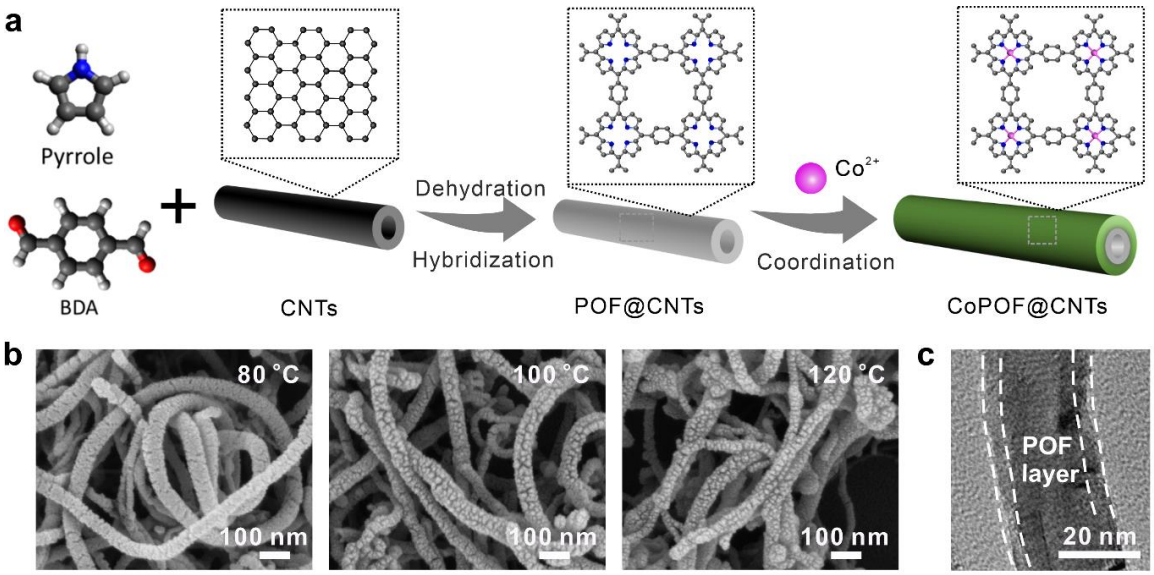

Figure 3.3. Preparation and morphology characterization of CoPOF@CNTs. (a) Synthesis of the CoPOF@CNT catalysts. (b) SEM images of the CoPOF@CNT catalysts synthesized at various temperatures. (c) TEM image of the CoPOF@CNT catalyst synthesized at 80 ℃.

The formation of the CoPOFs was proofed by X-ray diffraction (XRD) and Fourier-transform infrared spectra (FTIR) measurements. XRD spectra exhibited two peaks located at 30° and 50°, originating from the (002) and (100) crystal planes of the CNT host (Figure 3.4a). A broad diffraction peak at 21° stems from CoPOF. The peaks in FTIR spectra ranging from 1578-1630 cm^{-1} were ascribed to the C=N bondings in porphyrin (Figure 3.4b), confirming the formation of CoPOF.[210, 233] The existence of C, N, and Co elements was detected using X-ray photoelectron spectroscopy (XPS) (Figure 3.4c and Table 3.1). The high-resolution N1s spectra (Figure 3.4d) revealed that the CoPOF@CNTs has three types of N-moieties such as graphitic-N (401.3 eV), pyrrolic-N (400.2 eV), and Co-N (398.8 eV).[196, 210, 233] The graphitic-N stemmed from the possible N-doping of the CNT during the synthesis process,[207] while pyrrolic-N and Co-N further confirmed the formation of the CoPOF. The high-resolution Co 2p spectrum (Figure 3.4d) showed two characteristic broad peaks of Co 2p1/2 at 797.2 eV and Co 2p3/2 at 781.1 eV. Both peaks can be further fitted into four peaks at 780.9, 782.5, 786.1, and 789.1 eV, which can be attributed to Co^{III}, Co^{II}, and satellite peaks for Co^{II} and Co^{III} (Figure 3.4e), respectively.[235, 236]

The synergistic impact of the Co-N coordination and balanced Co^{III} species have been demonstrated to provide superior catalytic performance.[28, 237-239]

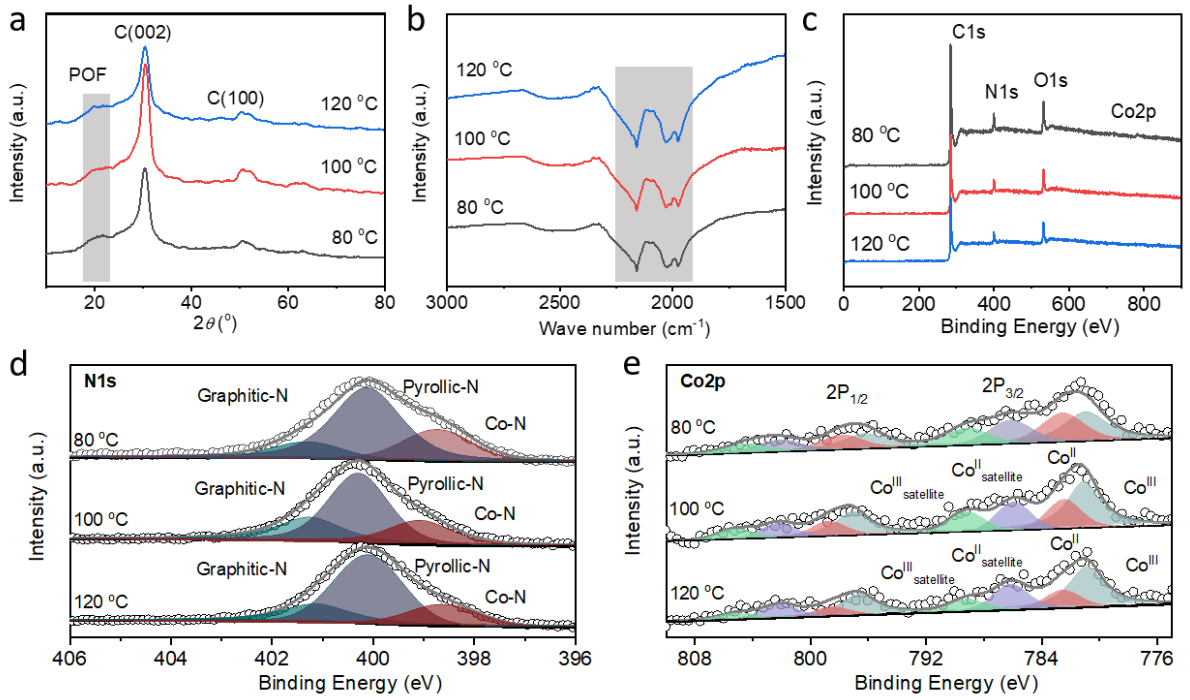

Figure 3.4. Composition characterization of the CoPOF@CNTs. (a) XRD pattern and (b) FTIR spectra of CoPOF@CNTs. (a) XPS survey spectra of CoPOF@CNTs synthesized at 80, 100, and 120 ℃. High-resolution XPS spectra of (b) N1s and (c) Co2p synthesized at 100 ℃ and 120 ℃, respectively.

Table 3.1. Summary of element composition of CoPOF@CNTs synthesized at various temperatures.

Reaction temperatures	Relative amounts of elements (at. %)			
	C	N	O	Co
80 °C	86.81	5.48	7.53	0.18
100 °C	86.41	5.64	7.84	0.12
120 °C	84.81	6.54	8.56	0.10

Raman analyzes were further introduced to investigate the interaction between the CNT host and the CoPOF unit (Figure 3.5). Raman spectra showed a G-band at 1592 cm^{-1} and a D-band at 1364 cm^{-1}, which corresponded to the sp^2 hybridized carbon and the sp^3 hybridized carbon or defects, respectively. A resonant 2D band at 2720 cm^{-1} was also observed as a result of the D-band overtone.[240] Notably, the CoPOF@CNT displayed a shoulder peak at 1570 cm^{-1}, suggesting the presence of sp^2 hybridized carbon atoms. Furthermore, the intensity ratios of the G to D band (I_G/I_D) and the G to 2D band (I_G/I_{2D}) increased substantially upon hybridization to the CoPOF (inset in Figure 3-3). This phenomenon demonstrates that the CoPOF and the CNT host have strong intermolecular conjugated interactions.[241]

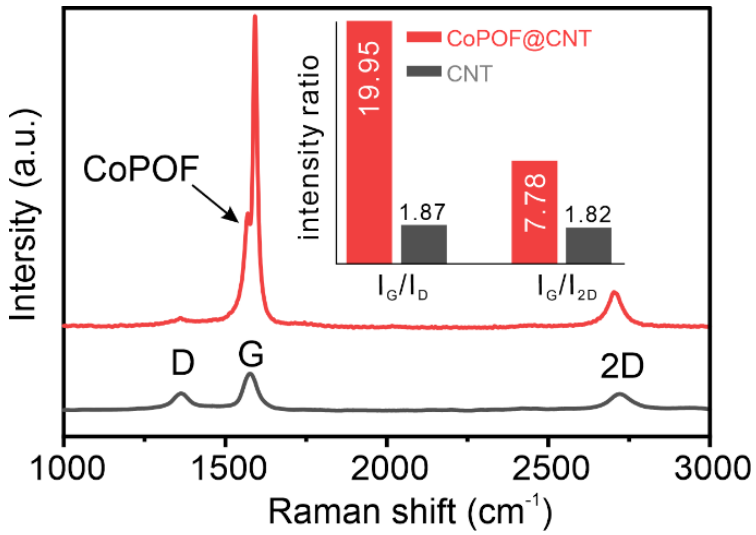

Figure 3.5. Raman spectra of the CoPOF@CNT synthesized at 80 °C. The inset is the ratio of I_G/I_D and I_G/I_{2D}.

Given the highly desirable characteristics of the CoPOF@CNTs, electrochemical evaluation was performed to probe their ORR and OER activity. Linear sweep voltammetry (LSV) was first used to measure the catalytic activity of CoPOF@CNTs in 0.1 M O_2- or N_2-saturated KOH electrolyte. LSV curves of ORR reveal that half-wave potentials ($E_{1/2}$) of the CoPOF@CNT increase with the elevating synthesis temperatures (Figure 3.6a). The CoPOF@CNTs catalyst synthesized at 80 °C exhibited the best ORR activity with half-wave potential of 0.70 V (vs. RHE) than the Pt/C catalyst (0.72 V vs. RHE). The Tafel slope of ORR for the CoPOF@CNT synthesized at 120 °C reaches 118 mV dec^{-1}, whereas

the values for those synthesized at 80 and 100 °C are 78 and 81 mV dec^{-1} (Figure 3.6b), respectively. By contrast, a benchmark Pt/C+Ir/C catalyst delivers a typical slope of 71 mV dec^{-1}. In terms of the OER activity, the overpotentials at 10 mA cm^{-2} (η_{10}) for CoPOF@CNTs and Ir/C catalysts are 390, 370, 440, and 320 mV (Figure 3.6c), respectively. The CoPOF@CNT synthesized at 80 and 100 °C shows the slopes of 132 and 130 mV dec^{-1}, close to the Ir/C (127 mV dec^{-1}).[196, 207, 242-244] The synthesized sample at 120 °C also demonstrates a noticeable decline of OER kinetics as shown by a large Tafel slope of 161 mV dec^{-1} (Figure 3.6d).

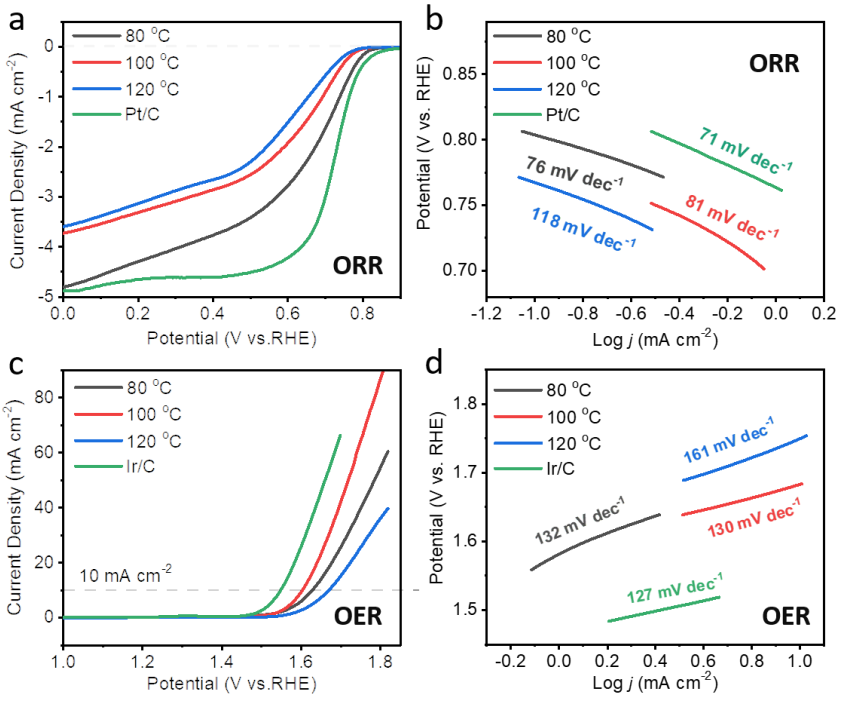

Figure 3.6. Electrocatalytic activities of the CoPOF@CNTs. (a, c) LSV curves and (b, d) Tafel slopes of the CoPOF@CNT and the corresponding benchmark catalysts towards the ORR and OER.

As shown in Figure 3.7, the potential gap between $E_{1/2}$ and η_{10} of the CoPOF@CNT, evaluating the overall catalytic performance, shows a smaller potential gap of 0.91 V than that of Pt/C (1.12 V) and Ir/C catalysts (1.03 V). In contrast, the mixture catalyst (Pt/C+Ir/C) with the same mass loading also shows a larger potential gap of 0.96 V than the CoPOF@CNT. Correspondingly, the CoPOF@CNT synthesized at 80 °C demonstrates the best bifunctional electrocatalytic reactivity among CoPOF@CNT samples. The enhanced catalytic activity can be ascribed to the following reasons. In terms of materials

structure, the TEM image of CoPOF@CNT synthesized at 80 °C demonstrates a uniform CoPOF coating on the surface of CNTs (Figure 3.3c), giving rise to fast charge transfer. At the molecular level, the Co-N coordination and the Co valence state have been demonstrated to determine the catalytic activities. In the CoPOF design, Co is coordinated to four N atoms forming Co-N_4 moieties, which offers high catalytic activity. The Co content decreases along with increasing synthesis temperature (Table 3-1), resulting in the degradation of the catalytic activity.

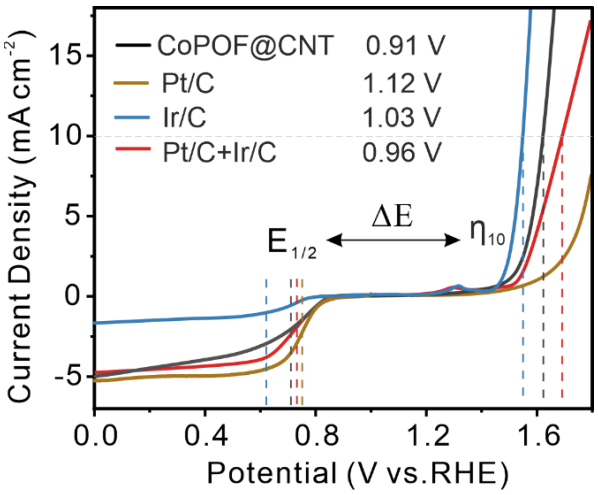

Figure 3.7. LSV profiles of various catalysts for evaluating the overall catalytic performance.

Based on the observations and results presented so far, the optimal catalyst is the CoPOF@CNT synthesized at 80 °C and used for further measurements. A conventional aqueous ZAB was then assembled using a zinc foil anode, 6 M KOH aqueous electrolyte, and a CoPOF@CNT based air cathode. For comparison, the benchmark Pt/C+Ir/C cathode was also fabricated using the same procedures. The areal mass loading is 1.15 mg cm^{-2} for all catalysts. At all current densities, the CoPOF@CNT delivers higher discharging voltages than the Pt/C+Ir/C catalyst (Figure 3.8a), demonstrating superior rate performance. The peak power density of the CoPOF@CNT cathode is 140 mW cm^{-2}, which is much greater than the Pt/C+Ir/C cathode (87.3 mW cm^{-2}, Figure 3.8b). In addition, the CoPOF@CNT can survive for over 3000 cycles corresponding to over 1000-hour operation at 2.0 mA cm^{-2} (Figure 3.8d), indicating extraordinary cycling stability. In comparison, the Pt/C+Ir/C cathode only lasts around 690 cycles or 250 hours. Impressively, the CoPOF@CNT achieves a high round-trip efficiency of ~79.3% at the initial cycle, and slightly decreases to 69.7% after 3000 cycles (Figure 3.8e). Even at a higher

current density of 5.0 mA cm^{-2}, the CoPOF@CNT catalyst maintains long-term cycling stability of about 2000 cycles (corresponding to 640 hours) and no obvious degradation is observed (Figure 3.8f). The significantly enhanced stability demonstrates that the synergistic effects of highly-active catalytic units and the robust hybrid structure contribute to a high-performance catalyst.

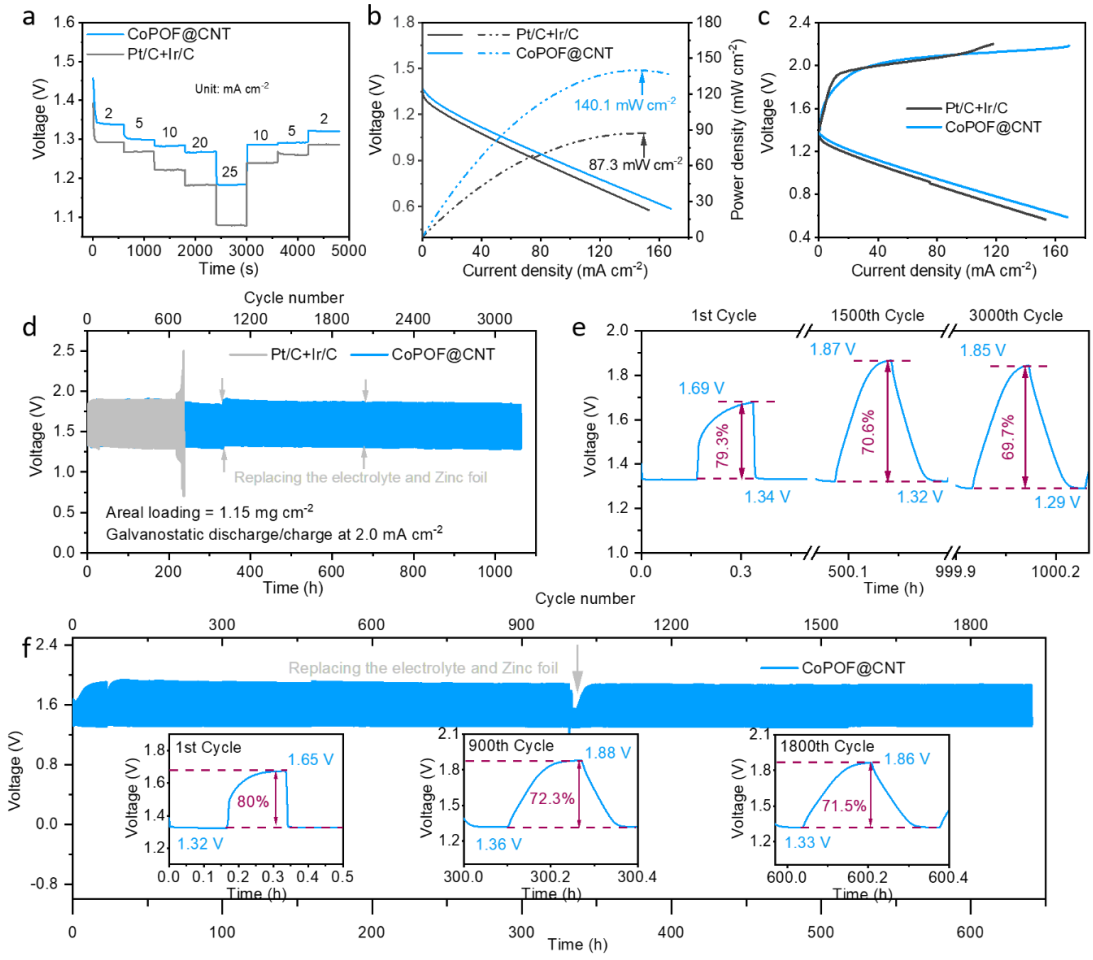

Figure 3.8. Aqueous ZAB performance of the CoPOF@CNT and the Pt/C+Ir/C cathodes. (a) Rate performance, (b) discharging polarization profiles, and (c) discharge-charge voltage profiles for the CoPOF@CNT and the Pt/C+Ir/C cathodes. Cycling stability of the CoPOF@CNT cathode at current densities of (d) 2.0 mA cm^{-2} and (f) 5.0 mA cm^{-2}. (e) Corresponding round-trip efficiency of the CoPOF@CNT cathode at various cycling stages in (d).

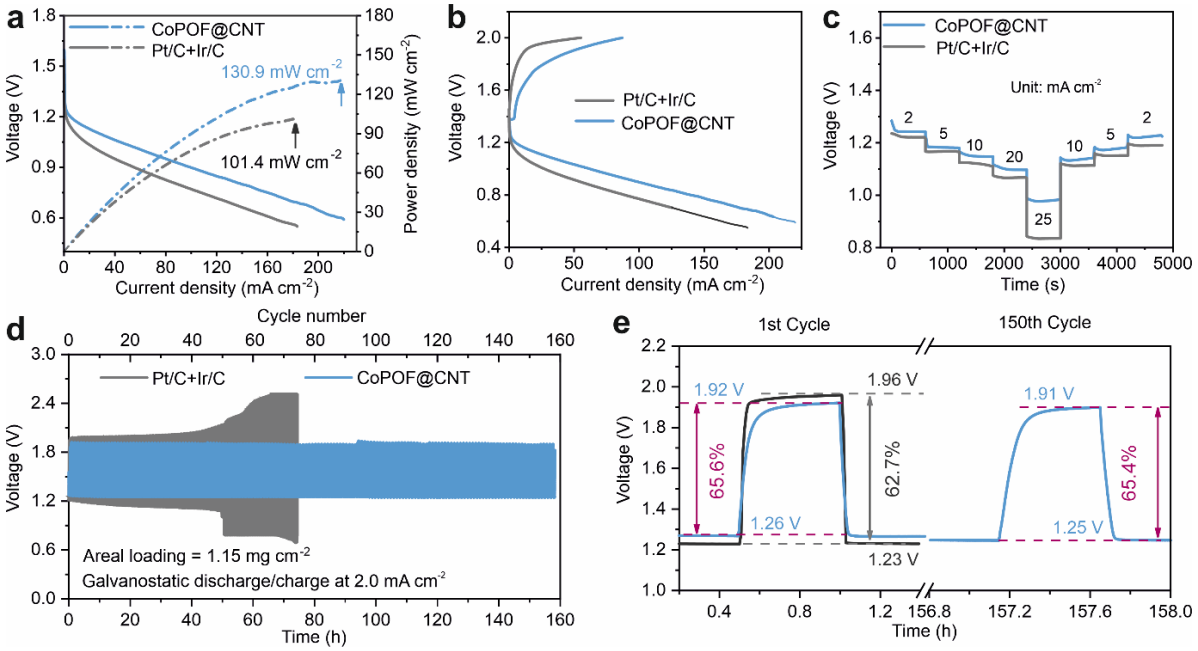

Figure 3.9. Quasi-solid-state ZAB performance of the CoPOF@CNT and the Pt/C+Ir/C cathodes. (a) Discharge polarization profiles, and (b) discharge and charge voltage curves of the CoPOF@CNT and the Pt/C+Ir/C cathodes. (c) Rate performance and (d) cycling stability of the CoPOF@CNT and the Pt/C+Ir/C cathodes in quasi-solid-state ZABs. (e) Round-trip efficiencies at the first cycle and the 157th cycle of CoPOF@CNT and Pt/C+Ir/C cathodes.

The outstanding performance in the aqueous electrolyte is projected to be maintained effectively in the hydrogel electrolyte. Thus, we constructed a quasi-solid-state ZAB using a PVA-co-PAA hydrogel electrolyte saturated with 6M KOH. The PVA-co-PAA hydrogel is chosen due to its excellent water retention properties.[245, 246] As a result, the CoPOF@CNT cathode delivered a high peak power density of 131 mW cm^{-2} (Figure 3.9a), about 30% higher than the Pt/C+Ir/C cathode (101 mW cm^{-2}).[247, 248] The CoPOF@CNT cathode exhibited a higher discharge voltage and a lower charge voltage than the Pt/C+Ir/C cathode (Figure 3.9b). Furthermore, at all current densities, the CoPOF@CNT cathode in the hydrogel electrolyte also showed higher discharges voltage than the Pt/C+Ir/C cathode (Figure 3.9c), indicating better rate performance. Likewise, the CoPOF@CNT cathode has excellent long-term cycling stability in the hydrogel electrolyte. The CoPOF@CNT cathode in the hydrogel electrolyte can stably run for over 150 cycles (Figure 3.9d). Accordingly, the CoPOF@CNT cathode attained a round-

trip efficiency of 65.6% and slightly reduced to 65.4% as the battery cycles (Figure 3.9e), indicating a high energy utilization throughout the service time. By contrast, the Pt/C+Ir/C cathode started to degrade after 50 hours and failed in less than 80 hours. These results clearly demonstrate that the CoPOF@CNT cathode hold promise in practical applications for both liquid and quasi-solid-state ZABs.

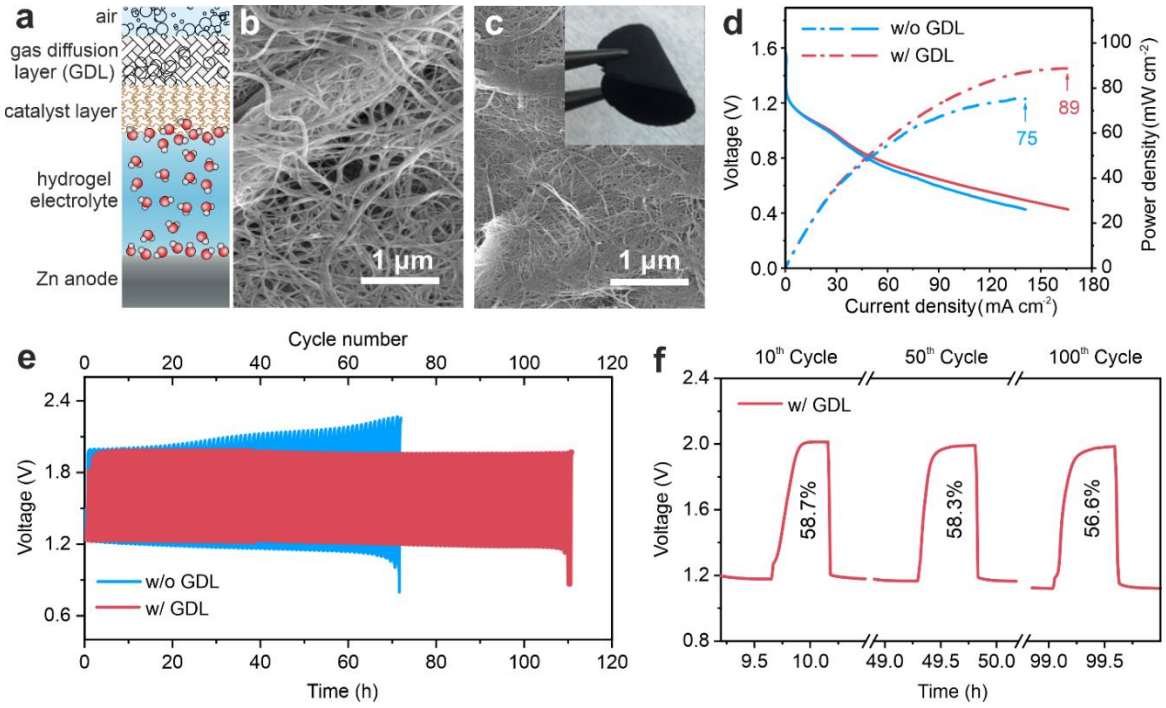

Figure 3.10. Improved performance by designing a CNT-based GDL. (a) Schematic of the air cathode architecture of quasi-solid-state ZAB. SEM images of (b) the porous CNT-based GDL and (c) the CoPOF@CNT catalyst layer. (d) Polarization profiles and (e) cycling performance of freestanding CoPOF@CNT cathodes designed with and without GDL. (f) Energy efficiencies of the freestanding CoPOF@CNT cathodes with GDL at various cycles.

To enable the potential applications in on-chip processing, a carvable and freestanding air cathode based on the CoPOF@CNT catalyst was further fabricated in the quasi-solid-state battery. Generally, a standard air cathode is made up of a catalyst layer and a hydrophobic porous gas diffusion layer (GDL) that allows for gas diffusion, facilitating oxygen redox reactions at the three-phase boundary (Figure 3.10a). A two-step filtration process was created to imitate this bilayer structure via filtering the CNT dispersion to a porous membrane as the GDL (Figure 3.10b), followed by coating the CoPOF@CNT

catalysts to create the catalyst layer (Figure 3.10c). The CNT GDL has a more open structure than the catalyst layer, which creates abundant pore for providing sufficient supply of oxygen. After peeling off the filter paper, the obtained freestanding air cathode is mechanically flexible without any damage or cracking under deformations (inset in Figure 3.10c). The freestanding CoPOF@CNT cathode with the GDL (denoted as w/ GDL) was employed directly as the air cathode without the current collector because of its inherent mechanical flexibility and abundance of internal gas channels.

Figure 3.10d demonstrates that the peak power density of freestanding CoPOF@CNT cathodes with GDL achieves 89 mW cm^{-2}, about 18% higher than the one without the GDL (termed as w/o GDL). As far as we know, such a high power density is superior to most of freestanding air cathodes previously reported (Table 3.2).[196, 233, 247, 249-253] Notably, a 35% increase in the peak power density can be achieved by utilizing the CoPOF@CNT catalyst as compared to the simple mixing of CNTs and the Pt/C+Ir/C catalyst (Figure 3.11a). The remarkable improvement can be attributed to the molecular-level engineering of the catalytic units in the stable POF, and intermolecular interconnection with the conductive material. The long-term cycling stability of cavable CoPOF@CNT cathode were tested at 2.0 mA cm^{-2} (Figure 3.10e). Initially, the freestanding cathodes with and without the GDLs show a same voltage gap of around 0.8 V. However, the voltage gap of the one without GDL significantly increases to 1 V after 50 cycles and renders the failure of ZAB after 70 cycles. In contrast, the cathode with GDL displays stable cycling for more than 100 cycles with a negligible increase in the voltage gaps (ca. 0.03 V after 100 cycles). Correspondingly, the round-trip efficiency exhibited a slightly decrease with only 0.4 % after 50 cycles and 2.1% after 100 cycles (Figure 3.10f). As for the cathode without GDL, the round-trip efficiency quickly drops from 60% at the 10^{th} cycle to 48% at the 69^{th} cycle (Figure 3.11b).

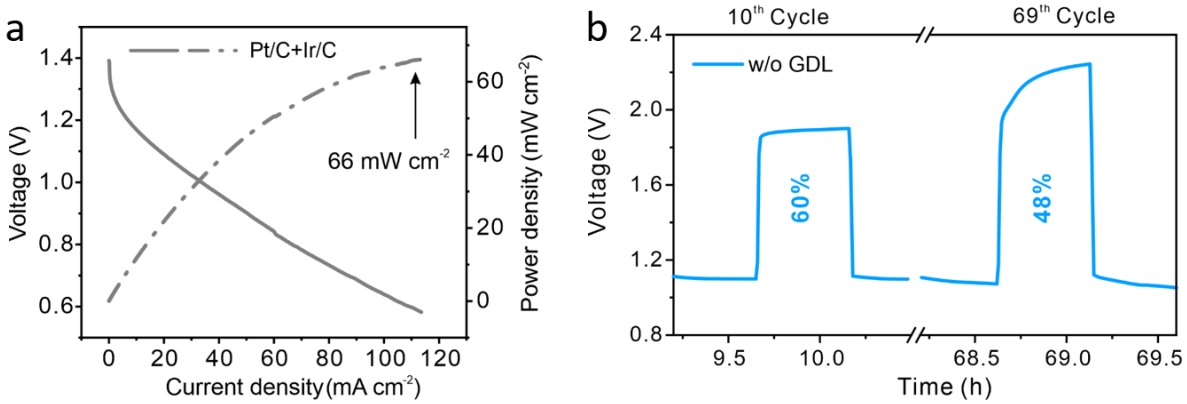

Figure 3.11. (a) Polarization curve of the cathode based on a simple mixture of the CNTs and the Pt/C+Ir/C catalyst. (b) Corresponding round-trip efficiencies of CoPOF@CNT cathode without GDL.

Table 3.2. The performance of rechargeable quasi-solid-state ZABs with freestanding air cathodes.

Cathodes	Voltage gap (V) @ current density (mA cm^{-2})	Peak power density (mW cm^{-2})	Cycling stability @ current density (mA cm^{-2})	Ref.
Co/N@CNTs@ CNMF-800	0.68 @ 1.0	26.5	100 cycles @ 1.0	[252]
CNT/POF	0.76 @ 1.0	22.3	------	[233]
CoNCNTF/CNF	-----	63	68 cycles /11 h @ 0.5	[250]
Co-NC@Al_2O_3 /CC	0.79 @ 2	72.4	10 h @ 20	[253]
N-GCNT/FeCo/CC	1.42 @ 120	97.8	240 cycles /24 h @ 20	[196]
NC-Co_3O_4-90/CC	-----	82.0	20 h @ 1.0	[249]
Co-FeCo/N-G	0.61 @ 1.0	82.0	18 h @ 1.0	[251]
Meso-CoNC@GF	1.04 @ 20	85.6	70 cycles @ 20	[247]
CNT@CoPOF-80/G	0.83 @ 2.0	89.0	110 cycles /110 h @ 2.0	**This work**

The on-chip Zn-air microbattery (μZAB) consists of a Zn anode on the chip with a 3D microstructure to expand the contact area between the hydrogel and Zn anode (Figure 3.12a). Experimental Methods shows the complete technique for each stage as well as the associated digital photographs. It has been

reported that the adoption of 3D Zn anodes can efficiently improve the cycling stability.[219, 254-256] To do so, a 3D structure with periodic holes 200 m in diameter and 60 m in depth was selectively etched from a silicon wafer. Subsequently, a thin gold layer of gold with a thickness of 50 nm was deposited as a current collector, followed by electrodepositing zinc onto the gold layer to obtain a 3D Zn anode. Then a PVA-co-PAA gel electrolyte with a thickness of one millimeter was applied to the surface of Zn anode through a photopolymerization method. The final step was completed by flipping the chip and embossed on the carvable CoPOF@CNT film. Because of the strong adhesion of the PVA-co-PAA gel, the freestanding air cathode can be firmly attached to the gel and subsequently separated from the leftover components.

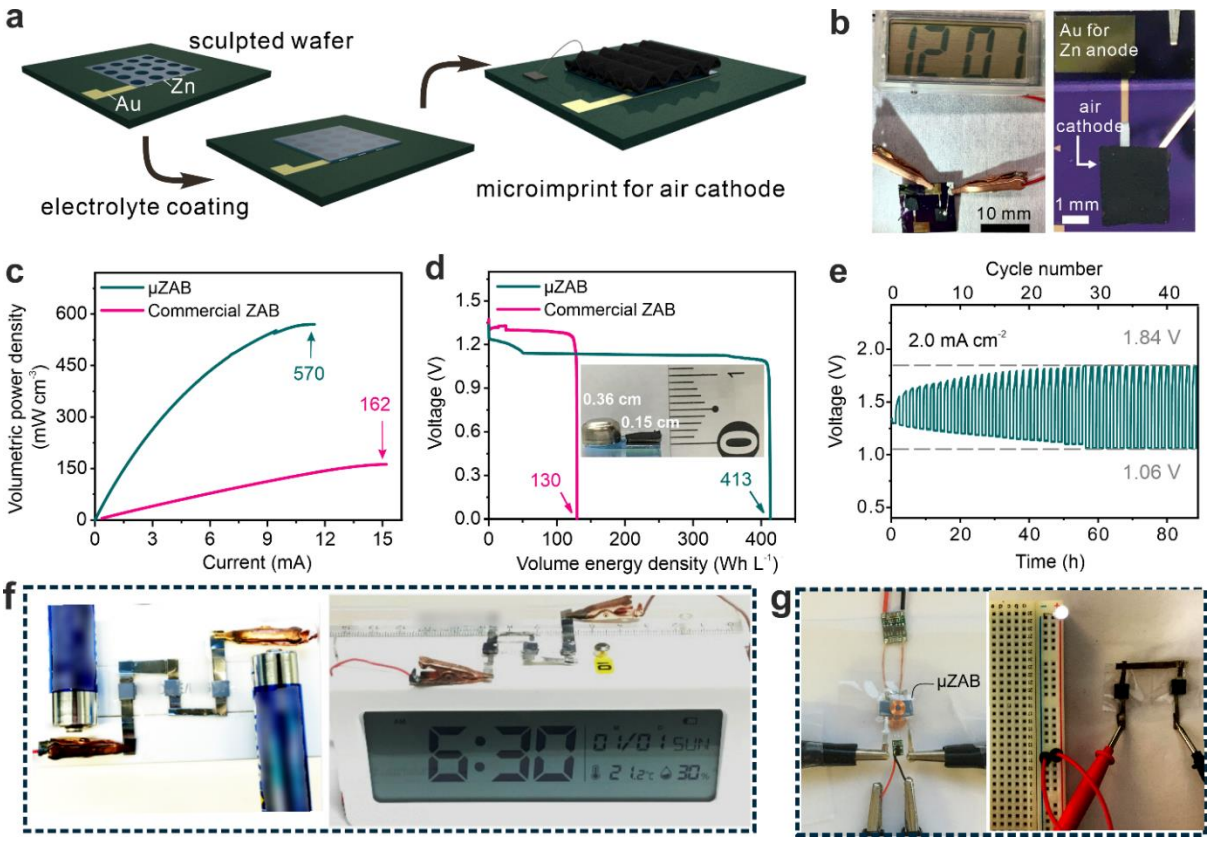

Figure 3.12. Assembly of the on-chip μZAB and its practical performance. (a) Fabrication scheme of the on-chip processing route for the μZAB. (b) Photograph of a fresh μZAB that can power the digital watch right away. (c) Volumetric power density and (d) volumetric energy density of the μZAB and the commercial one. (e) Long-term cycling performance of the μZAB. Photographs show a digital watch and humidity indicator powered driven by three tandem μZABs (f) and a LED light driven by two tandem μZABs, as well as (g) its wireless rechargeability.

The μZAB can directly drive a digital watch after on-chip manufacturing (Figure 3.12b, left panel). The as-prepared μZAB possesses a modest dimension of 3×3 mm^2 and a total thickness of 1.5 mm (Figure 3.12b, right panel). As a comparison, the commercial primary ZAB (P10 type) shows a geometry of 5.8 mm in diameter and 3.6 mm in height, 9 times larger in volume than the μZAB. Impressively, the μZAB exhibits a high OCV of 1.32 V and achieves an ultrahigh volumetric power density of 570 mW cm^{-3} (Figure 3.12c), 3.5 times greater than the commercial one (162 mW cm^{-3}).

Figure 3.12d demonstrates that the μZAB has a record-high volumetric energy density of 413 Wh L^{-1} at the device level, which is 3 times over the commercial ZAB. Notably, it also outperforms the volumetric energy density of bulk lithium-ion battery.[13] These results clearly indicate that the obtained μZAB affords superior performance than commercial ZAB in terms of volumetric power density and energy density aspects. Figure 3.12e displays the cycling stability of the μZAB at 2 mA cm^{-2}. Impressively, at a deep depth of discharge of 35% (based on Zn consumption), the μZAB withstand a long cycle life of about 90 hours with a voltage gap of 0.78 V, which is even superior to the bulk battery with a freestanding cathode (Figure 3.10f). This outstanding cycling performance and round-trip efficiency can be attributed to the 3D design of Zn anode and carvable air cathode, which results in a short electrical and electrolyte diffusion pathway. Furthermore, the μZAB delivers a lifetime capacity of 4.5 mAh, which is roughly double that of commercially available lithium-ion microbatteries.

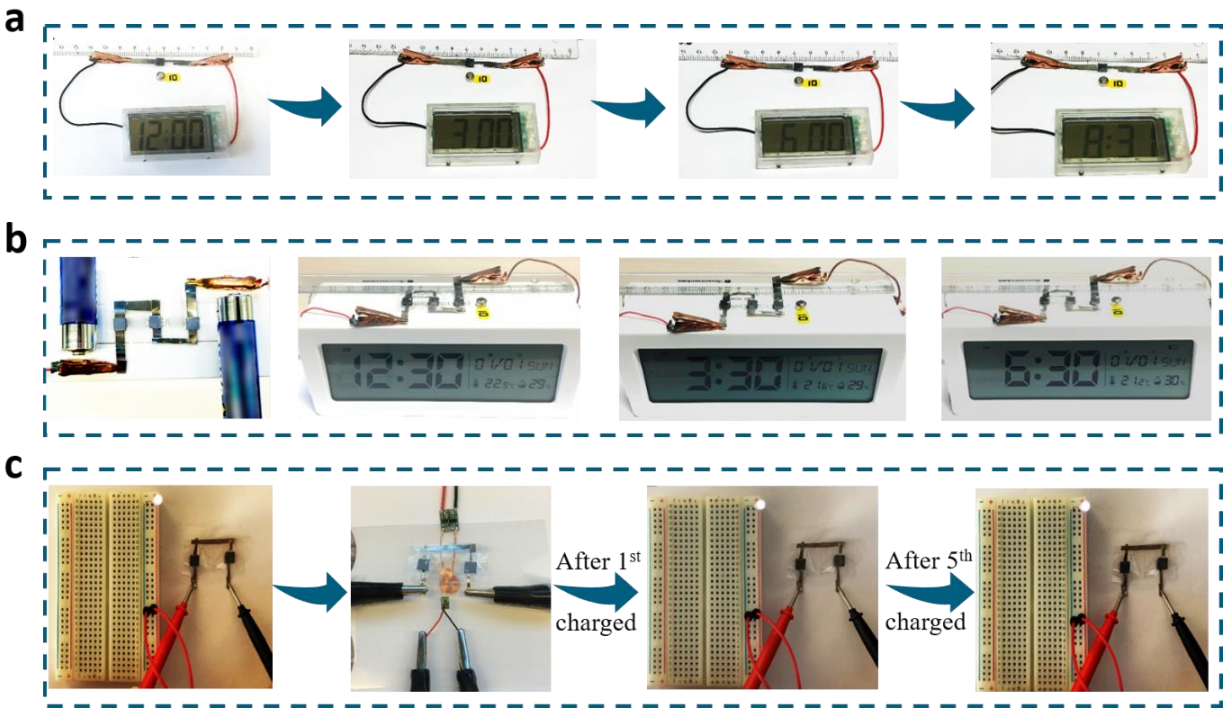

Figure 3.13. Photographs of (a) a commercial timer powered by a single μZAB for about 8.5 hours. (b) a digital watch with humidity and temperature sensors powered by three tandem μZABs, for about 6.5 hours. (c) a LED light powered by two tandem μZABs and wireless charging performance.

For practical applications, the μZAB can be employed as a reliable power source for powering complicated electronic devices. As shown in Figure 3.13a, the μZAB can power a digital timer for 8.5 hours. Furthermore, the μZABs linked in series can suit on-demand energy out requirements. As exemplified in Figure 3.12f, three tandem μZABs are able to operate a complicated digital watch and humidity indicator for 6.5 hours, equals to the operation of two bulky batteries. We also demonstrate that our μZABs are wirelessly rechrgeability. As shown in Figures 3-12g and 3.13c, a tiny coil can be simply put on two μZABs connected in series to collect the energy from the emitter, and subsequently charge the μZABs. Two tandem μZABs can light up a light-emitting diode (LED) light (50 mW) after 20 minutes of charging. The rechargeability is verified by five wireless charging and discharging cycles (Figure 3.13c).

3.4 Summary

In this work, we demonstrate an attractive design of the on-chip μZAB as a promising energy source for microsystems, where the fabrication process is compatible with microelectronic manufacturing route. Through molecular engineering techniques, we have incorporated Co catalytic units within a robust and porous COF to achieve a high-performance carvable air cathode. Such an electrode performs outstanding catalytic activity in both aqueous and quasi-solid-state ZABs. A highly adhesive hydrogel electrolyte enables the integration of the carvable air cathode with on-chip manufacturing through a microimprint technique. The obtained μZAB shows a tiny footprint area of 3×3 mm^2 and delivers an excellent energy output with an ultrahigh volumetric power density of 570 mW cm^{-3} and energy density of 413 Wh L^{-1}. Moreover, the μZAB affords a lifetime capacity of 4.5 mAh, double that of a commercially tiny lithium-ion battery. Our findings also demonstrate that the μZAB can power diverse complicated electrical devices, showing promising applications in intelligent microsystems.

Chapter 4: Quasi-solid-state Asymmetric Zn-air Batteries with High Voltage and Energy-density

4.1 Introduction

The increasing concerns about decarbonizing our energy economy have stimulated intensive interest in developing renewable and efficient energy conversion technologies.[226, 257, 258] Among them, aqueous alkaline zinc-air batteries (ZABs) with two-electron redox ($Zn^{0/2+}$) chemistry are highly appealing because of their low cost, high theoretical energy density, high safety, and relatively high abundance.[216, 259] However, the issues of CO_2 poisoning and sluggish oxygen redox reactions on air cathode hamper the large-scale implementation of ZABs.[162, 260] According to the Nernst equation, the voltage output of a ZAB is theoretically capable of 1.65 V. While the discharging voltage of conventional ZABs using solely alkaline electrolytes are in the range of 1.0 to 1.4 V Owing to the kinetic and thermodynamics limits of redox reactions.[261, 262] Consequently, the outputting energy density of ZABs reported so far is far from theoretical estimates.

To address these challenges, Yu and Manthiram et al. for the first time proposed a novel ZABs design with an asymmetric electrolyte configuration capable of preventing the neutralization of acid and alkaline electrolytes at the cathode and anode side, respectively. [157] The use of acidic catholyte eliminates the persistence issue of CO_2 poisoning on the air-electrode. Moreover, the redox potential of oxygen in an acid medium ($O_2 + 4H^+ + 4e^- \leftrightarrow 2H_2O$) increases from 0.4 to 1.23 V (vs. SHE), thus increasing the output voltage and energy density of practical devices. Although the proposed asymmetric ZAB (termed as AZAB) reached a high theoretical voltage of 2.48 V, the commercialization of the emerging AZABs still faces several challenges: (i) the lack of a cost-effective separator. Current conventional separators, such as bipolar polymer membrane (BPM) and ceramic solid-state membrane suffer from limited ion conductivity, the inevitable crossover phenomenon, and extremely expensive;[263, 264] (ii) the lack of highly active and low-cost bifunctional catalysts toward the oxygen redox reactions

in the challenging acidic electrolyte.[157, 265] Very recently, Lee et al. realized the high-voltage and long-term stable AZABs by developing a low-cost Zn^{2+}-selective polymeric separator and a highly efficient Co electrocatalyst.[266] Although this work advances the practical use of AZABs, there is still significant space for improving the overpotential of the air cathode, reducing the internal resistance of the cathode, and suppressing the dendrites formation at Zn anode in alkaline electrolytes. In addition, the rapid development in flexible and wearable devices urgently requires high-voltage-output power sources with gel polymer electrolytes. However, the creation of such AZABs remains challenging because of the lack of appropriate components for device integration.

Herein, we propose an efficient combination strategy that includes the fabrication of a low-cost separator and an efficient COF-based catalyst to realize a quasi-solid-state ZAB (sAZAB) with asymmetric gel electrolytes, having both improved discharge voltage and substantially high energy density. To do so, a low-cost Zn^{2+}-conductive polyimide separator (ZnPI) is fabricated to selectively transport Zn^{2+} ions. The Zn^{2+} ion transportation behavior stems from the abundant carbonyl groups on the polymeric backbone that serve as electron-donating sites capable of coordinating with Zn^{2+} ions. In terms of electrocatalysts, we demonstrate a CoPOF catalyst supported by layered MXene sheets (CoPOF@MXene) to efficiently catalyze oxygen redox reactions in an acidic medium. The efficient bifunctional catalytic activity can be ascribed to the synergistic impacts of Co-N_x active units and highly conductive MXene substrate.

Combining the advanced properties of the ZnPI separator and the COF-based catalyst, a high-voltage sAZAB is assembled by using a Zn anode, a CoPOF@MXene based air cathode, and a ZnPI separator sandwiched in between the alkaline anolyte (PAA-co-PVA + 6 M KOH) and the acidic catholyte (PAM-co-PVA gel + 3 M H_3PO_4). As a result, the as-fabricated sAZAB demonstrates good rate performance and stably operation for ~100 h, as well as a record open-circuit voltage (OCV) of about 2.1 V. The average round-trip efficiency achieves about 70% throughout the entire cycling process. In addition, due to the poor performance at a high discharge of depth, an optimized sAZAB with the enhanced power density and specific capacity is further constructed by combining the (002)-textured Zn electrode and $Zn_3(PO_4)_2$-based catholyte. The optimized sAZAB coin cell achieves an impressive specific

capacity of 742.4 mAh g_{Zn}^{-1} and energy density of 1425.4 Wh kg_{Zn}^{-1} at 5 mA cm^{-2}, superior than most of reported conventional quasi-solid-state ZABs. At the cell level, the optimized sAZAB in coin cell delivers an energy density of 429.7 Wh kg_{cell}^{-1}, outperforms the cell-level energy densities of commercial lithium-ion cells and other advanced batteries. This work closes the gap between fundamental research and practical applications of rechargeable ZABs, paving the way toward advances in materials science and structural engineering for electrochemical energy and storage systems.

4.2 Experimental Methods

Fabrication of ZnPI separator

ZnPI film was prepared via spin-coating and thermal imidization processes. Typically, anhydrous zinc chloride ($ZnCl_2$, 136.3 mg) and 2 mL of poly(pyromellitic dianhydride-co-4,4'-oxydianiline) (PMDA/ODA, 18 wt.%) precursor solution were added into 4 mL of 1-methyl-2-pyrrolidinone (NMP) to produce a homogenous precursor solution. The polymeric precursor was then spin-coated onto the glass and dried at 80 °C for 12 h under vacuum to remove the residual solvent. Afterward, the mixture was annealed at 360 °C for 1 h to complete the imidization process. A yellow ZnPI membrane was finally obtained after washed with de-ionized water and isopropanol.

Fabrication of the CoPOF@MXene

Firstly, 200 mg of Ti_3C_2 MXene powder was added in the mixture solution composed of 100 mL of acetic acid and 50 μL of trifluoroacetic acid, followed by ultrasonicating for 120 min. Thereafter, 18.2 μL of pyrrole, 0.90 mL of nitrobenzene, 17.4 mg of BDA, and 24.9 mg of $Co(OAc)_2$ were added to the suspension in turns. After that, the obtained mixture was transformed into a round-bottom flask and reacted for 24 h at 80 ℃ under magnetic stirring. Finally, the as-obtained product was obtained by filtrating, washing, and then vacuum-drying at 60 ℃ overnight. As a control sample, pure CoPOF was prepared in the absence of MXene powder in the system through a similar strategy to that of the CoPOF@MXene.

Synthesis of PAM-co-PVA acidic gel

Firstly, 0.675 g acrylamide was dissolved in a mixture consisting of 4 mL of H_3PO_4 (3 M) and 1 mL of PVA (5 wt.%), followed by adding 10.2 mg N, N′-methylenebis(acrylamide), and 23.84 mg ammonium persulfate. The mixed solution was under magnetic stirring to obtain a transparent solution. Afterward, the obtained solution was degassed with nitrogen for 30 min and then injected into rubber molds. The sample was kept at 70 ^oC for 3h for allowing complete polymerization. The resultant hydrogels were then taken out of the molds and stored in a 3M H_3PO_4 solution before use.

Synthesis of PAM-co-PVA acidic gel

5 mL of NaOH solution (20 M) was drop-wisely added into a mixture of acrylic acid (7.2 mL) and H_2O (10 mL) under stirring in an ice bath to obtain a transparent solution. Then, 2 mL of PVA (5 wt.%) was added in the obtained suspension with vigorous stirring, followed by adding 0.1 wt.% of N, N′-methylenebis(acrylamide) as the crosslinker and 23.84 mg of ammonium persulfate as the initiator. Thereafter, the prepared suspension was degassed with nitrogen gas for 30 min, injected into molds, and then kept at 65 ^oC for 2h to allow polymerization. Finally, the obtained hydrogels were taken out of the molds and soaked in a 6M KOH solution before use.

Material characterizations

Microstructures of as-prepared samples were characterized using a LEO Supra-35 (Carl Zeiss AG, Germany) scanning electron microscope (SEM) operated at 10 kV. The crystalline structure was examined by X-ray diffraction (XRD) using a Philips X'Pert PRO MPD diffractometer (Co Kα radiation, λ = 1.5418 A˚) and Raman spectroscopy (LabRAM HR Evolution, HORIBA Scientific) measured with a laser of 458 nm. X-ray photoelectron spectroscopy (XPS) analysis were collected using a PHI VersaProbe II (Ulvac-phi, Inc., Chigasaki, Japan) with a monochromatic Al-Kα source (photon energy of 1486.6 eV) and a power by a Thermal Scientific Al Kα XPS spectrometer of 100 W. Fourier-Transform Infrared (FTIR) spectra were measured at a resolution of 4 cm^{-1} using a Spectrum One FTIR Spectrometer (PerkinElmer, U.S.A.).

Electrochemical measurements

The interfacial resistance between the ZnPI membrane and aqueous electrolytes was evaluated by electrochemical impedance spectroscopy (EIS) technique. EIS was performed using a two-electrodes system symmetrically placed in two equivalent acetate acid or zinc acetate solutions, in which the electrolytes were separated by ZnPI. Linear sweep voltammetry (LSV) tests were conducted on the electrochemistry workstation (MULTIAUTOLAB/M101, Metrohm Autolab). The catalytic activities of as-prepared CoPOF@MXene catalysts were examined via a PINE rotating ring disk electrode (RDE) in a standard three-electrode cell. The ORR and OER activity of the catalysts was evaluated at 1600 rpm in 0.1 M O_2-saturated and N_2-saturated $HClO_4$ solution, respectively. The catalyst ink is composed of 5 mg of catalysts, 0.2 mL of H_2O, 0.8 mL of isopropanol, and 50 µL of Nafion solution (5 wt.%). The catalyst loading is controlled to be approximately 0.1 mg cm^{-2}. Notably, all of the potentials were calibrated to the potential of the reversible hydrogen electrode (RHE).

4.3 Results and Discussions

The ZnPI membrane was fabricated by a simple spin-coating method as depicted in Figure 4.1a. First, commercial PMDA/ODA solution and anhydrous $ZnCl_2$ were mixed in NMP solvent under continuous stirring to yield humongous Zn^{2+} ions coordinated PI precursor solution. The obtained precursor was then spin-coated on a glass substrate, followed by 12 hours of drying at 80 ^oC and 1 hour of curing at 360 ^oC under a vacuum to complete the thermal imidization process. Fourier-transform infrared spectroscopy (FTIR) results of pure polyamide and Zn-MEM (Figure 1b) show three strong characteristic peaks at 1776 cm^{-1} (asymmetric C=O stretching), 1716 cm^{-1} (symmetric C=O stretching) and 1370 cm^{-1} (C-N stretching), demonstrating the successful formation of imide ring.[267-269] Two peaks at ~500 and ~1500 cm^{-1} corresponding to Zn-O and nitro compound stretching occur in the ZnPI, which confirms the coordination between Zn^{2+} ions and carbonyl oxygens on the polyimide skeleton.[270] Consequently, a mechanically flexible ZnPI membrane was achieved with an average thickness of around 30 µm (Figure 4.1c). The incorporation of Zn^{2+} ions is further validated by the energy dispersive

spectroscopy (EDS) mapping of the cross-section of the ZnPI (Figure 4.1d), displaying that C, N, O, and Zn elements are distributed uniformly across the ZnPI membrane.

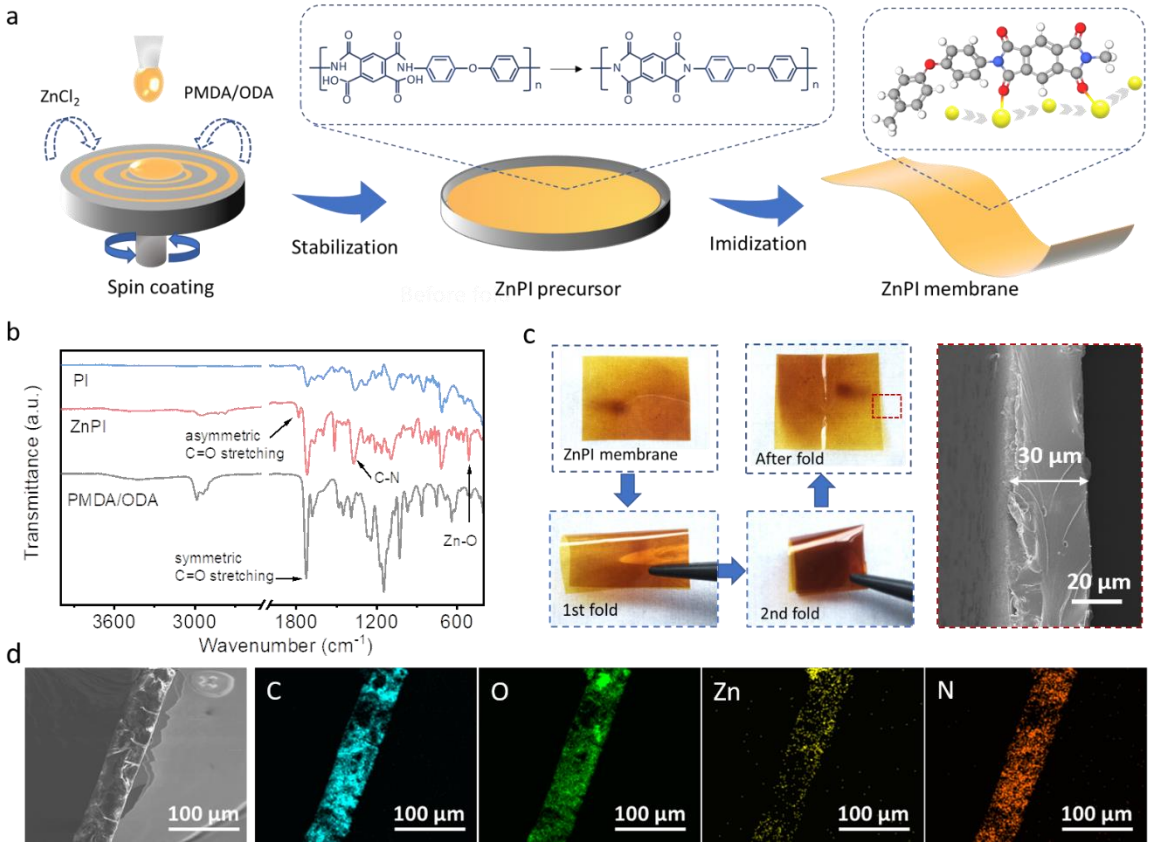

Figure 4.1. (a) Schematics of the synthesis of ZnPI membrane. (b) FTIR spectra of the ZnPI, neat PI, and commercial PMDA/ODA. (c) Optical images (left) and SEM image (right) of the ZnPI membrane, showing its mechanical flexibility. (d) Corresponding EDS mapping images of the ZnPI membrane.

In principle, Zn^{2+} ionic conductivity and Zn transference number of the ZnPI separator are critical for its practical applications in sAZABs. The ionic conductivity was first measured at temperatures ranging from 263 to 303 K by sandwiching a fresh ZnPI membrane between two Zn electrodes. As a result, the ionic conductivities of the ZnPI membrane at 263, 268, 273, 278, 283, 288, 293, 298, and 303 K are calculated to be 1.6×10^{-4}, 2.7×10^{-4}, 3.9×10^{-4}, 3.8×10^{-4}, 5.8×10^{-4}, 6.9×10^{-4}, 7.3×10^{-4}, 8.4×10^{-4}, and 1.1×10^{-3} S cm^{-1}, respectively. Figure 4-2a displays the Arrhenius plot obtained by plotting the logarithm of conductivity against the inverse temperature. The behavior of Zn^{2+} migration in the ZnPI

follows the Grotthuss hopping mechanism as the activation energy of the ZnPI was determined to be 0.13 eV.[271] In other words, the Zn^{2+} migrates throughout the ZnPI by hopping between two adjacent carbonyl groups. The Zn transference number in the ZnPI was further tested using a symmetric Zn/Zn cell at room temperature and estimated using the following Equation[272]:

$$t_{Zn^{2+}} = \frac{1}{2} \times \frac{I_{ss}(\Delta V - I_0 R_0)}{I_0(\Delta V - I_{ss} R_{ss})}$$

where ΔV stands for the applied voltage (10 mV), R_0 and R_{ss} indicates the electrode resistances before and after polarization, respectively. I_0 and I_{ss} represent the initial and steady-state currents, respectively. The Nyquist plots of the fresh and the polarized Zn/Zn symmetric cells based on the ZnPI and neat PI separators are shown in Figures 4.2b and 4.2c, respectively. The inset displays the current change under the bias of 10 mV. Fitting the Nyquist plots, as shown in Table 4.1, yields the values for these parameters. Accordingly, the zinc transference number for the ZnPI reaches 0.35, which is higher than that of the neat PI (0.22), indicating cation-controlled ion conduction.[256] The cation-controlled behavior can be attributed to the abundant carbonyl groups, which are electron-donating sites capable of coordinating with Zn^{2+} ions. Hence, the ZnPI membrane shows high selectivity of Zn^{2+} ion passage as the ionic migration resistance of H^+ is about 6 times greater than for Zn^{2+} (2910 vs. 360 Ω, Figure S2), which further reduces the risks of neutralization of the alkaline anolyte due to the shuttle of protons. As reported, the proton conductivity of the membrane relies on the proton density and surface functional groups.[271] In the ZnPI, the strong coordination of Zn^{2+} ions occupies the original sites for proton transport at the membrane/electrolyte interface, thereby increasing the proton transfer energy barrier.

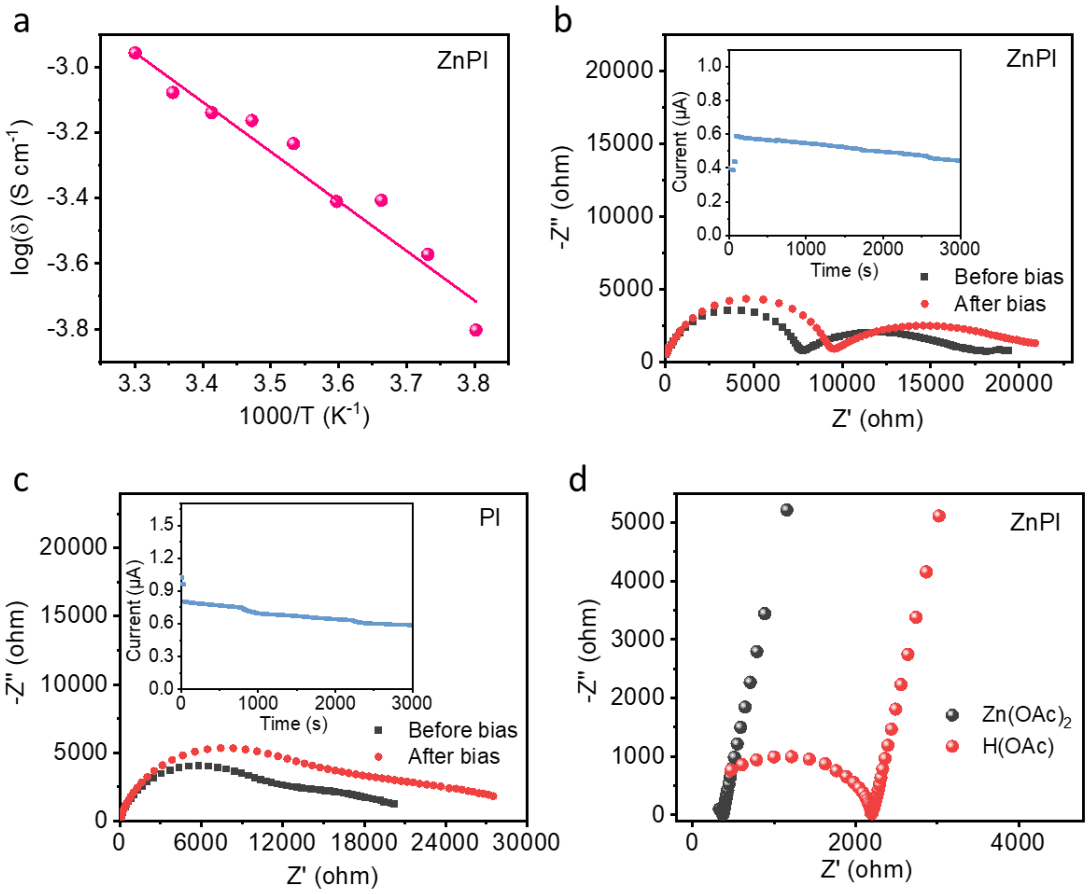

Figure 4.2. (a) Arrhenius plot of the ionic conductivity of ZnPI separator. Nyquist plots of the Zn/Zn symmetric cells based on (b) ZnPI and (c) PI separators before and after bias. The inset figures show the variation of current with time at an applied voltage of 10 mV. (d) EIS spectra of the ZnPI in 1 M H(OAc) and 1M $Zn(OAc)_2$ electrolytes.

Table 4.1. Summary of the parameters of the polar test

	R_0 (Ω)	R_{ss} (Ω)	I_0 (A)	I_{ss} (A)	$t_{Zn^{2+}}$
ZnPI	7610	9380	0.59×10^{-6}	0.44×10^{-6}	0.35
PI	11580	14750	0.79×10^{-6}	0.58×10^{-6}	0.22

Besides the solid ion conductor to prevent the neutralization of the catholyte and anolyte, it is crucial to improve the kinetics of the oxygen redox ($O_2/2O^2$) to achieve good practical performance, which generally requires an effective bifunctional catalyst with outstanding conductivity. Taking these two requirements into account, we proposed a bifunctional Co^{2+}-coordinated porphyrin-based organic framework (CoPOF) electrocatalyst with a layered two-dimensional transition metal carbides (Ti_3C_2, MXene, Figure 4.3a). The layered Ti_3C_2 MXene was fabricated by selectively etching the aluminum layers of Ti_3AlC_2 powders, showing a typical multilayer structure (Figure 4.3b). Then, the CoPOFs were in-situ grown on the layered Ti_3C_2 MXene by dehydrating pyrrole and benzene-1,4-dialdehyde and then hybridizing with Ti_3C_2 MXene. Interestingly, due to the increase of the interlayer space caused by the in-situ growth of CoPOF, layered Ti_3C_2 MXene is exfoliated into a few-layer structure with the uniform distribution of CoPOF nanospheres on the surface (Figure 4.3c). The successful formation of CoPOF nanospheres and Ti_3C_2 MXene hybrid materials (CoPOF@MXene) were confirmed by the homogeneous distribution of C, Ti, N, O, F, and Co elements. The cobalt content is measured to be about 0.16 at% according to the ICP-OES measurement.

The surface chemistry and crystalline structure of CoPOF@MXene were further investigated by FTIR and XRD analysis. Compared with pure MXene, a new peak located at 1650 cm^{-1} appears in the FTIR spectrum of the CoPOF@MXene (Figure 4.3d), stemming from the C=N stretching vibration.[210, 273] This result further confirms the formation of the CoPOF on the surface of MXene. XRD spectrum of the CoPOF@MXene (Figure 4.3e) shows the characteristic peaks of typical Ti_3C_2 MXene.[274, 275] Notably, the peak related to the (002) plane of the CoPOF@MXene downshifts to about 8.33° as compared to its original position for pure MXene (at around 8.94°). This corresponds to a 0.64 Å increase in the *d*-spacing because of the formation of CoPOF nanospheres on the interlayer of MXene. Raman spectrum of pure MXene displays four sharp peaks located at 151, 242, 446, and 616 cm^{-1} (Figure 4.3f), demonstrating the distinct features of delaminated Ti_3C_2 MXene.[274, 275] These peaks show decreased intensity after the growth of CoPOF, and two new peaks appeared at 1364 cm^{-1} (D-band) and 1580 cm^{-1} (G-band) within the CoPOF@MXene, which corresponds to the sp3 and the sp2 hybridized carbon atoms, respectively, further indicating the formation of CoPOF and its strong intermolecular

conjugated interactions with the MXene host. In such a hybrid structure, the highly conductive MXene is expected to allow for rapidly electronic transportation to access the active centers, thereby enabling fast charge transfer and promoting the catalytic activity.

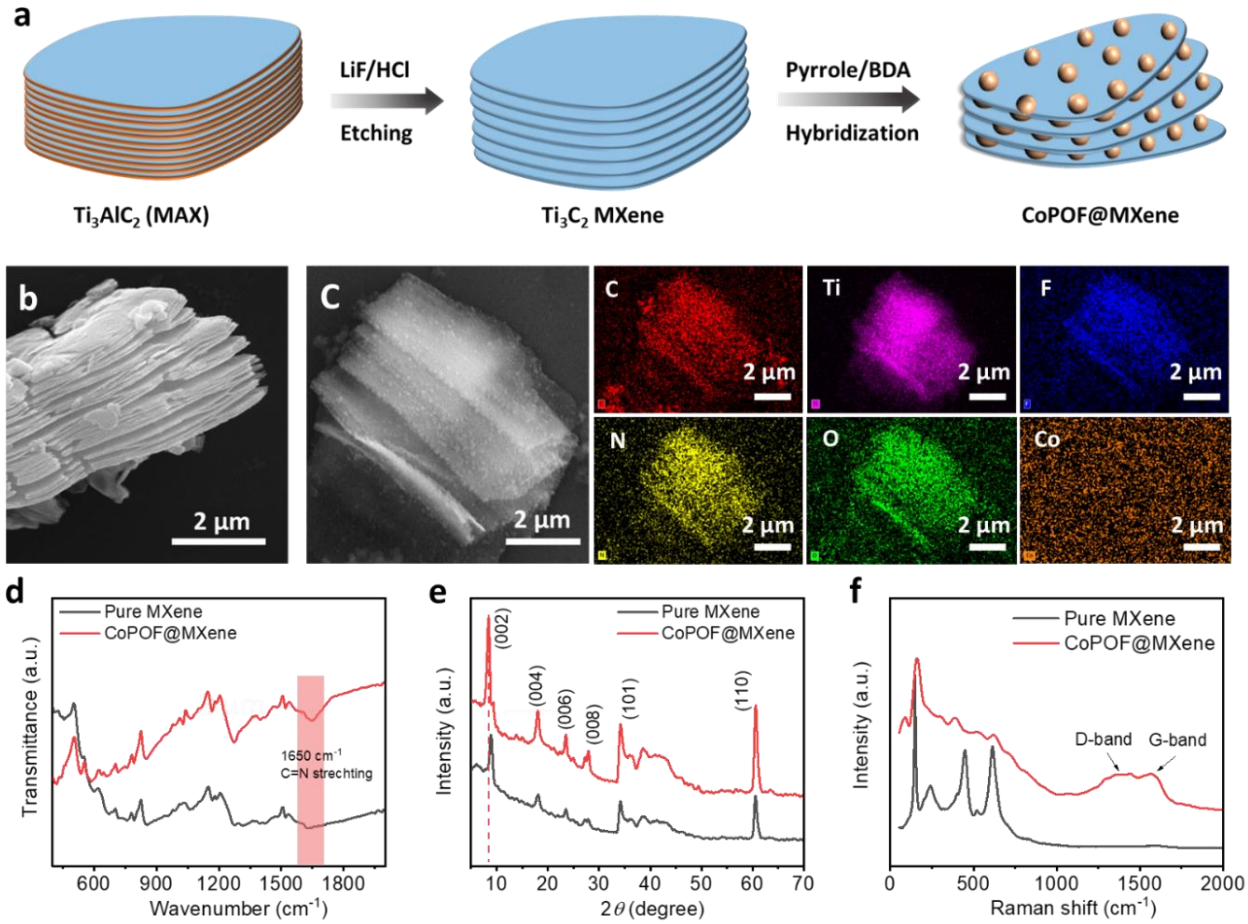

Figure 4.3. (a) Synthesis of the CoPOF@MXene catalyst. SEM images of (b) pure MXene and (c) CoPOF@MXene. The right panel in (c) is the corresponding EDS mapping images of the CoPOF@MXene. (d) FTIR, (e) XRD, and (c) Raman spectra of pure MXene and CoPOF@MXene.

Linear scan voltammetry (LSV) tests were carried out in 0.1 M $HClO_4$ solution to probe the catalytic performance of the CoPOF@MXene. As expected, the CoPOF@MXene displays much higher ORR activity over both pure CoPOF and pure MXene, suggesting the significant role of the conductive MXene host in enhancing catalytic performance. The CoPOF@MXene displays a half-wave potential of about 0.75 V (vs. RHE), close to the benchmark Pt/C catalyst (0.80 V), showing a small potential

gap of 50 mV (Figure 4.4a). Accordingly, the CoPOF@MXene catalyst displays a small Tafel slope of 85 mV dec^{-1}, slightly lower than the Pt/C (81 mV dec^{-1}, Figure 4.4b). By contrast, pure CoPOF and pure MXene demonstrate sluggish ORR kinetics displaying larger Tafel slopes of 116 and 130 mV dec^{-1}. In terms of OER activity, the CoPOF@MXene also outperforms pure CoPOF and pure MXene, achieving an overpotential of 620 mV at 10 mA cm^{-2} (Figure 4.4c) and a Tafel slope of 121 mV dec^{-1} (Figure 4.4d). To characterize the overall bifunctional catalytic performance of the CoPOF@MXene, the potential gap between the ORR half-wave potential and the OER overpotential for achieving a current density of 10 mA cm^{-2} is further calculated. The potential gap of the CoPOF@MXene is 1.05 V (Figure 4.4e), much higher tha that of pure CoPOF and pure MXene catalysts. The enhanced catalytic performance of CoPOF@MXene can be ascribed as follows, where the Co-N_x sites are responsible for catalyzing oxygen redox reactions, while the highly conductive MXene contributes to the rapid charge transfer. To investigate its performance in practical applications, quasi-solid-state ZABs were assembled by using the CoPOF@MXene based air cathode, and a PAA-co-PVA alkaline or PAM-co-PVA acidic gel electrolyte (Figure 4.5). Both in alkaline and acidic gels, the CoPOF@MXene cathodes demonstrate outstanding cycling stability for over 90 and 70 hours, respectively. These results demonstrate that the CoPOF@MXene electrocatalyst possesses great promise in serving as the air electrocatalyst for AMABs.

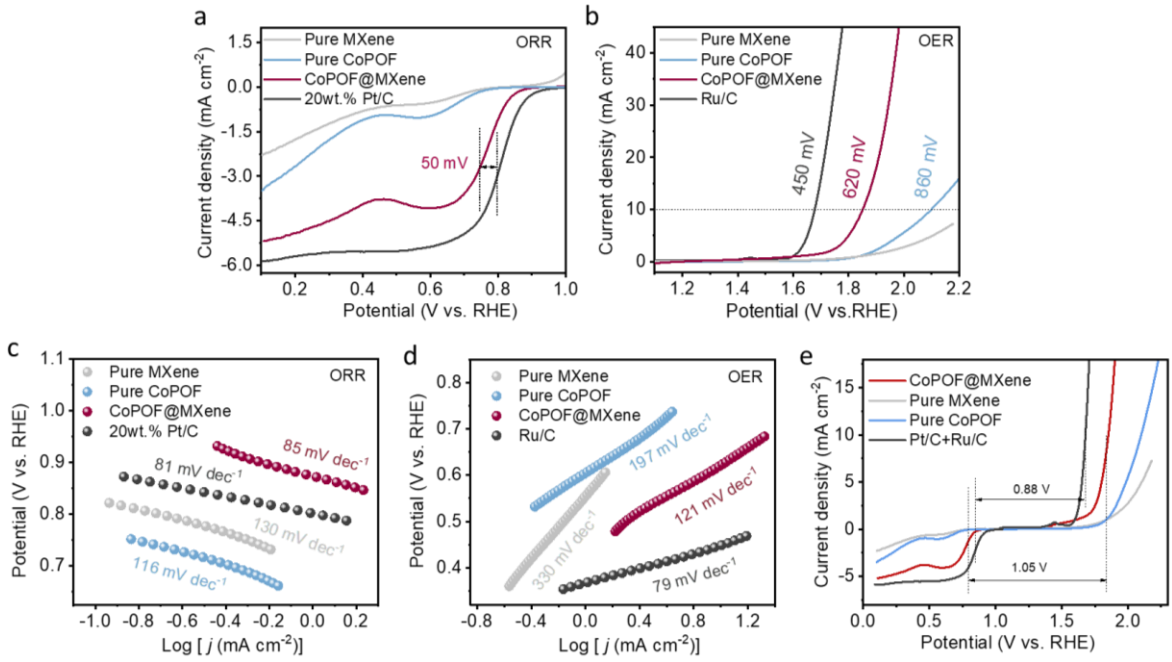

Figure 4.4. Electrochemical performance of the CoPOF@MXene. (a, b) LSV profiles and (c, d) Tafel plots of the CoPOF@MXene, the Pt/C and the Ru/C. (e) LSV curves of various catalysts for evaluating overall bifunctional performance.

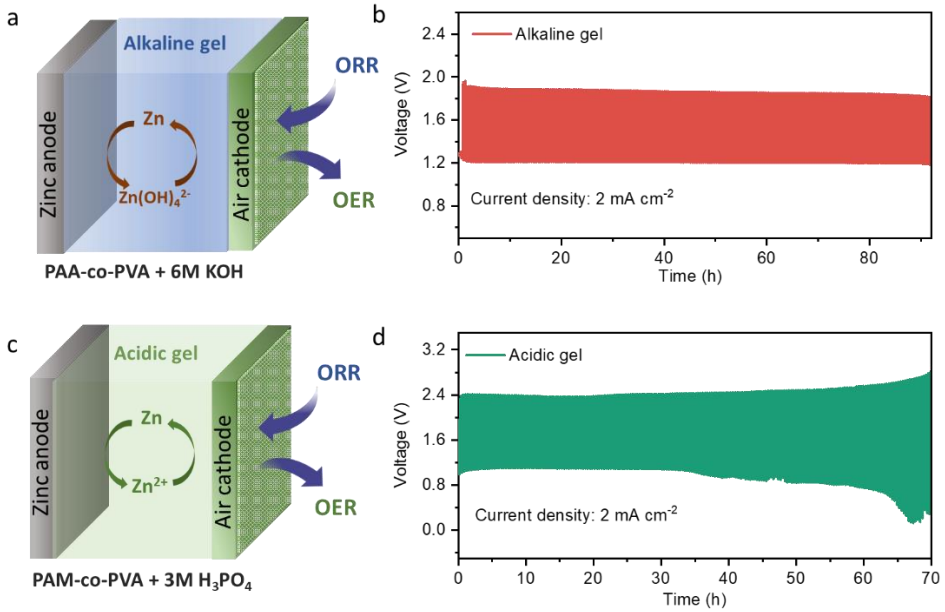

Figure 4.5. Schematic illustration of CoPOF@MXene-based ZABs assembled with (a) PAA-co-PVA-based alkaline and (c) PAM-co-PVA-based acidic gel electrolytes. (b, d) Corresponding cycling stability of the CoPOF@MXene-based ZABs.

The high-voltage sAZAB was then assembled by using a Zn anode, a ZnPI separator, and a CoPOF@MXene-based air cathode (Figure 4.6a). The ZnPI separator was placed in between the alkaline anolyte (PAA-co-PVA + 6 M KOH) and the acidic catholyte (PAM-co-PVA gel + 3 M H_3PO_4). As expected, the as-fabricated sAZAB delivered a high OCV of about 2.1 V, ~50% higher than common alkaline ZABs (e.g., ~1.4 V).[28, 217] EIS spectrum in Figure 4.6b displays a low charge transfer resistance of 20 Ω, which reveals the good interfacial interaction between gel electrolytes and the ZnPI separator. The prepared sAZAB reaches a peak power density of 140 mW cm^{-2} (Figure 4.6c), outperforms most of recently reported ZnSTM-base aqueous AZABs and is comparable with common alkaline solid-state ZABs. Additionally, the sAZAB also delivers good rate performance with stable discharge potentials at all current densities (Figure 4.6d).

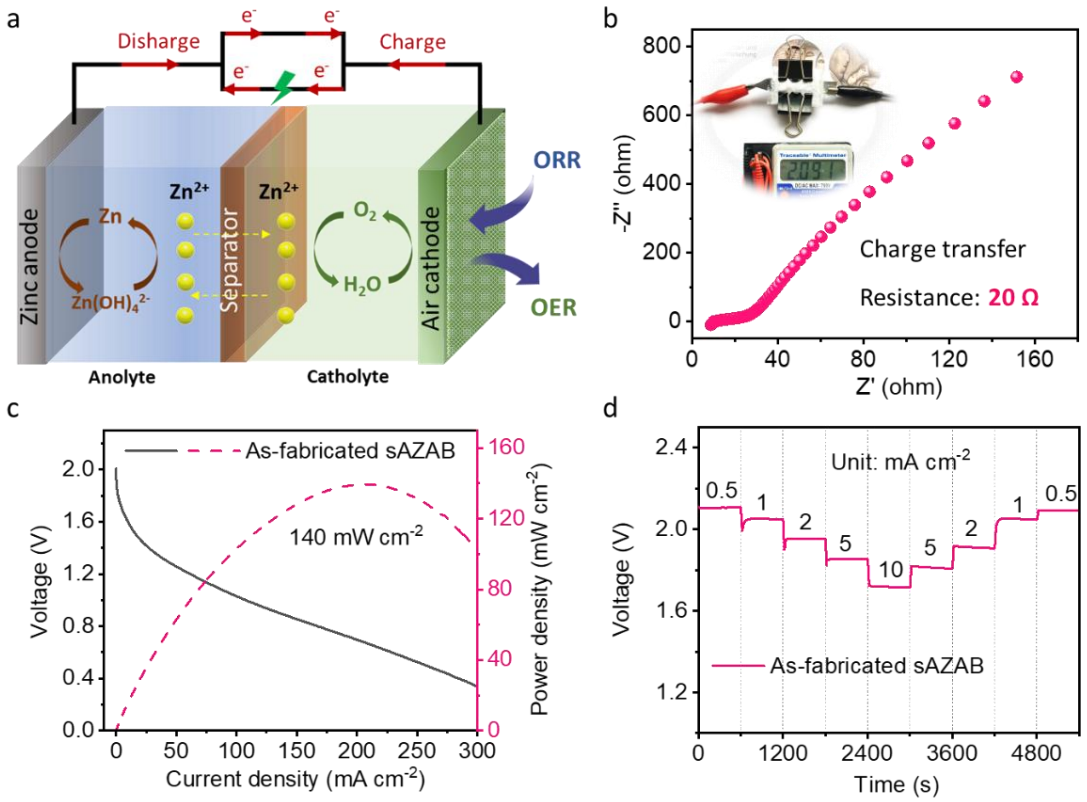

Figure 4.6. (a) Schematic illustration of the sAZAB configuration. (b) Nyquist plots, (c) discharging polarization profile, and (d) rate performance of the as-fabricated sAZAB. The inset in (b) displays the open-circuit voltage of sAZAB, approaching ~2.1 V.

The cycling performance of the sAZAB was further evaluated by the galvanostatic discharging-charging test at a current density of 0.5 mA cm^{-2} (Figure 4.7a). As a result, the sAZAB with the CoPOF@MXene operates stably for more than 90 h with an average round-trip efficiency of about 69.8%. A record round-trip efficiency of 79.2% is attained at the initial cycle and then slightly decreases to 67.3% after operation for over 90 h (Figure 4.7b). Notably, the average discharge potential is about 1.85 V, 1.3 times higher than reported conventional ZABs (i.e., ~1.4 V). This result suggests that the sAZAB configuration greatly improves the output voltage and battery performance. Based on the mass of Zn consumption, such a sAZAB can deliver specific capacities of 678, 632, and 581 mAh g_{Zn}^{-1} at 2, 5, and 10 mA cm^{-2} (Figure 4.7c), respectively.

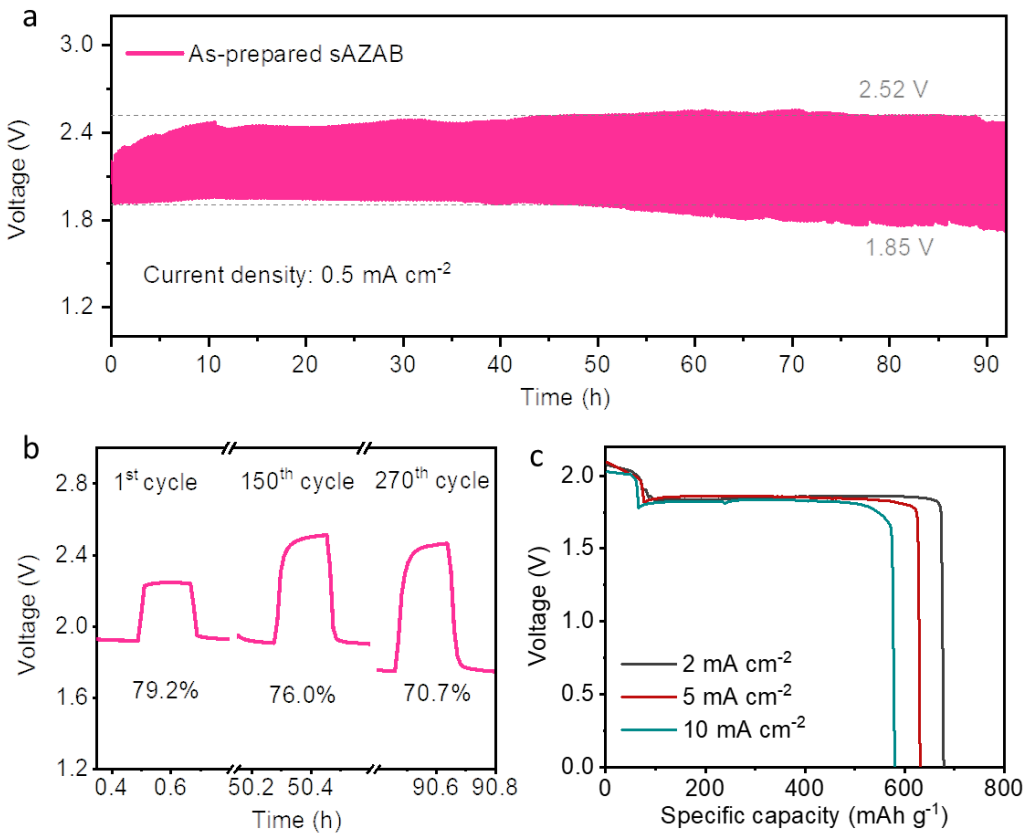

Figure 4.7. (a) Long-term cycling stability of as-prepared sAZAB at 0.5 mA cm^{-2}. (b) Corresponding round-trip efficiencies at the 1st, 150th, and 270th cycles. (c) Specific capacities of the sAZAB at different densities.

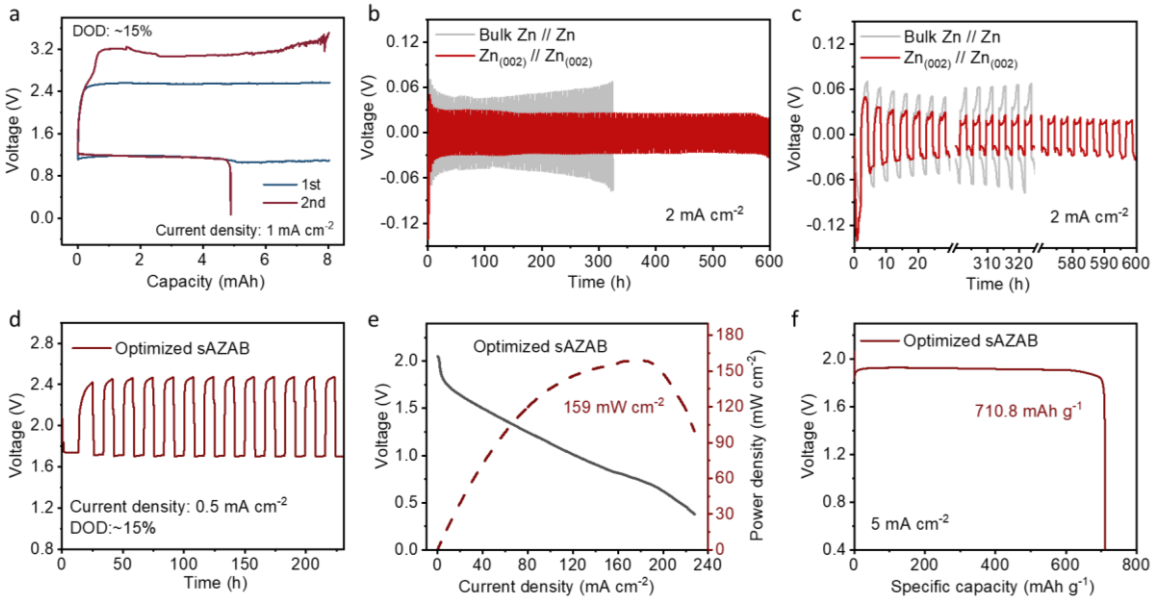

Figure 4.8. (a) Galvanostatic voltage profiles of the as-fabricated sAZAB at a high DOD of ~15%. (b, c) Galvanostatic plating/stripping profile of the textured Zn in the alkaline gel at 2 mA cm^{-2}. (d) Cycling stability of the optimized sAZAB with 16 h for per discharging-charging cycle. (e) Polarization profiles of optimized sAZAB. (f) Capacity polarization of optimized sAZAB.

It should be noted that current studies on rechargeable ZABs can't meet the requirements for practical applications as the depth of discharge (DOD) is mostly less than 1%. The battery performance at a high DOD, therefore, is of great importance and deserved to be investigated. Unfortunately, the above-mentioned excellent performance of as-fabricated sAZAB is only attainable at a low DOD of ~0.16%. When it comes to a higher DOD of 15%, the sAZAB quickly fails at the second cycle (Figure 4.8a). The reasons could be the persistent accumulation of by-products (e.g., $Zn_3(PO_4)_2$) in the catholyte and severe corrosion of Zn anode. Therefore, to prevent Zn corrosion, we use H_3PO_4 as a texturing agent to develop a (002)-textured surface for the Zn anode via (002) epitaxial growth during long-term stripping/plating cycles. As expected, the (002)-textured Zn symmetric cell stably runs for about 600 h at a current density of 2 mA cm^{-2}, while the bulk Zn foil only can be cycled for about 300 h (Figure 4.8b). A low overpotential of less than 30 mV is also attainable for the (002)-textured Zn symmetric cell (Figure 4.8c), suggesting its high Zn reversibility. At the same time, the addition of 0.5M $Zn_3(PO_4)_2$

as an additive in the catholyte has been proven for suppressing the persistent accumulation of by-products. Combining the (002)-textured Zn electrode and $Zn_3(PO_4)_2$-based catholyte, the optimized sAZAB can be stably cycled for over 200 h at a DOD of ~15% (Figure 4.8d). Additionally, the optimized sAZAB achieves a high peak power density of 159 mW cm^{-2} (Figure 4.8e) and a specific capacity of 711 mAh g_{Zn}^{-1}, which outperforms the sAZAB before optimization. These results demonstrate that the combination between (002)-textured Zn electrode and $Zn_3(PO_4)_2$-based catholyte significantly enhances the battery performance of sAZAB.

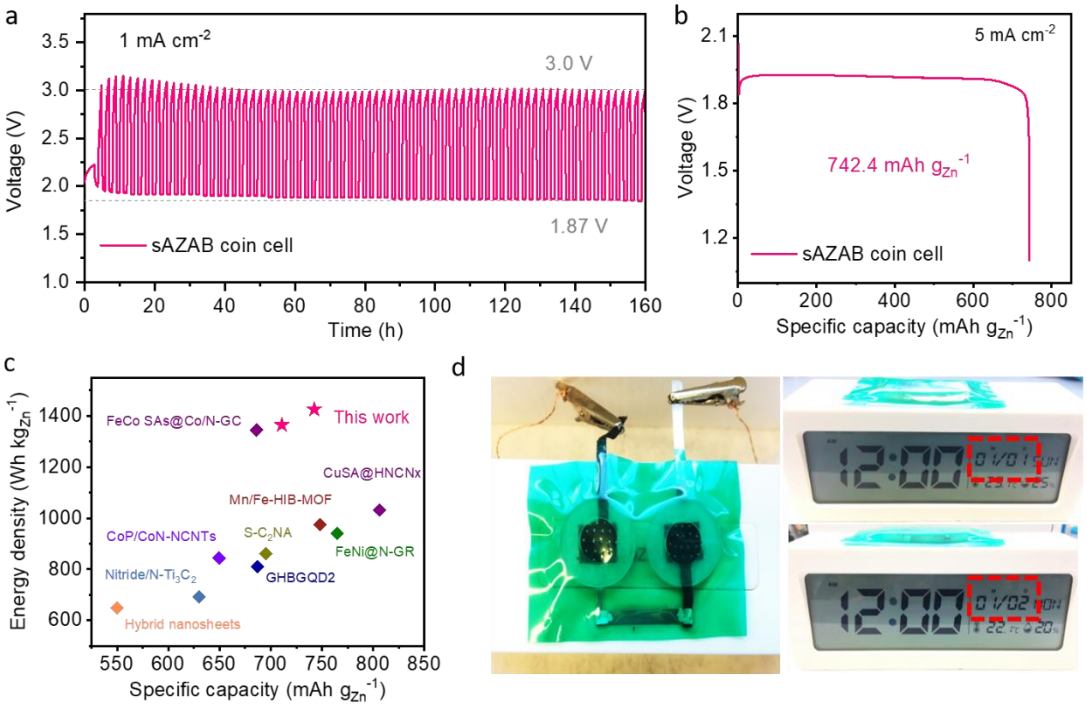

Figure 4.9. (a) Galvanostatic cycling performance of optimized sAZAB coin cell. (b) Discharge profile of the sAZAB coin cell at 5 mA cm^{-2}. (c) Ragone plots for the specific capacities and energy densities of the sAZAB and conventional quasi-solid-state ZABs previously reported (see Table 4.1 for details). (d) Two tandem sAZABs are powering a complex electronic device with a threshold voltage of 3 V.

To investigate the performance on the cell level, we further assembled the optimized sAZAB coin cell. As a result, the optimized sAZAB coin cell exhibits good stability for more than 160 h at 1 mA cm^{-2} (Figure 4.9a). Accordingly, the sAZAB coin cell achieves an impressive specific capacity of 742.4 mAh

g_{Zn}^{-1} and energy density of 1425.4 Wh kg_{Zn}^{-1} at 5 mA cm^{-2} corresponding to the mass of Zn consumption (Figure 4.9b), outperforms reported conventional quasi-solid-state ZABs (Figure 4.9c and Table 4.1).[276-284] At the cell level, a record energy density of 429.7 Wh kg_{cell}^{-1} is attainable for the sAZAB coin cell based on the overall mass weight of electrodes, ZnPI separator, and electrolytes. Notably, this value has surpassed the cell-level energy densities of commercial lithium-ion cells and other advanced batteries.[285] For practical applications, two tandem sAZAB cells can power a complicated electronic device (threshold voltage: 3 V) for 24 h in the atmosphere (Figure 4.9d).

Table 4.2. Summary of the performance of various ZABs with quasi-solid-state electrolytes.

Catalyst	Electrolyte	Power density (mW cm^{-2})	Specific capacity (mAh g_{Zn}^{-1})	Energy density (Wh kg_{Zn}^{-1})	Ref.
Mn/Fe-HIB-MOF	Functionalized bio-cellulose	193	748	975	[277]
$GHBGQD_2$	PVA gel	112	687	810	[278]
Co_2P/CoN-in-NCNTs	PVA gel	194.6	649.6	844.5	[279]
CuSA@HNCNx	Functionalized bio-cellulose	212	806	1031	[280]
Nitride/N-Ti_3C_2	PVA gel	27	630	693	[281]
S-C_2NA	Functionalized cellulose film	187	695	862	[282]
FeNi@N-GR	PVA gel	85	765	940	[283]
Hybrid nanosheets	PVA gel	45	550	649	[284]
FeCo SAs@Co/N-GC	Functionalized cellulose film	144	686	1345	[276]
CoPOF@MXene	**Asymmetric gel electrolyte**	**140** **159**	**711** **742**	**1365** **1524**	**This work**

4.4 Summary

In summary, we have developed an asymmetric AZAB capable of high voltage and energy density as a promising energy source for electronic devices. With a low-cost Zn^{2+}-conductive ZnPI separator and an efficient CoPOF@MXene catalyst, the as-fabricated sAZAB delivers long cycling stability with an average round-trip efficiency of 70% and good rate performance. At a high DOD of ~15%, the optimized sAZAB coin cell achieves a specific capacity of 742.4 mAh g_{Zn}^{-1} and energy density of 1425.4 Wh kg_{Zn}^{-1}, outperforming reported conventional quasi-solid-state ZABs. Notably, an ultrahigh energy density of 429.7 Wh kg_{cell}^{-1} is attainable, which has surpassed the cell-level energy densities of commercial lithium-ion cells. Furthermore, our sAZAB are able to drive various complicated electronic devices in practical applications, holding great promise as a powering source for energy storage and conversion.

Chapter 5: Conclusions and Future Work

5.1 Conclusions

As mentioned all along with this study, the overview of current rechargeable ZAB technology (Chapter 2), the development of advanced electrocatalyst and separator materials as well as engineering design are provided for successfully achieving a high energy density on-chip Zn-air microbattery (Chapter 3) and asymmetric-electrolyte ZABs (Chapter 4).

Firstly, in **Chapter 2**, we overview the development and fundamental principles of state-of-the-art ZAB technology, as well as scientific and technical challenges for current rechargeable ZABs. The key issues that affect the performance of ZABs are systematically discussed, such as the Zn anode, the bifunctional air cathode, the electrolyte, and the separator. In particular, the chemistry and materials of the Zn electrode and bifunctional air electrode are detailed, with special attention to the performance-limiting phenomena arising from the use of aqueous electrolyte and sluggish oxygen catalytic kinetics, Moreover, strategies to overcome these issues are summarized for developing high energy-output ZAB systems. To promote the energy density of ZABs in practical applications, specific advances in materials science and engineering are needed, such as the design of reversible Zn electrodes with high Zn utilization, efficient bifunctional electrocatalysts capable of low-cost and high durability, new electrolyte technologies, and optimal cell designs.

Miniaturizing rechargeable ZABs with high energy output for portable microelectronic devices is promising but challenging because the manufacturing technology of the battery is not compatible with on-chip processing. To address this issue, in **Chapter 3**, we propose the on-chip processing of a CoPOF-based electrocatalyst into a micro-scaled ZAB through a microimprint manufacture route. The incorporation of Co catalytic units into a stable and porous covalent organic framework allows for the simple production of a carvable air cathode with outstanding catalytic activity in both liquid and quasi-solid-state ZABs. A hydrogel electrolyte with high adhesion enables a microimprint process compatible with microelectronic manufacturing processes, to integrate the air cathode during the fabrication of on-

chip Zn-air microbattery (μZAB). As a result, the on-chip μZAB shows a record-high volumetric power density of 570 mW cm^{-3} and energy density of 413 Wh L^{-1}, approximately 3 times that of a commercial primary ZAB. The on-chip μZAB also achieves a lifecycle capacity of 4.5 mAh, which is double that of the smallest commercially available on-chip lithium-ion batteries.[234] We also show that the μZAB can run complicated electronic devices and can wirelessly recharged for prolonging the lifespan .

In **Chapter 4**, we propose a combination strategy including the preparation of a low-cost separator and an efficient COF-based catalyst to realize a quasi-solid-state asymmetric ZAB (sAZAB) with high energy output. A low-cost Zn^{2+}-conductive polyimide separator (ZnPI) is first fabricated with the aim of selectively transporting Zn^{2+} ions and increasing the energy barrier of the proton migration. In addition, a CoPOF catalyst supported by layered MXene sheets (CoPOF@MXene) is presented as the bifunctional catalyst for the sAZAB in an acidic medium. Remarkably, the as fabricated sAZAB delivers a OCV of about 2.1 V, 50% higher than that of the common alkaline ZABs (i.e., ~1.4 V). Additionally, the sAZAB also demonstrates a good rate performance and long cycling stability with an average round-trip efficiency of 70%. To improve the battery performance at a high discharge of depth, an optimized sAZAB is further constructed by combining the (002)-textured Zn electrode and adding a $Zn_3(PO_4)_2$ additive into catholyte. Impressively, the optimal sAZAB coin cell achieves a specific capacity of 742.4 mAh g_{Zn}^{-1} and an energy density of 1425.4 Wh kg_{Zn}^{-1} at 5 mA cm^{-2}, outperforming reported conventional quasi-solid-state ZABs. At the cell level, a high energy density of 429.7 Wh kg_{cell}^{-1} is attainable, which has surpassed the cell-level energy densities of commercial lithium-ion cells.

All in all, this work presents the development and design of advanced materials, as well as their integration into high-energy-output ZAB systems by combining them with engineering techniques. Our work narrows the gap between fundamental research and the practical application for rechargeable ZABs, paving the way toward advances in materials science and structural engineering for electrochemical energy and storage systems.

5.2 Future work

Although significant research progress has been made in material development and structural design, they are still not mature enough for widespread applications. According to the results of this project, several key suggestions for the ongoing work are put forward. First, more basic and in-depth research on the catalytic performance and corresponding mechanism of COF-based catalysts is of great importance to be conducted. In this regard, computational simulation and high-throughput screening can give more detailed information to explore the catalytic reaction at the molecule level. At the same time, further development of efficient oxygen electrocatalysts from earth-abundant materials is highly desirable. The properties at the electrode/electrolyte interface should be precisely regulated and optimized to expose more active centers and lower mass transfer barriers. Furthermore, for practical applications, it is very necessary to consider the compatibility between oxygen electrocatalysts and environmental conditions.

Second, for large-scale applications, the primary components of rechargeable ZABs must be greatly enhanced. The asymmetric ZAB configuration is an attractive strategy for addressing the CO_2 poisoning problem and opens up new avenue for increasing the energy output of ZABs. In this regard, the development of advanced air electrodes is crucial in such a hybrid system. To improve overall energy density of the hybrid system, great effects should be focused on novel structure designs and the optimization of electrode materials and corresponding mass loading, thereby allowing for efficient mass transportation. Furthermore, efficient and low-cost bifunctional electrocatalysts in challenging acidic media are lacking. Likewise, there is an urgent need to develop separators with high ionic conductivity and electrochemical stability to reduce dendrite proliferation as well as low-selective ion transport.

Additionally, the miniaturized ZABs for tiny wearable electronics require significant improvements in terms of energy storage performance, mechanical flexibility, and durability. Particularly, the fabrication process for microbatteries should be compatible with microelectronic manufacturing routes. Their practical energy density should be affordable for powering microsystems.

References

1. Breyer, C.; Gerlach, A., Global overview on grid-parity. *Prog. Photovolt.: Res. Appl.* **2013,** *21* (1), 121-136.
2. Munoz, L. A. H.; Huijben, J. C. C. M.; Verhees, B.; Verbong, G. P. J., The power of grid parity: A discursive approach. *Technol. Forecast. Soc. Change* **2014,** *87*, 179-190.
3. De Luna, P.; Hahn, C.; Higgins, D.; Jaffer Shaffiq, A.; Jaramillo Thomas, F.; Sargent Edward, H., What would it take for renewably powered electrosynthesis to displace petrochemical processes? *Science* **2019,** *364* (6438), eaav3506.
4. Stephens Ifan Erfyl, L.; Rossmeisl, J.; Chorkendorff, I., Toward sustainable fuel cells. *Science* **2016,** *354* (6318), 1378-1379.
5. Seh Zhi, W.; Kibsgaard, J.; Dickens Colin, F.; Chorkendorff, I.; Nørskov Jens, K.; Jaramillo Thomas, F., Combining theory and experiment in electrocatalysis: Insights into materials design. *Science* **2017,** *355* (6321), eaad4998.
6. Li, N.; Han, K.; Spratt, W.; Bedell, S.; Ren, J.; Gunawan, O.; Ott, J.; Hopstaken, M.; Cabral Jr, C.; Libsch, F.; Subramanian, C.; Shahidi, G.; Sadana, D., Dust-Sized High-Power-Density Photovoltaic Cells on Si and SOI Substrates for Wafer-Level-Packaged Small Edge Computers. *Adv. Mater.* **2020,** *32* (49), 2004573.
7. Lim, J.; Moon, E.; Barrow, M.; Nason, S. R.; Patel, P. R.; Patil, P. G.; Oh, S.; Lee, I.; Kim, H. S.; Sylvester, D.; Blaauw, D.; Chestek, C. A.; Phillips, J.; Jang, T. In *26.9 A 0.19×0.17mm2 Wireless Neural Recording IC for Motor Prediction with Near-Infrared-Based Power and Data Telemetry*, 2020 IEEE International Solid-State Circuits Conference - (ISSCC), 16-20 Feb. 2020; pp 416-418.
8. Piech, D. K.; Johnson, B. C.; Shen, K.; Ghanbari, M. M.; Li, K. Y.; Neely, R. M.; Kay, J. E.; Carmena, J. M.; Maharbiz, M. M.; Muller, R., A wireless millimetre-scale implantable neural stimulator with ultrasonically powered bidirectional communication. *Nat. Biomed. Eng.* **2020,** *4* (2), 207-222.
9. Shi, C.; Costa, T.; Elloian, J.; Zhang, Y.; Shepard, K. L., A 0.065-mm3 Monolithically-Integrated Ultrasonic Wireless Sensing Mote for Real-Time Physiological Temperature Monitoring. *IEEE Trans. Biomed. Circuits Syst.* **2020,** *14* (3), 412-424.
10. Kwak, W.-J.; Rosy; Sharon, D.; Xia, C.; Kim, H.; Johnson, L. R.; Bruce, P. G.; Nazar, L. F.; Sun, Y.-K.; Frimer, A. A.; Noked, M.; Freunberger, S. A.; Aurbach, D., Lithium–Oxygen Batteries and Related Systems: Potential, Status, and Future. *Chem. Rev.* **2020,** *120* (14), 6626-6683.
11. Bachman, J. C.; Muy, S.; Grimaud, A.; Chang, H.-H.; Pour, N.; Lux, S. F.; Paschos, O.; Maglia, F.; Lupart, S.; Lamp, P.; Giordano, L.; Shao-Horn, Y., Inorganic Solid-State Electrolytes for Lithium Batteries: Mechanisms and Properties Governing Ion Conduction. *Chem. Rev.* **2016,** *116* (1), 140-162.
12. Fan, E.; Li, L.; Wang, Z.; Lin, J.; Huang, Y.; Yao, Y.; Chen, R.; Wu, F., Sustainable Recycling Technology for Li-Ion Batteries and Beyond: Challenges and Future Prospects. *Chem. Rev.* **2020,** *120* (14), 7020-7063.
13. Tarascon, J. M.; Armand, M., Issues and challenges facing rechargeable lithium batteries. *Nature* **2001,** *414* (6861), 359-367.
14. Armand, M.; Tarascon, J. M., Building better batteries. *Nature* **2008,** *451* (7179), 652-657.
15. Aricò, A. S.; Bruce, P.; Scrosati, B.; Tarascon, J.-M.; van Schalkwijk, W., Nanostructured materials for advanced energy conversion and storage devices. *Nat. Mater.* **2005,** *4* (5), 366-377.

16. Pasta, M.; Wessells, C. D.; Huggins, R. A.; Cui, Y., A high-rate and long cycle life aqueous electrolyte battery for grid-scale energy storage. *Nat. Commun.* **2012,** *3* (1), 1149.
17. Cano, Z. P.; Banham, D.; Ye, S.; Hintennach, A.; Lu, J.; Fowler, M.; Chen, Z., Batteries and fuel cells for emerging electric vehicle markets. *Nat. Energy* **2018,** *3* (4), 279-289.
18. Lee, J.-S.; Tai Kim, S.; Cao, R.; Choi, N.-S.; Liu, M.; Lee, K. T.; Cho, J., Metal–Air Batteries with High Energy Density: Li–Air versus Zn–Air. *Adv. Energy Mater.* **2011,** *1* (1), 34-50.
19. Anju, V. G.; Manjunatha, R.; Austeria, P. M.; Sampath, S., Primary and rechargeable zinc–air batteries using ceramic and highly stable TiCN as an oxygen reduction reaction electrocatalyst. *J. Mater. Chem. A* **2016,** *4* (14), 5258-5264.
20. Du, G.; Liu, X.; Zong, Y.; Hor, T. S. A.; Yu, A.; Liu, Z., Co3O4 nanoparticle-modified MnO2 nanotube bifunctional oxygen cathode catalysts for rechargeable zinc–air batteries. *Nanoscale* **2013,** *5* (11), 4657-4661.
21. Rahman, M. A.; Wang, X.; Wen, C., High Energy Density Metal-Air Batteries: A Review. *J. Electrochem. Soc.* **2013,** *160* (10), A1759-A1771.
22. Narayanan, S. R.; Prakash, G. K. S.; Manohar, A.; Yang, B.; Malkhandi, S.; Kindler, A., Materials challenges and technical approaches for realizing inexpensive and robust iron–air batteries for large-scale energy storage. *Solid State Ionics* **2012,** *216*, 105-109.
23. Hartmann, P.; Bender, C. L.; Vračar, M.; Dürr, A. K.; Garsuch, A.; Janek, J.; Adelhelm, P., A rechargeable room-temperature sodium superoxide (NaO2) battery. *Nat. Mater.* **2013,** *12* (3), 228-232.
24. Ren, X.; Wu, Y., A Low-Overpotential Potassium–Oxygen Battery Based on Potassium Superoxide. *J. Am. Chem. Soc.* **2013,** *135* (8), 2923-2926.
25. Fu, J.; Cano, Z. P.; Park, M. G.; Yu, A.; Fowler, M.; Chen, Z., Electrically Rechargeable Zinc–Air Batteries: Progress, Challenges, and Perspectives. *Adv. Mater.* **2017,** *29* (7), 1604685.
26. Muldoon, J.; Bucur, C. B.; Gregory, T., Quest for Nonaqueous Multivalent Secondary Batteries: Magnesium and Beyond. *Chem. Rev.* **2014,** *114* (23), 11683-11720.
27. David, L.; Thomas, B. R., Handbook of batteries. McGraw-Hill Professional: 2001.
28. Zhang, H.; Qu, Z.; Tang, H.; Wang, X.; Koehler, R.; Yu, M.; Gerhard, C.; Yin, Y.; Zhu, M.; Zhang, K.; Schmidt, O. G., On-Chip Integration of a Covalent Organic Framework-Based Catalyst into a Miniaturized Zn–Air Battery with High Energy Density. *ACS Energy Lett.* **2021,** *6* (7), 2491-2498.
29. Cao, R.; Lee, J.-S.; Liu, M.; Cho, J., Recent Progress in Non-Precious Catalysts for Metal-Air Batteries. *Adv. Energy Mate.* **2012,** *2* (7), 816-829.
30. Lee, Y.; Suntivich, J.; May, K. J.; Perry, E. E.; Shao-Horn, Y., Synthesis and Activities of Rutile IrO2 and RuO2 Nanoparticles for Oxygen Evolution in Acid and Alkaline Solutions. *J. Phys. Chem. Lett.* **2012,** *3* (3), 399-404.
31. Gong, K.; Du, F.; Xia, Z.; Durstock, M.; Dai, L., Nitrogen-Doped Carbon Nanotube Arrays with High Electrocatalytic Activity for Oxygen Reduction. *Science* **2009,** *323* (5915), 760-764.
32. Miles, M. H.; Klaus, E. A.; Gunn, B. P.; Locker, J. R.; Serafin, W. E.; Srinivasan, S., The oxygen evolution reaction on platinum, iridium, ruthenium and their alloys at 80°C in acid solutions. *Electrochim. Acta* **1978,** *23* (6), 521-526.
33. Nørskov, J. K.; Rossmeisl, J.; Logadottir, A.; Lindqvist, L.; Kitchin, J. R.; Bligaard, T.; Jónsson, H., Origin of the Overpotential for Oxygen Reduction at a Fuel-Cell Cathode. *J. Phys. Chem. B* **2004,** *108* (46), 17886-17892.
34. Browne, M. P.; Sofer, Z.; Pumera, M., Layered and two dimensional metal oxides for electrochemical energy conversion. *Energy Environ. Sci.* **2019,** *12* (1), 41-58.

35. Chen, G.; Wan, H.; Ma, W.; Zhang, N.; Cao, Y.; Liu, X.; Wang, J.; Ma, R., Layered Metal Hydroxides and Their Derivatives: Controllable Synthesis, Chemical Exfoliation, and Electrocatalytic Applications. *Adv. Energy Mater.* **2020,** *10* (11), 1902535.
36. Lim, C. S.; Chua, C. K.; Sofer, Z.; Klímová, K.; Boothroyd, C.; Pumera, M., Layered transition metal oxyhydroxides as tri-functional electrocatalysts. *J. Mater. Chem. A* **2015,** *3* (22), 11920-11929.
37. Zhan, T.; Liu, X.; Lu, S.; Hou, W., Nitrogen doped NiFe layered double hydroxide/reduced graphene oxide mesoporous nanosphere as an effective bifunctional electrocatalyst for oxygen reduction and evolution reactions. *Appl. Catal. B* **2017,** *205*, 551-558.
38. Zhang, X.; Wang, Y.; Dong, S.; Li, M., Dual-site polydopamine spheres/CoFe layered double hydroxides for electrocatalytic oxygen reduction reaction. *Electrochim. Acta* **2015,** *170*, 248-255.
39. Du, Z.; Yang, P.; Wang, L.; Lu, Y.; Goodenough, J. B.; Zhang, J.; Zhang, D., Electrocatalytic performances of LaNi1−xMgxO3 perovskite oxides as bi-functional catalysts for lithium air batteries. *J. Power Sources* **2014,** *265*, 91-96.
40. Lee, D.-G.; Kim, S. H.; Joo, S. H.; Ji, H.-I.; Tavassol, H.; Jeon, Y.; Choi, S.; Lee, M.-H.; Kim, C.; Kwak, S. K.; Kim, G.; Song, H.-K., Polypyrrole-assisted oxygen electrocatalysis on perovskite oxides. *Energy Environ. Sci.* **2017,** *10* (2), 523-527.
41. Suntivich, J.; Gasteiger, H. A.; Yabuuchi, N.; Nakanishi, H.; Goodenough, J. B.; Shao-Horn, Y., Design principles for oxygen-reduction activity on perovskite oxide catalysts for fuel cells and metal–air batteries. *Nat. Chem.* **2011,** *3* (7), 546-550.
42. Zhu, H.; Zhang, P.; Dai, S., Recent Advances of Lanthanum-Based Perovskite Oxides for Catalysis. *ACS Catal.* **2015,** *5* (11), 6370-6385.
43. Zhu, Y.; Zhou, W.; Yu, J.; Chen, Y.; Liu, M.; Shao, Z., Enhancing Electrocatalytic Activity of Perovskite Oxides by Tuning Cation Deficiency for Oxygen Reduction and Evolution Reactions. *Chem. Mater.* **2016,** *28* (6), 1691-1697.
44. Chen, Z.; Duan, X.; Wei, W.; Wang, S.; Ni, B.-J., Recent advances in transition metal-based electrocatalysts for alkaline hydrogen evolution. *J. Mater. Chem. A* **2019,** *7* (25), 14971-15005.
45. Dinh, K. N.; Liang, Q.; Du, C.-F.; Zhao, J.; Tok, A. I. Y.; Mao, H.; Yan, Q., Nanostructured metallic transition metal carbides, nitrides, phosphides, and borides for energy storage and conversion. *Nano Today* **2019,** *25*, 99-121.
46. Dong, Y.; Deng, Y.; Zeng, J.; Song, H.; Liao, S., A high-performance composite ORR catalyst based on the synergy between binary transition metal nitride and nitrogen-doped reduced graphene oxide. *J. Mater. Chem. A* **2017,** *5* (12), 5829-5837.
47. Elumeeva, K.; Masa, J.; Medina, D.; Ventosa, E.; Seisel, S.; Kayran, Y. U.; Genç, A.; Bobrowski, T.; Weide, P.; Arbiol, J.; Muhler, M.; Schuhmann, W., Cobalt boride modified with N-doped carbon nanotubes as a high-performance bifunctional oxygen electrocatalyst. *J. Mater. Chem. A* **2017,** *5* (40), 21122-21129.
48. Fritz, K. E.; Yan, Y.; Suntivich, J., Influence of 3d transition-metal substitution on the oxygen reduction reaction electrocatalysis of ternary nitrides in acid. *Nano Res.* **2019,** *12* (9), 2307-2312.
49. Pan, J.; Tian, X. L.; Zaman, S.; Dong, Z.; Liu, H.; Park, H. S.; Xia, B. Y., Recent Progress on Transition Metal Oxides as Bifunctional Catalysts for Lithium-Air and Zinc-Air Batteries. *Batteries & Supercaps* **2019,** *2* (4), 336-347.
50. Wang, D.; Song, Y.; Zhang, H.; Yan, X.; Guo, J., Recent advances in transition metal borides for electrocatalytic oxygen evolution reaction. *J. Electroanal. Chem.* **2020,** *861*, 113953.
51. Wang, Y.-J.; Fan, H.; Ignaszak, A.; Zhang, L.; Shao, S.; Wilkinson, D. P.; Zhang, J., Compositing doped-carbon with metals, non-metals, metal oxides, metal nitrides and other materials to form bifunctional electrocatalysts to enhance metal-air battery oxygen reduction and evolution reactions. *Chem. Eng. J.* **2018,** *348*, 416-437.

52. Kusada, K.; Wu, D.; Yamamoto, T.; Toriyama, T.; Matsumura, S.; Xie, W.; Koyama, M.; Kawaguchi, S.; Kubota, Y.; Kitagawa, H., Emergence of high ORR activity through controlling local density-of-states by alloying immiscible Au and Ir. *Chem. Sci.* **2019,** *10* (3), 652-656.
53. Liu, M.; Zhao, Z.; Duan, X.; Huang, Y., Nanoscale Structure Design for High-Performance Pt-Based ORR Catalysts. *Adv. Mater.* **2019,** *31* (6), 1802234.
54. Tang, H.; Karnaushenko, D. D.; Neu, V.; Gabler, F.; Wang, S.; Liu, L.; Li, Y.; Wang, J.; Zhu, M.; Schmidt, O. G., Stress-Actuated Spiral Microelectrode for High-Performance Lithium-Ion Microbatteries. *Small* **2020,** *16* (35), 2002410.
55. Xiong, Y.; Xiao, L.; Yang, Y.; DiSalvo, F. J.; Abruña, H. D., High-Loading Intermetallic Pt3Co/C Core–Shell Nanoparticles as Enhanced Activity Electrocatalysts toward the Oxygen Reduction Reaction (ORR). *Chem. Mater.* **2018,** *30* (5), 1532-1539.
56. Chai, G.-L.; Qiu, K.; Qiao, M.; Titirici, M.-M.; Shang, C.; Guo, Z., Active sites engineering leads to exceptional ORR and OER bifunctionality in P,N Co-doped graphene frameworks. *Energy Environ. Sci.* **2017,** *10* (5), 1186-1195.
57. Qu, L.; Liu, Y.; Baek, J.-B.; Dai, L., Nitrogen-Doped Graphene as Efficient Metal-Free Electrocatalyst for Oxygen Reduction in Fuel Cells. *ACS Nano* **2010,** *4* (3), 1321-1326.
58. Tao, L.; Wang, Q.; Dou, S.; Ma, Z.; Huo, J.; Wang, S.; Dai, L., Edge-rich and dopant-free graphene as a highly efficient metal-free electrocatalyst for the oxygen reduction reaction. *ChemComm* **2016,** *52* (13), 2764-2767.
59. Deng, H.; Li, Q.; Liu, J.; Wang, F., Active sites for oxygen reduction reaction on nitrogen-doped carbon nanotubes derived from polyaniline. *Carbon* **2017,** *112*, 219-229.
60. Pan, T.; Liu, H.; Ren, G.; Li, Y.; Lu, X.; Zhu, Y., Metal-free porous nitrogen-doped carbon nanotubes for enhanced oxygen reduction and evolution reactions. *Sci. Bull.* **2016,** *61* (11), 889-896.
61. Yang, J.; Sun, H.; Liang, H.; Ji, H.; Song, L.; Gao, C.; Xu, H., A Highly Efficient Metal-Free Oxygen Reduction Electrocatalyst Assembled from Carbon Nanotubes and Graphene. *Adv. Mater.* **2016,** *28* (23), 4606-4613.
62. Liu, Q.; Wang, Y.; Dai, L.; Yao, J., Scalable Fabrication of Nanoporous Carbon Fiber Films as Bifunctional Catalytic Electrodes for Flexible Zn-Air Batteries. *Adv. Mater.* **2016,** *28* (15), 3000-3006.
63. Luo, H.; Jiang, W.-J.; Zhang, Y.; Niu, S.; Tang, T.; Huang, L.-B.; Chen, Y.-Y.; Wei, Z.; Hu, J.-S., Self-terminated activation for high-yield production of N,P-codoped nanoporous carbon as an efficient metal-free electrocatalyst for Zn-air battery. *Carbon* **2018,** *128*, 97-105.
64. Yuan, W.; Feng, Y.; Xie, A.; Zhang, X.; Huang, F.; Li, S.; Zhang, X.; Shen, Y., Nitrogen-doped nanoporous carbon derived from waste pomelo peel as a metal-free electrocatalyst for the oxygen reduction reaction. *Nanoscale* **2016,** *8* (16), 8704-8711.
65. Peng, P.; Zhou, Z.; Guo, J.; Xiang, Z., Well-Defined 2D Covalent Organic Polymers for Energy Electrocatalysis. *ACS Energy Lett.* **2017,** *2* (6), 1308-1314.
66. Nagai, A.; Guo, Z.; Feng, X.; Jin, S.; Chen, X.; Ding, X.; Jiang, D., Pore surface engineering in covalent organic frameworks. *Nat. Commun.* **2011,** *2* (1), 536.
67. Xiang, Z.; Cao, D., Porous covalent–organic materials: synthesis, clean energy application and design. *J. Mater. Chem. A* **2013,** *1* (8), 2691-2718.
68. Xiang, Z.; Cao, D.; Huang, L.; Shui, J.; Wang, M.; Dai, L., Nitrogen-Doped Holey Graphitic Carbon from 2D Covalent Organic Polymers for Oxygen Reduction. *Adv. Mater.* **2014,** *26* (20), 3315-3320.
69. Xiang, Z.; Xue, Y.; Cao, D.; Huang, L.; Chen, J.-F.; Dai, L., Highly Efficient Electrocatalysts for Oxygen Reduction Based on 2D Covalent Organic Polymers Complexed with Non-precious Metals. *Angew. Chem. Int. Ed.* **2014,** *53* (9), 2433-2437.

70. Bunsen, R., Ueber die anwendung der Kohle zu Volta'schen batterien. *Ann. Phys. (Berl.)* **1841,** *130* (11), 417-430.
71. Grove, W. R., LXXII. On a gaseous voltaic battery. *Lond. Edinb. Dublin philos. mag. j. sci. (Online)* **1842,** *21* (140), 417-420.
72. Grove, W. R., XXIV. On voltaic series and the combination of gases by platinum. *Lond. Edinb. Dublin philos. mag. j. sci. (Online)* **1839,** *14* (86-87), 127-130.
73. Barak, M., *Electrochemical power sources: primary and secondary batteries*. IET: 1980.
74. Gibbard, H.; Espig, H.; Hall, J.; Cretzmeyer, J.; Melrose, R. In *Mechanisms of Operation of the Zinc-Air Battery*, Proceedings of the Symposium on Battery Design and Optimization, Battery Division, Electrochemical Society: 1979; p 232.
75. Rahman, M. A.; Wang, X.; Wen, C., High energy density metal-air batteries: a review. *J. Electrochem. Soc.* **2013,** *160* (10), A1759.
76. Heise, G. W.; Schumacher, E. A., An Air-Depolarized Primary Cell with Caustic Alkali Electrolyte. *Trans. Electrochem. Soc.* **1932,** *62* (1), 383.
77. Heise, G. W., Air-depolarized primary battery. Google Patents: 1933.
78. Cook, R., Electric car showdown in Phoenix. *Popular Science* **1991,** *64*.
79. Garche, J.; Karden, E.; Moseley, P. T.; Rand, D. A., *Lead-acid batteries for future automobiles*. Elsevier: 2017.
80. Koretz, B.; Goldstein, J. R. In *Regeneration of zinc anodes for the Electric Fuel(R) zinc-air refuelable EV battery system*, IECEC-97 Proceedings of the Thirty-Second Intersociety Energy Conversion Engineering Conference (Cat. No.97CH6203), 27 July-1 Aug. 1997; pp 877-882 vol.2.
81. Ross, P. N. In *A novel zinc-air battery for electric vehicles*, Proceedings of the Tenth Annual Battery Conference on Applications and Advances, 10-13 Jan. 1995; pp 131-133.
82. Nykvist, B.; Nilsson, M., Rapidly falling costs of battery packs for electric vehicles. *Nature Clim. Change* **2015,** *5* (4), 329-332.
83. Pei, P.; Wang, K.; Ma, Z., Technologies for extending zinc–air battery's cyclelife: A review. *Applied Energy* **2014,** *128*, 315-324.
84. Lee, D. U.; Xu, P.; Cano, Z. P.; Kashkooli, A. G.; Park, M. G.; Chen, Z., Recent progress and perspectives on bi-functional oxygen electrocatalysts for advanced rechargeable metal–air batteries. *J. Mater. Chem. A* **2016,** *4* (19), 7107-7134.
85. Mainar, A. R.; Colmenares, L. C.; Blázquez, J. A.; Urdampilleta, I., A brief overview of secondary zinc anode development: The key of improving zinc-based energy storage systems. *Int. J. Energy Res.* **2018,** *42* (3), 903-918.
86. Price, S. W. T.; Thompson, S. J.; Li, X.; Gorman, S. F.; Pletcher, D.; Russell, A. E.; Walsh, F. C.; Wills, R. G. A., The fabrication of a bifunctional oxygen electrode without carbon components for alkaline secondary batteries. *J. Power Sources* **2014,** *259*, 43-49.
87. Ross, P. N.; Sokol, H., The Corrosion of Carbon Black Anodes in Alkaline Electrolyte: I . Acetylene Black and the Effect of Cobalt Catalyzation. *J. Electrochem. Soc.* **1984,** *131* (8), 1742-1750.
88. Pinto, M.; Smedley, S.; Wu, G., Recirculating anode. Google Patents: 2004.
89. Pinto, M.; Smedley, S.; Colborn, J. A., Refuelable electrochemical power source capable of being maintained in a substantially constant full condition and method of using the same. Google Patents: 2001.
90. Wolfe, D.; Friesen, C. A.; Johnson, P. B., Ionic liquid containing sulfonate ions. Google Patents: 2014.
91. Amendola, S.; Binder, M.; Black, P. J.; Sharp-Goldman, S.; Johnson, L.; Kunz, M.; Oster, M.; Chciuk, T.; Johnson, R., Electrically rechargeable, metal-air battery systems and methods. Google Patents: 2012.

92. Clark, S.; Latz, A.; Horstmann, B., A Review of Model-Based Design Tools for Metal-Air Batteries. *Batteries* **2018,** *4* (1).
93. Lide, D. R., *CRC handbook of chemistry and physics*. CRC press: 2004; Vol. 85.
94. Li, P.-C.; Chien, Y.-J.; Hu, C.-C., Novel configuration of bifunctional air electrodes for rechargeable zinc–air batteries. *J. Power Sources* **2016,** *313*, 37-45.
95. Ma, H.; Wang, B.; Fan, Y.; Hong, W., Development and Characterization of an Electrically Rechargeable Zinc-Air Battery Stack. *Energies* **2014,** *7* (10).
96. Deiss, E.; Holzer, F.; Haas, O., Modeling of an electrically rechargeable alkaline Zn–air battery. *Electrochim. Acta* **2002,** *47* (25), 3995-4010.
97. Cheng, Y.; Li, D.; Shi, L.; Xiang, Z., Efficient unitary oxygen electrode for air-based flow batteries. *Nano Energy* **2018,** *47*, 361-367.
98. Li, N.; Chen, Z.; Ren, W.; Li, F.; Cheng, H.-M., Flexible graphene-based lithium ion batteries with ultrafast charge and discharge rates. *Proc. Natl. Acad. Sci.* **2012,** *109* (43), 17360.
99. Bidault, F.; Brett, D. J. L.; Middleton, P. H.; Brandon, N. P., Review of gas diffusion cathodes for alkaline fuel cells. *J. Power Sources* **2009,** *187* (1), 39-48.
100. Gouérec, P.; Poletto, L.; Denizot, J.; Sanchez-Cortezon, E.; Miners, J. H., The evolution of the performance of alkaline fuel cells with circulating electrolyte. *J. Power Sources* **2004,** *129* (2), 193-204.
101. Gaikwad, A. M.; Whiting, G. L.; Steingart, D. A.; Arias, A. C., Highly Flexible, Printed Alkaline Batteries Based on Mesh-Embedded Electrodes. *Adv. Mater.* **2011,** *23* (29), 3251-3255.
102. Wang, X.; Lu, X.; Liu, B.; Chen, D.; Tong, Y.; Shen, G., Flexible Energy-Storage Devices: Design Consideration and Recent Progress. *Adv. Mater.* **2014,** *26* (28), 4763-4782.
103. Park, J.; Park, M.; Nam, G.; Lee, J.-s.; Cho, J., All-Solid-State Cable-Type Flexible Zinc–Air Battery. *Adv. Mater.* **2015,** *27* (8), 1396-1401.
104. Fu, J.; Lee, D. U.; Hassan, F. M.; Yang, L.; Bai, Z.; Park, M. G.; Chen, Z., Flexible High-Energy Polymer-Electrolyte-Based Rechargeable Zinc–Air Batteries. *Adv. Mater.* **2015,** *27* (37), 5617-5622.
105. Fu, J.; Zhang, J.; Song, X.; Zarrin, H.; Tian, X.; Qiao, J.; Rasen, L.; Li, K.; Chen, Z., A flexible solid-state electrolyte for wide-scale integration of rechargeable zinc–air batteries. *Energy Environ. Sci.* **2016,** *9* (2), 663-670.
106. Wang, R. Y.; Kirk, D. W.; Zhang, G. X., Effects of Deposition Conditions on the Morphology of Zinc Deposits from Alkaline Zincate Solutions. *J. Electrochem. Soc.* **2006,** *153* (5), C357.
107. Simičić, M. V.; Popov, K. I.; Krstajić, N. V., An experimental study of zinc morphology in alkaline electrolyte at low direct and pulsating overpotentials. *J. Electroanal. Chem.* **2000,** *484* (1), 18-23.
108. Despić, A. R.; Purenović, M. M., Critical Overpotential and Induction Time of Dendritic Growth. *J. Electrochem. Soc.* **1974,** *121* (3), 329.
109. Diggle, J. W.; Despic, A. R.; Bockris, J. O. M., The Mechanism of the Dendritic Electrocrystallization of Zinc. *J. Electrochem. Soc.* **1969,** *116* (11), 1503.
110. Zhang, Q.; Luan, J.; Huang, X.; Wang, Q.; Sun, D.; Tang, Y.; Ji, X.; Wang, H., Revealing the role of crystal orientation of protective layers for stable zinc anode. *Nat. Commun.* **2020,** *11* (1), 3961.
111. McLarnon, F. R.; Cairns, E. J., The Secondary Alkaline Zinc Electrode. *J. Electrochem. Soc.* **1991,** *138* (2), 645-656.
112. McBreen, J., Zinc Electrode Shape Change in Secondary Cells. *J. Electrochem. Soc.* **1972,** *119* (12), 1620.
113. Sunu, W. G.; Bennion, D. N., Transient and Failure Analyses of the Porous Zinc Electrode: I . Theoretical. *J. Electrochem. Soc.* **1980,** *127* (9), 2007-2016.

114. Einerhand, R. E. F.; Visscher, W.; de Goeij, J. J. M.; Barendrecht, E., Zinc Electrode Shape Change: I . In Situ Monitoring. *J. Electrochem. Soc.* **1991,** *138* (1), 1-7.
115. Choi, K. W.; Hamby, D.; Bennion, D. N.; Newman, J., Engineering Analysis of Shape Change in Zinc Secondary Electrodes: II . Experimental. *J. Electrochem. Soc.* **1976,** *123* (11), 1628-1637.
116. Choi, K. W.; Bennion, D. N.; Newman, J., Engineering Analysis of Shape Change in Zinc Secondary Electrodes: I . Theoretical. *J. Electrochem. Soc.* **1976,** *123* (11), 1616-1627.
117. Jung, C.-Y.; Kim, T.-H.; Kim, W.-J.; Yi, S.-C., Computational analysis of the zinc utilization in the primary zinc-air batteries. *Energy* **2016,** *102*, 694-704.
118. Gagnon, E. G.; Wang, Y. M., Pasted-Rolled Zinc Electrodes Containing Calcium Hydroxide for Use in Zn / NiOOH Cells. *J. Electrochem. Soc.* **1987,** *134* (9), 2091-2096.
119. Zhang, X. G., Fibrous zinc anodes for high power batteries. *J. Power Sources* **2006,** *163* (1), 591-597.
120. Chang, T. S.; Wang, Y. Y.; Wan, C. C., Structural effect of the zinc electrode on its discharge performance. *J. Power Sources* **1983,** *10* (2), 167-177.
121. Parker, J. F.; Chervin, C. N.; Nelson, E. S.; Rolison, D. R.; Long, J. W., Wiring zinc in three dimensions re-writes battery performance—dendrite-free cycling. *Energy Environ. Sci.* **2014,** *7* (3), 1117-1124.
122. Parker Joseph, F.; Chervin Christopher, N.; Pala Irina, R.; Machler, M.; Burz Michael, F.; Long Jeffrey, W.; Rolison Debra, R., Rechargeable nickel–3D zinc batteries: An energy-dense, safer alternative to lithium-ion. *Science* **2017,** *356* (6336), 415-418.
123. Jung, A.; Koblischka, M. R.; Lach, E.; Diebels, S.; Natter, H., Hybrid Metal Foams. *Int. J. Mater. Sci.* **2012,** *2* (4), 97-107.
124. Bouwhuis, B. A.; McCrea, J. L.; Palumbo, G.; Hibbard, G. D., Mechanical properties of hybrid nanocrystalline metal foams. *Acta Materialia* **2009,** *57* (14), 4046-4053.
125. Yan, Z.; Wang, E.; Jiang, L.; Sun, G., Superior cycling stability and high rate capability of three-dimensional Zn/Cu foam electrodes for zinc-based alkaline batteries. *RSC Advances* **2015,** *5* (102), 83781-83787.
126. Zhang, Z.; Yang, Z.; Huang, J.; Feng, Z.; Xie, X., Enhancement of electrochemical performance with Zn-Al-Bi layered hydrotalcites as anode material for Zn/Ni secondary battery. *Electrochim. Acta* **2015,** *155*, 61-68.
127. Wang, R.; Yang, Z.; Yang, B.; Fan, X.; Wang, T., A novel alcohol-thermal synthesis method of calcium zincates negative electrode materials for Ni–Zn secondary batteries. *J. Power Sources* **2014,** *246*, 313-321.
128. Huang, J.; Yang, Z.; Wang, R.; Zhang, Z.; Feng, Z.; Xie, X., Zn–Al layered double oxides as high-performance anode materials for zinc-based secondary battery. *J. Mater. Chem. A* **2015,** *3* (14), 7429-7436.
129. Liu, Z.; Cui, T.; Pulletikurthi, G.; Lahiri, A.; Carstens, T.; Olschewski, M.; Endres, F., Dendrite-Free Nanocrystalline Zinc Electrodeposition from an Ionic Liquid Containing Nickel Triflate for Rechargeable Zn-Based Batteries. *Angew. Chem. Int. Ed. Engl.* **2016,** *55* (8), 2889-2893.
130. Subbaraman, R.; Tripkovic, D.; Chang, K.-C.; Strmcnik, D.; Paulikas, A. P.; Hirunsit, P.; Chan, M.; Greeley, J.; Stamenkovic, V.; Markovic, N. M., Trends in activity for the water electrolyser reactions on 3d M(Ni,Co,Fe,Mn) hydr(oxy)oxide catalysts. *Nat. Mater.* **2012,** *11* (6), 550-557.
131. Schmid, M.; Willert-Porada, M., Zinc particles coated with bismuth oxide based glasses as anode material for zinc air batteries with improved electrical rechargeability. *Electrochim. Acta* **2018,** *260*, 246-253.
132. Zeng, D.; Yang, Z.; Wang, S.; Ni, X.; Ai, D.; Zhang, Q., Preparation and electrochemical performance of In-doped ZnO as anode material for Ni–Zn secondary cells. *Electrochim. Acta* **2011,** *56* (11), 4075-4080.

133. Bonnick, P.; Dahn, J. R., A Simple Coin Cell Design for Testing Rechargeable Zinc-Air or Alkaline Battery Systems. *J. Electrochem. Soc.* **2012,** *159* (7), A981-A989.
134. Li, H.; Xu, C.; Han, C.; Chen, Y.; Wei, C.; Li, B.; Kang, F., Enhancement on Cycle Performance of Zn Anodes by Activated Carbon Modification for Neutral Rechargeable Zinc Ion Batteries. *J. Electrochem. Soc.* **2015,** *162* (8), A1439-A1444.
135. Tao, H.; Tong, X.; Gan, L.; Zhang, S.; Zhang, X.; Liu, X., Effect of adding various carbon additives to porous zinc anode in rechargeable hybrid aqueous battery. *J. Alloys Compd.* **2016,** *658*, 119-124.
136. Ozgit, D.; Hiralal, P.; Amaratunga, G. A. J., Improving Performance and Cyclability of Zinc–Silver Oxide Batteries by Using Graphene as a Two Dimensional Conductive Additive. *ACS Appl. Mater. Interfaces* **2014,** *6* (23), 20752-20757.
137. Masri, M. N.; Mohamad, A. A., Effect of Adding Carbon Black to a Porous Zinc Anode in a Zinc-Air Battery. *J. Electrochem. Soc.* **2013,** *160* (4), A715-A721.
138. Gan, W.; Zhou, D.; Zhou, L.; Zhang, Z.; Zhao, J., Zinc electrode with anion conducting polyvinyl alcohol/poly(diallyldimethylammonium chloride) film coated ZnO for secondary zinc air batteries. *Electrochim. Acta* **2015,** *182*, 430-436.
139. Hwang, B.; Oh, E.-S.; Kim, K., Observation of electrochemical reactions at Zn electrodes in Zn-air secondary batteries. *Electrochim. Acta* **2016,** *216*, 484-489.
140. Ma, Z.; Pei, P.; Wang, K.; Wang, X.; Xu, H.; Liu, Y.; peng, G., Degradation characteristics of air cathode in zinc air fuel cells. *J. Power Sources* **2015,** *274*, 56-64.
141. Lan, C. J.; Lee, C. Y.; Chin, T. S., Tetra-alkyl ammonium hydroxides as inhibitors of Zn dendrite in Zn-based secondary batteries. *Electrochim. Acta* **2007,** *52* (17), 5407-5416.
142. Zhu, J.; Zhou, Y.; Gao, C., Influence of surfactants on electrochemical behavior of zinc electrodes in alkaline solution. *J. Power Sources* **1998,** *72* (2), 231-235.
143. Lee, C. W.; Sathiyanarayanan, K.; Eom, S. W.; Kim, H. S.; Yun, M. S., Novel electrochemical behavior of zinc anodes in zinc/air batteries in the presence of additives. *J. Power Sources* **2006,** *159* (2), 1474-1477.
144. Park, H. W.; Lee, D. U.; Zamani, P.; Seo, M. H.; Nazar, L. F.; Chen, Z., Electrospun porous nanorod perovskite oxide/nitrogen-doped graphene composite as a bi-functional catalyst for metal air batteries. *Nano Energy* **2014,** *10*, 192-200.
145. Lee, D. U.; Park, H. W.; Park, M. G.; Ismayilov, V.; Chen, Z., Synergistic Bifunctional Catalyst Design based on Perovskite Oxide Nanoparticles and Intertwined Carbon Nanotubes for Rechargeable Zinc–Air Battery Applications. *ACS Appl. Mater. Interfaces* **2015,** *7* (1), 902-910.
146. Hwang, H. J.; Chi, W. S.; Kwon, O.; Lee, J. G.; Kim, J. H.; Shul, Y.-G., Selective Ion Transporting Polymerized Ionic Liquid Membrane Separator for Enhancing Cycle Stability and Durability in Secondary Zinc–Air Battery Systems. *ACS Appl. Mater. Interfaces* **2016,** *8* (39), 26298-26308.
147. Arora, P.; Zhang, Z., Battery Separators. *Chem. Rev.* **2004,** *104* (10), 4419-4462.
148. Dewi, E. L.; Oyaizu, K.; Nishide, H.; Tsuchida, E., Cationic polysulfonium membrane as separator in zinc–air cell. *J. Power Sources* **2003,** *115* (1), 149-152.
149. Kiros, Y., Separation and permeability of zincate ions through membranes. *J. Power Sources* **1996,** *62* (1), 117-119.
150. Wu, G. M.; Lin, S. J.; You, J. H.; Yang, C. C., Study of high-anionic conducting sulfonated microporous membranes for zinc-air electrochemical cells. *Mater. Chem. Phys.* **2008,** *112* (3), 798-804.
151. Liu, X.; Fan, X.; Liu, B.; Ding, J.; Deng, Y.; Han, X.; Zhong, C.; Hu, W., Mapping the Design of Electrolyte Materials for Electrically Rechargeable Zinc–Air Batteries. *Adv. Mater.* **2021,** *33* (31), 2006461.

152. See, D. M.; White, R. E., Temperature and Concentration Dependence of the Specific Conductivity of Concentrated Solutions of Potassium Hydroxide. *J. Chem. Eng. Data* **1997,** *42* (6), 1266-1268.
153. Chakkaravarthy, C.; Waheed, A. K. A.; Udupa, H. V. K., Zinc—air alkaline batteries — A review. *J. Power Sources* **1981,** *6* (3), 203-228.
154. Thomas Goh, F. W.; Liu, Z.; Hor, T. S. A.; Zhang, J.; Ge, X.; Zong, Y.; Yu, A.; Khoo, W., A Near-Neutral Chloride Electrolyte for Electrically Rechargeable Zinc-Air Batteries. *J. Electrochem. Soc.* **2014,** *161* (14), A2080-A2086.
155. Clark, S.; Mainar, A. R.; Iruin, E.; Colmenares, L. C.; Blázquez, J. A.; Tolchard, J. R.; Latz, A.; Horstmann, B., Towards rechargeable zinc–air batteries with aqueous chloride electrolytes. *J. Mater. Chem. A* **2019,** *7* (18), 11387-11399.
156. Sun, W.; Wang, F.; Zhang, B.; Zhang, M.; Küpers, V.; Ji, X.; Theile, C.; Bieker, P.; Xu, K.; Wang, C.; Winter, M., A rechargeable zinc-air battery based on zinc peroxide chemistry. *Science* **2021,** *371* (6524), 46-51.
157. Li, L.; Manthiram, A., Long-Life, High-Voltage Acidic Zn–Air Batteries. *Adv. Energy Mater.* **2016,** *6* (5), 1502054.
158. Pozo-Gonzalo, C.; Virgilio, C.; Yan, Y.; Howlett, P. C.; Byrne, N.; MacFarlane, D. R.; Forsyth, M., Enhanced performance of phosphonium based ionic liquids towards 4 electrons oxygen reduction reaction upon addition of a weak proton source. *Electrochem. commun.* **2014,** *38*, 24-27.
159. Keist, J. S.; Orme, C. A.; Wright, P. K.; Evans, J. W., An in situ AFM Study of the Evolution of Surface Roughness for Zinc Electrodeposition within an Imidazolium Based Ionic Liquid Electrolyte. *Electrochim. Acta* **2015,** *152*, 161-171.
160. Xu, M.; Ivey, D. G.; Xie, Z.; Qu, W., Electrochemical behavior of Zn/Zn(II) couples in aprotic ionic liquids based on pyrrolidinium and imidazolium cations and bis(trifluoromethanesulfonyl)imide and dicyanamide anions. *Electrochim. Acta* **2013,** *89*, 756-762.
161. Kar, M.; Simons, T. J.; Forsyth, M.; MacFarlane, D. R., Ionic liquid electrolytes as a platform for rechargeable metal–air batteries: a perspective. *Phys. Chem. Chem. Phys.* **2014,** *16* (35), 18658-18674.
162. Mainar, A. R.; Iruin, E.; Colmenares, L. C.; Kvasha, A.; de Meatza, I.; Bengoechea, M.; Leonet, O.; Boyano, I.; Zhang, Z.; Blazquez, J. A., An overview of progress in electrolytes for secondary zinc-air batteries and other storage systems based on zinc. *J. Energy Storage* **2018,** *15*, 304-328.
163. Kim, C. S.; Oh, S. M., Performance of gel-type polymer electrolytes according to the affinity between polymer matrix and plasticizing solvent molecules. *Electrochim. Acta* **2001,** *46* (9), 1323-1331.
164. Song, Z.; Ding, J.; Liu, B.; Liu, X.; Han, X.; Deng, Y.; Hu, W.; Zhong, C., A Rechargeable Zn–Air Battery with High Energy Efficiency and Long Life Enabled by a Highly Water-Retentive Gel Electrolyte with Reaction Modifier. *Adv. Mater.* **2020,** *32* (22), 1908127.
165. Zhang, Y.; Deng, Y.-P.; Wang, J.; Jiang, Y.; Cui, G.; Shui, L.; Yu, A.; Wang, X.; Chen, Z., Recent Progress on Flexible Zn-Air Batteries. *Energy Storage Mater.* **2021,** *35*, 538-549.
166. Wu, G. M.; Lin, S. J.; Yang, C. C., Alkaline Zn-air and Al-air cells based on novel solid PVA/PAA polymer electrolyte membranes. *J. Membr. Sci.* **2006,** *280* (1), 802-808.
167. Fu, J.; Hassan, F. M.; Li, J.; Lee, D. U.; Ghannoum, A. R.; Lui, G.; Hoque, M. A.; Chen, Z., Flexible Rechargeable Zinc-Air Batteries through Morphological Emulation of Human Hair Array. *Adv. Mater.* **2016,** *28* (30), 6421-6428.
168. Lee, D. U.; Choi, J.-Y.; Feng, K.; Park, H. W.; Chen, Z., Advanced Extremely Durable 3D Bifunctional Air Electrodes for Rechargeable Zinc-Air Batteries. *Adv. Energy Mater.* **2014,** *4* (6), 1301389.

169. Li, H.; Han, C.; Huang, Y.; Huang, Y.; Zhu, M.; Pei, Z.; Xue, Q.; Wang, Z.; Liu, Z.; Tang, Z.; Wang, Y.; Kang, F.; Li, B.; Zhi, C., An extremely safe and wearable solid-state zinc ion battery based on a hierarchical structured polymer electrolyte. *Energy Environ. Sci.* **2018,** *11* (4), 941-951.
170. Lee, H.-J.; Lim, J.-M.; Kim, H.-W.; Jeong, S.-H.; Eom, S.-W.; Hong, Young T.; Lee, S.-Y., Electrospun polyetherimide nanofiber mat-reinforced, permselective polyvinyl alcohol composite separator membranes: A membrane-driven step closer toward rechargeable zinc–air batteries. *J. Membr. Sci.* **2016,** *499*, 526-537.
171. Zhou, T.; Zhang, N.; Wu, C.; Xie, Y., Surface/interface nanoengineering for rechargeable Zn–air batteries. *Energy Environ. Sci.* **2020,** *13* (4), 1132-1153.
172. Davari, E.; Johnson, A. D.; Mittal, A.; Xiong, M.; Ivey, D. G., Manganese-cobalt mixed oxide film as a bifunctional catalyst for rechargeable zinc-air batteries. *Electrochim. Acta* **2016,** *211*, 735-743.
173. Sadeghifar, H.; Djilali, N.; Bahrami, M., Effect of Polytetrafluoroethylene (PTFE) and micro porous layer (MPL) on thermal conductivity of fuel cell gas diffusion layers: Modeling and experiments. *J. Power Sources* **2014,** *248*, 632-641.
174. Suren, S.; Kheawhom, S., Development of a High Energy Density Flexible Zinc-Air Battery. *J. Electrochem. Soc.* **2016,** *163* (6), A846-A850.
175. Park, S. B.; Park, Y.-i., Fabrication of gas diffusion layer (GDL) containing microporous layer using flourinated ethylene prophylene (FEP) for proton exchange membrane fuel cell (PEMFC). *J. Precis. Eng. Manuf.* **2012,** *13* (7), 1145-1151.
176. Yan, W.-M.; Hsueh, C.-Y.; Soong, C.-Y.; Chen, F.; Cheng, C.-H.; Mei, S.-C., Effects of fabrication processes and material parameters of GDL on cell performance of PEM fuel cell. *Int. J. Hydrog. Energy* **2007,** *32* (17), 4452-4458.
177. Haas, O.; Van Wesemael, J., SECONDARY BATTERIES – METAL-AIR SYSTEMS | Zinc–Air: Electrical Recharge. In *Encyclopedia of Electrochemical Power Sources*, Garche, J., Ed. Elsevier: Amsterdam, 2009; pp 384-392.
178. Park, J.; Oh, H.; Ha, T.; Lee, Y. I.; Min, K., A review of the gas diffusion layer in proton exchange membrane fuel cells: Durability and degradation. *Applied Energy* **2015,** *155*, 866-880.
179. Hansen, H. A.; Viswanathan, V.; Nørskov, J. K., Unifying Kinetic and Thermodynamic Analysis of 2 e– and 4 e– Reduction of Oxygen on Metal Surfaces. *J. Phys. Chem. C* **2014,** *118* (13), 6706-6718.
180. Ge, X.; Sumboja, A.; Wuu, D.; An, T.; Li, B.; Goh, F. W. T.; Hor, T. S. A.; Zong, Y.; Liu, Z., Oxygen Reduction in Alkaline Media: From Mechanisms to Recent Advances of Catalysts. *ACS Catal.* **2015,** *5* (8), 4643-4667.
181. Yu, L.; Pan, X.; Cao, X.; Hu, P.; Bao, X., Oxygen reduction reaction mechanism on nitrogen-doped graphene: A density functional theory study. *J. Catal.* **2011,** *282* (1), 183-190.
182. Stamenkovic, V. R.; Strmcnik, D.; Lopes, P. P.; Markovic, N. M., Energy and fuels from electrochemical interfaces. *Nat. Mater.* **2017,** *16* (1), 57-69.
183. Suen, N.-T.; Hung, S.-F.; Quan, Q.; Zhang, N.; Xu, Y.-J.; Chen, H. M., Electrocatalysis for the oxygen evolution reaction: recent development and future perspectives. *Chem. Soc. Rev.* **2017,** *46* (2), 337-365.
184. Lu, Z.; Wang, H.; Kong, D.; Yan, K.; Hsu, P.-C.; Zheng, G.; Yao, H.; Liang, Z.; Sun, X.; Cui, Y., Electrochemical tuning of layered lithium transition metal oxides for improvement of oxygen evolution reaction. *Nat. Commun.* **2014,** *5* (1), 4345.
185. Trotochaud, L.; Young, S. L.; Ranney, J. K.; Boettcher, S. W., Nickel–Iron Oxyhydroxide Oxygen-Evolution Electrocatalysts: The Role of Intentional and Incidental Iron Incorporation. *J. Am. Chem. Soc.* **2014,** *136* (18), 6744-6753.
186. Zhang, L.; Zhao, H.; Wilkinson, D. P.; Sun, X.; Zhang, J., *Electrochemical Water Electrolysis: Fundamentals and Technologies*. CRC Press: 2020.

187. Gong, K.; Du, F.; Xia, Z.; Durstock, M.; Dai, L., Nitrogen-Doped Carbon Nanotube Arrays with High Electrocatalytic Activity for Oxygen Reduction. *Science* **2009,** *323* (5915), 760.
188. Zhang, H.; Lv, K.; Fang, B.; Forster, M. C.; Dervişoğlu, R.; Andreas, L. B.; Zhang, K.; Chen, S., Crucial role for oxygen functional groups in the oxygen reduction reaction electrocatalytic activity of nitrogen-doped carbons. *Electrochim. Acta* **2018,** *292*, 942-950.
189. Zhang, H.; Zhou, Y.; Li, C.; Chen, S.; Liu, L.; Liu, S.; Yao, H.; Hou, H., Porous nitrogen doped carbon foam with excellent resilience for self-supported oxygen reduction catalyst. *Carbon* **2015,** *95*, 388-395.
190. Liu, X.; Dai, L., Carbon-based metal-free catalysts. *Nat. Rev. Mater.* **2016,** *1* (11), 16064.
191. Zhang, J.; Zhao, Z.; Xia, Z.; Dai, L., A metal-free bifunctional electrocatalyst for oxygen reduction and oxygen evolution reactions. *Nat. Nanotech.* **2015,** *10* (5), 444-452.
192. Yang Hong, B.; Miao, J.; Hung, S.-F.; Chen, J.; Tao Hua, B.; Wang, X.; Zhang, L.; Chen, R.; Gao, J.; Chen Hao, M.; Dai, L.; Liu, B., Identification of catalytic sites for oxygen reduction and oxygen evolution in N-doped graphene materials: Development of highly efficient metal-free bifunctional electrocatalyst. *Sci. Adv. 2* (4), e1501122.
193. Shen, M.; Wei, C.; Ai, K.; Lu, L., Transition metal–nitrogen–carbon nanostructured catalysts for the oxygen reduction reaction: From mechanistic insights to structural optimization. *Nano Res.* **2017,** *10* (5), 1449-1470.
194. Fei, H.; Dong, J.; Feng, Y.; Allen, C. S.; Wan, C.; Volosskiy, B.; Li, M.; Zhao, Z.; Wang, Y.; Sun, H.; An, P.; Chen, W.; Guo, Z.; Lee, C.; Chen, D.; Shakir, I.; Liu, M.; Hu, T.; Li, Y.; Kirkland, A. I.; Duan, X.; Huang, Y., General synthesis and definitive structural identification of MN4C4 single-atom catalysts with tunable electrocatalytic activities. *Nat. Catal.* **2018,** *1* (1), 63-72.
195. Meng, F.; Zhong, H.; Yan, J.; Zhang, X., Iron-chelated hydrogel-derived bifunctional oxygen electrocatalyst for high-performance rechargeable Zn–air batteries. *Nano Res.* **2017,** *10* (12), 4436-4447.
196. Su, C.-Y.; Cheng, H.; Li, W.; Liu, Z.-Q.; Li, N.; Hou, Z.; Bai, F.-Q.; Zhang, H.-X.; Ma, T.-Y., Atomic Modulation of FeCo–Nitrogen–Carbon Bifunctional Oxygen Electrodes for Rechargeable and Flexible All-Solid-State Zinc–Air Battery. *Adv. Energy Mater.* **2017,** *7* (13), 1602420.
197. Zhang, G.; Xia, B. Y.; Xiao, C.; Yu, L.; Wang, X.; Xie, Y.; Lou, X. W., General Formation of Complex Tubular Nanostructures of Metal Oxides for the Oxygen Reduction Reaction and Lithium-Ion Batteries. *Angew. Chem. Int. Ed.* **2013,** *52* (33), 8643-8647.
198. Osgood, H.; Devaguptapu, S. V.; Xu, H.; Cho, J.; Wu, G., Transition metal (Fe, Co, Ni, and Mn) oxides for oxygen reduction and evolution bifunctional catalysts in alkaline media. *Nano Today* **2016,** *11* (5), 601-625.
199. Liang, Y.; Li, Y.; Wang, H.; Zhou, J.; Wang, J.; Regier, T.; Dai, H., Co3O4 nanocrystals on graphene as a synergistic catalyst for oxygen reduction reaction. *Nat. Mater.* **2011,** *10* (10), 780-786.
200. Chen, Z.; Yu, A.; Higgins, D.; Li, H.; Wang, H.; Chen, Z., Highly Active and Durable Core–Corona Structured Bifunctional Catalyst for Rechargeable Metal–Air Battery Application. *Nano Letters* **2012,** *12* (4), 1946-1952.
201. Malkhandi, S.; Yang, B.; Manohar, A. K.; Manivannan, A.; Prakash, G. K. S.; Narayanan, S. R., Electrocatalytic Properties of Nanocrystalline Calcium-Doped Lanthanum Cobalt Oxide for Bifunctional Oxygen Electrodes. *J. Phys. Chem. Lett.* **2012,** *3* (8), 967-972.
202. Jung, J.-I.; Risch, M.; Park, S.; Kim, M. G.; Nam, G.; Jeong, H.-Y.; Shao-Horn, Y.; Cho, J., Optimizing nanoparticle perovskite for bifunctional oxygen electrocatalysis. *Energy Environ. Sci.* **2016,** *9* (1), 176-183.
203. Park, J.; Risch, M.; Nam, G.; Park, M.; Shin, T. J.; Park, S.; Kim, M. G.; Shao-Horn, Y.; Cho, J., Single crystalline pyrochlore nanoparticles with metallic conduction as efficient bi-functional oxygen electrocatalysts for Zn–air batteries. *Energy Environ. Sci.* **2017,** *10* (1), 129-136.

204. Zhang, H.; Zhu, M.; Schmidt, O. G.; Chen, S.; Zhang, K., Covalent Organic Frameworks for Efficient Energy Electrocatalysis: Rational Design and Progress. *Adv. Energy Sustainability Res.* **2021,** *2* (4), 2000090.
205. Lin, X.; Peng, P.; Guo, J.; Xiang, Z., Reaction milling for scalable synthesis of N, P-codoped covalent organic polymers for metal-free bifunctional electrocatalysts. *Chem. Eng. J.* **2019,** *358*, 427-434.
206. Xu, Q.; Tang, Y.; Zhang, X.; Oshima, Y.; Chen, Q.; Jiang, D., Template Conversion of Covalent Organic Frameworks into 2D Conducting Nanocarbons for Catalyzing Oxygen Reduction Reaction. *Adv. Mater.* **2018,** *30* (15), 1706330.
207. Li, B.-Q.; Zhang, S.-Y.; Chen, X.; Chen, C.-Y.; Xia, Z.-J.; Zhang, Q., One-Pot Synthesis of Framework Porphyrin Materials and Their Applications in Bifunctional Oxygen Electrocatalysis. *Adv. Funct. Mater.* **2019,** *29* (29), 1901301.
208. Singh, A.; Roy, S.; Das, C.; Samanta, D.; Maji, T. K., Metallophthalocyanine-based redox active metal–organic conjugated microporous polymers for OER catalysis. *ChemComm* **2018,** *54* (35), 4465-4468.
209. Wu, D.; Xu, Q.; Qian, J.; Li, X.; Sun, Y., Bimetallic Covalent Organic Frameworks for Constructing Multifunctional Electrocatalyst. *Chem. Eur. J.* **2019,** *25* (12), 3105-3111.
210. Li, B.-Q.; Zhao, C.-X.; Chen, S.; Liu, J.-N.; Chen, X.; Song, L.; Zhang, Q., Framework-Porphyrin-Derived Single-Atom Bifunctional Oxygen Electrocatalysts and their Applications in Zn-Air Batteries. *Adv. Mater.* **2019,** *31* (19), 1900592.
211. Oh, S.; Blaauw, D.; Sylvester, D., The Internet of Tiny Things: Recent Advances of Millimeter-Scale Computing. *IEEE Design & Test* **2019,** *36* (2), 65-72.
212. Oh, S.; Cho, M.; Wu, X.; Kim, Y.; Chuo, L.; Lim, W.; Pannuto, P.; Bang, S.; Yang, K.; Kim, H.; Sylvester, D.; Blaauw, D. In *IoT^2-the Internet of Tiny Things: Realizing mm-Scale Sensors through 3D Die Stacking*, 2019 Design, Automation & Test in Europe Conference & Exhibition (DATE), 25-29 March 2019; pp 686-691.
213. Wu, X.; Lee, I.; Dong, Q.; Yang, K.; Kim, D.; Wang, J.; Peng, Y.; Zhang, Y.; Saligane, M.; Yasuda, M.; Kumeno, K.; Ohno, F.; Miyoshi, S.; Kawaminami, M.; Sylvester, D.; Blaauw, D. In *A 0.04mm^3 16nW Wireless and Batteryless Sensor System with Integrated Cortex-M0+ Processor and Optical Communication for Cellular Temperature Measurement*, 2018 IEEE Symposium on VLSI Circuits, 18-22 June 2018; pp 191-192.
214. Zhu, M.; Schmidt, O. G., Tiny robots and sensors need tiny batteries-here's how to do it. *Nature* **2021,** *589*, 195-197.
215. Li, Y.; Dai, H., Recent advances in zinc-air batteries. *Chem. Soc. Rev.* **2014,** *43* (15), 5257-5275.
216. Li, Y.; Lu, J., Metal–air batteries: Will they be the future electrochemical energy storage device of choice? *ACS Energy Lett.* **2017,** *2* (6), 1370-1377.
217. Wang, H.-F.; Tang, C.; Zhang, Q., A Review of Precious-Metal-Free Bifunctional Oxygen Electrocatalysts: Rational Design and Applications in Zn-Air Batteries. *Adv. Funct. Mater.* **2018,** *28* (46), 1803329.
218. Pan, J.; Xu, Y. Y.; Yang, H.; Dong, Z.; Liu, H.; Xia, B. Y., Advanced architectures and relatives of air electrodes in Zn–air batteries. *Adv. Sci.* **2018,** *5* (4), 1700691.
219. Chamran, F.; Yeh, Y.; Min, H.; Dunn, B.; Kim, C., Fabrication of high-aspect-ratio electrode arrays for three-dimensional microbatteries. *J. Microelectromech. Syst.* **2007,** *16* (4), 844-852.
220. Hong-Seok Min; Fardad Chamran; Yuting Yeh; Chang-Jin Kim; Dunn, a. B., The development of microbatteries based on three-dimensional architectures. *ECS Meeting Abstracts* **2006**.

221. Armutlulu, A.; Fang, Y.; Kim, S. H.; Ji, C. H.; Bidstrup Allen, S. A.; Allen, M. G., A MEMS-enabled 3D zinc–air microbattery with improved discharge characteristics based on a multilayer metallic substructure. *J. Micromech. Microeng.* **2011,** *21* (10), 104011.
222. Edström, K.; Brandell, D.; Gustafsson, T.; Nyholm, L., Electrodeposition as a tool for 3D microbattery fabrication. *Electrochem. Soc. Interface* **2011,** *20* (2), 41.
223. Fu, L.; Luo, J. K.; Huber, J. E.; Lu, T. J., Design and fabrication of a micro zinc/air battery. *J. Phys. Conf. Ser.* **2006,** *34*, 800-805.
224. Pei, Z.; Li, H.; Huang, Y.; Xue, Q.; Huang, Y.; Zhu, M.; Wang, Z.; Zhi, C., Texturing in situ: N,S-enriched hierarchically porous carbon as a highly active reversible oxygen electrocatalyst. *Energy Environ. Sci.* **2017,** *10* (3), 742-749.
225. Pei, Z.; Yuan, Z.; Wang, C.; Zhao, S.; Fei, J.; Wei, L.; Chen, J.; Wang, C.; Qi, R.; Liu, Z., A Flexible Rechargeable Zinc–Air Battery with Excellent Low-Temperature Adaptability. *Angew. Chem. Int. Ed.* **2020,** *132* (12), 4823-4829.
226. Wang, H.-F.; Xu, Q., Materials design for rechargeable metal-air batteries. *Matter* **2019,** *1* (3), 565-595.
227. Liu, D.; Dai, L.; Lin, X.; Chen, J.-F.; Zhang, J.; Feng, X.; Müllen, K.; Zhu, X.; Dai, S., Chemical approaches to carbon-based metal-free catalysts. *Adv. Mater.* **2019,** *31* (13), 1804863.
228. Côté, A. P.; Benin, A. I.; Ockwig, N. W.; Keeffe, M.; Matzger, A. J.; Yaghi, O. M., Porous, Crystalline, Covalent Organic Frameworks. *Science* **2005,** *310* (5751), 1166.
229. Waller, P. J.; Gándara, F.; Yaghi, O. M., Chemistry of covalent organic frameworks. *Acc. Chem. Res.* **2015,** *48* (12), 3053-3063.
230. Cui, X.; Lei, S.; Wang, A. C.; Gao, L.; Zhang, Q.; Yang, Y.; Lin, Z., Emerging covalent organic frameworks tailored materials for electrocatalysis. *Nano Energy* **2020,** *70*, 104525.
231. Lin, C.-Y.; Zhang, D.; Zhao, Z.; Xia, Z., Covalent Organic Framework Electrocatalysts for Clean Energy Conversion. *Adv. Mater.* **2018,** *30* (5), 1703646.
232. Zhao, X.; Pachfule, P.; Li, S.; Langenhahn, T.; Ye, M.; Schlesiger, C.; Praetz, S.; Schmidt, J.; Thomas, A., Macro/Microporous Covalent Organic Frameworks for Efficient Electrocatalysis. *J. Am. Chem. Soc.* **2019,** *141* (16), 6623-6630.
233. Li, B.-Q.; Zhang, S.-Y.; Wang, B.; Xia, Z.-J.; Tang, C.; Zhang, Q., A porphyrin covalent organic framework cathode for flexible Zn–air batteries. *Energy Environ. Sci.* **2018,** *11* (7), 1723-1729.
234. Wang, Y.; Liu, B.; Li, Q.; Cartmell, S.; Ferrara, S.; Deng, Z. D.; Xiao, J., Lithium and lithium ion batteries for applications in microelectronic devices: A review. *J. Power Sources* **2015,** *286*, 330-345.
235. Kuang, M.; Tao Li, T.; Chen, H.; Mao Zhang, S.; Li Zhang, L.; Xin Zhang, Y., Hierarchical Cu2O/CuO/Co3O4 core-shell nanowires: synthesis and electrochemical properties. *Nanotechnology* **2015,** *26* (30), 304002.
236. Yang, Q.; Wang, D.; Wang, C.; Li, X.; Li, K.; Peng, Y.; Li, J., Facile surface improvement method for LaCoO3 for toluene oxidation. *Catal. Sci. Technol.* **2018,** *8* (12), 3166-3173.
237. Lin, S.; Diercks, C. S.; Zhang, Y.-B.; Kornienko, N.; Nichols, E. M.; Zhao, Y.; Paris, A. R.; Kim, D.; Yang, P.; Yaghi, O. M.; Chang, C. J., Covalent organic frameworks comprising cobalt porphyrins for catalytic CO_2 reduction in water. *Science* **2015,** *349* (6253), 1208.
238. Zhao, D.; Zhuang, Z.; Cao, X.; Zhang, C.; Peng, Q.; Chen, C.; Li, Y., Atomic site electrocatalysts for water splitting, oxygen reduction and selective oxidation. *Chem. Soc. Rev.* **2020,** *49* (7), 2215-2264.
239. Zheng, Y.; Jiao, Y.; Zhu, Y.; Cai, Q.; Vasileff, A.; Li, L. H.; Han, Y.; Chen, Y.; Qiao, S.-Z., Molecule-level g-C3N4 coordinated transition metals as a new class of electrocatalysts for oxygen electrode reactions. *J. Am. Chem. Soc.* **2017,** *139* (9), 3336-3339.

240. Wu, J.-B.; Zhang, X.; Ijäs, M.; Han, W.-P.; Qiao, X.-F.; Li, X.-L.; Jiang, D.-S.; Ferrari, A. C.; Tan, P.-H., Resonant Raman spectroscopy of twisted multilayer graphene. *Nat. Commun.* **2014,** *5* (1), 5309.
241. Dresselhaus, M. S.; Dresselhaus, G.; Saito, R.; Jorio, A., Raman spectroscopy of carbon nanotubes. *Phys. Rep.* **2005,** *409* (2), 47-99.
242. Qiu, K.; Chai, G.; Jiang, C.; Ling, M.; Tang, J.; Guo, Z., Highly Efficient Oxygen Reduction Catalysts by Rational Synthesis of Nanoconfined Maghemite in a Nitrogen-Doped Graphene Framework. *ACS Catal.* **2016,** *6* (6), 3558-3568.
243. Wang, Y.; Yang, Y.; Jia, S.; Wang, X.; Lyu, K.; Peng, Y.; Zheng, H.; Wei, X.; Ren, H.; Xiao, L.; Wang, J.; Muller, D. A.; Abruña, H. D.; Hwang, B. J.; Lu, J.; Zhuang, L., Synergistic Mn-Co catalyst outperforms Pt on high-rate oxygen reduction for alkaline polymer electrolyte fuel cells. *Nat. Commun.* **2019,** *10* (1), 1506.
244. Zhao, Y.; Wan, J.; Yao, H.; Zhang, L.; Lin, K.; Wang, L.; Yang, N.; Liu, D.; Song, L.; Zhu, J.; Gu, L.; Liu, L.; Zhao, H.; Li, Y.; Wang, D., Few-layer graphdiyne doped with sp-hybridized nitrogen atoms at acetylenic sites for oxygen reduction electrocatalysis. *Nat. Chem.* **2018,** *10* (9), 924-931.
245. Ma, L.; Chen, S.; Wang, D.; Yang, Q.; Mo, F.; Liang, G.; Li, N.; Zhang, H.; Zapien, J. A.; Zhi, C., Super-Stretchable Zinc–Air Batteries Based on an Alkaline-Tolerant Dual-Network Hydrogel Electrolyte. *Adv. Energy Mater.* **2019,** *9* (12), 1803046.
246. Rabat, N. E.; Hashim, S.; Majid, R. A., Effect of Different Monomers on Water Retention Properties of Slow Release Fertilizer Hydrogel. *Procedia Eng.* **2016,** *148*, 201-207.
247. Liu, S.; Wang, M.; Sun, X.; Xu, N.; Liu, J.; Wang, Y.; Qian, T.; Yan, C., Facilitated oxygen chemisorption in heteroatom-doped carbon for improved oxygen reaction activity in all-solid-state zinc–air batteries. *Adv. Mater.* **2018,** *30* (4), 1704898.
248. Wang, X.; Liao, Z.; Fu, Y.; Neumann, C.; Turchanin, A.; Nam, G.; Zschech, E.; Cho, J.; Zhang, J.; Feng, X., Confined growth of porous nitrogen-doped cobalt oxide nanoarrays as bifunctional oxygen electrocatalysts for rechargeable zinc–air batteries. *Energy Stor. Mater.* **2020,** *26*, 157-164.
249. Guan, C.; Sumboja, A.; Wu, H.; Ren, W.; Liu, X.; Zhang, H.; Liu, Z.; Cheng, C.; Pennycook, S. J.; Wang, J., Hollow Co3O4 nanosphere embedded in carbon arrays for stable and flexible solid-state zinc–air batteries. *Adv. Mater.* **2017,** *29* (44), 1704117.
250. Ji, D.; Fan, L.; Li, L.; Mao, N.; Qin, X.; Peng, S.; Ramakrishna, S., Hierarchical catalytic electrodes of cobalt-embedded carbon nanotube/carbon flakes arrays for flexible solid-state zinc-air batteries. *Carbon* **2019,** *142*, 379-387.
251. Jin, Q.; Ren, B.; Chen, J.; Cui, H.; Wang, C., A facile method to conduct 3D self-supporting Co-FeCo/N-doped graphene-like carbon bifunctional electrocatalysts for flexible solid-state zinc air battery. *Appl. Catal. B Environ.* **2019,** *256*, 117887.
252. Liu, T.; Mou, J.; Wu, Z.; Lv, C.; Huang, J.; Liu, M., A facile and scalable strategy for fabrication of superior bifunctional freestanding air electrodes for flexible zinc–air batteries. *Adv. Funct. Mater.* **2020,** *30* (36), 2003407.
253. Zhu, L.; Zheng, D.; Wang, Z.; Zheng, X.; Fang, P.; Zhu, J.; Yu, M.; Tong, Y.; Lu, X., A confinement strategy for stabilizing ZIF-derived bifunctional catalysts as a benchmark cathode of flexible all-solid-state zinc–air batteries. *Adv. Mater.* **2018,** *30* (45), 1805268.
254. Chamran, F.; Hong-Seok, M.; Dunn, B.; Chang-Jin, C. J. K. In *Zinc-air microbattery with electrode array of zinc microposts*, 2007 IEEE 20th International Conference on Micro Electro Mechanical Systems (MEMS), 21-25 Jan. 2007; pp 871-874.
255. Armutlulu, A.; Fang, Y.; Kim, S.; Ji, C.; Allen, S.; Allen, M., High-current zinc-air microbattery based on a micromachined multilayer lateral metallic scaffold. *Proc. of PowerMEMS* **2010**, 107-110.

256. Zhu, M.; Wang, X.; Tang, H.; Wang, J.; Hao, Q.; Liu, L.; Li, Y.; Zhang, K.; Schmidt, O. G., Antifreezing Hydrogel with High Zinc Reversibility for Flexible and Durable Aqueous Batteries by Cooperative Hydrated Cations. *Adv. Funct. Mater.* **2020,** *30* (6), 1907218.
257. Huang, Y.; Wang, Y.; Tang, C.; Wang, J.; Zhang, Q.; Wang, Y.; Zhang, J., Atomic Modulation and Structure Design of Carbons for Bifunctional Electrocatalysis in Metal–Air Batteries. *Adv. Mater.* **2019,** *31* (13), 1803800.
258. Chen, Y.; Ji, S.; Zhao, S.; Chen, W.; Dong, J.; Cheong, W.-C.; Shen, R.; Wen, X.; Zheng, L.; Rykov, A. I.; Cai, S.; Tang, H.; Zhuang, Z.; Chen, C.; Peng, Q.; Wang, D.; Li, Y., Enhanced oxygen reduction with single-atomic-site iron catalysts for a zinc-air battery and hydrogen-air fuel cell. *Nat. Commun.* **2018,** *9* (1), 5422.
259. Han, X.; Li, X.; White, J.; Zhong, C.; Deng, Y.; Hu, W.; Ma, T., Metal–Air Batteries: From Static to Flow System. *Adv. Energy Mater.* **2018,** *8* (27), 1801396.
260. Cao, Z.-q.; Wu, M.-z.; Hu, H.-b.; Liang, G.-j.; Zhi, C.-y., Monodisperse Co9S8 nanoparticles in situ embedded within N, S-codoped honeycomb-structured porous carbon for bifunctional oxygen electrocatalyst in a rechargeable Zn–air battery. *NPG Asia Materials* **2018,** *10* (7), 670-684.
261. Cheng, F.; Chen, J., Metal–air batteries: from oxygen reduction electrochemistry to cathode catalysts. *Chem. Soc. Rev.* **2012,** *41* (6), 2172-2192.
262. Weinrich, H.; Durmus, Y. E.; Tempel, H.; Kungl, H.; Eichel, R.-A., Silicon and Iron as Resource-Efficient Anode Materials for Ambient-Temperature Metal-Air Batteries: A Review. *Materials* **2019,** *12* (13).
263. Cai, P.; Peng, X.; Huang, J.; Jia, J.; Hu, X.; Wen, Z., Covalent organic frameworks derived hollow structured N-doped noble carbon for asymmetric-electrolyte Zn-air battery. *Science China Chemistry* **2019,** *62* (3), 385-392.
264. Cai, P.; Li, Y.; Chen, J.; Jia, J.; Wang, G.; Wen, Z., An Asymmetric-Electrolyte Zn-Air Battery with Ultrahigh Power Density and Energy Density. *ChemElectroChem* **2018,** *5* (4), 589-592.
265. Yu, X.; Gross, M. M.; Wang, S.; Manthiram, A., Aqueous Electrochemical Energy Storage with a Mediator-Ion Solid Electrolyte. *Adv. Energy Mater.* **2017,** *7* (11), 1602454.
266. Lin, C.; Kim, S.-H.; Xu, Q.; Kim, D.-H.; Ali, G.; Shinde, S. S.; Yang, S.; Yang, Y.; Li, X.; Jiang, Z.; Lee, J.-H., High-voltage asymmetric metal–air batteries based on polymeric single-Zn2+-ion conductor. *Matter* **2021,** *4* (4), 1287-1304.
267. Hasegawa, M.; Ishigami, T.; Ishii, J.; Sugiura, K.; Fujii, M., Solution-processable transparent polyimides with low coefficients of thermal expansion and self-orientation behavior induced by solution casting. *Eur. Polym. J.* **2013,** *49* (11), 3657-3672.
268. Lin, D.; Zhuo, D.; Liu, Y.; Cui, Y., All-Integrated Bifunctional Separator for Li Dendrite Detection via Novel Solution Synthesis of a Thermostable Polyimide Separator. *J. Am. Chem. Soc.* **2016,** *138* (34), 11044-11050.
269. Zhu, M.; Hu, J.; Lu, Q.; Dong, H.; Karnaushenko, D. D.; Becker, C.; Karnaushenko, D.; Li, Y.; Tang, H.; Qu, Z.; Ge, J.; Schmidt, O. G., A Patternable and In Situ Formed Polymeric Zinc Blanket for a Reversible Zinc Anode in a Skin-Mountable Microbattery. *Adv. Mater.* **2021,** *33* (8), 2007497.
270. Thirukumaran, P.; Atchudan, R.; Parveen, A. S.; Kalaiarasan, K.; Lee, Y. R.; Kim, S.-C., Fabrication of ZnO nanoparticles adorned nitrogen-doped carbon balls and their application in photodegradation of organic dyes. *Sci. Rep.* **2019,** *9* (1), 19509.
271. Yuan, S.; Bao, J. L.; Wei, J.; Xia, Y.; Truhlar, D. G.; Wang, Y., A versatile single-ion electrolyte with a Grotthuss-like Li conduction mechanism for dendrite-free Li metal batteries. *Energy Environ. Sci.* **2019,** *12* (9), 2741-2750.
272. Liu, W.; Lee, S. W.; Lin, D.; Shi, F.; Wang, S.; Sendek, A. D.; Cui, Y., Enhancing ionic conductivity in composite polymer electrolytes with well-aligned ceramic nanowires. *Nat. Energy* **2017,** *2* (5), 17035.

273. Dubin, S.; Gilje, S.; Wang, K.; Tung, V. C.; Cha, K.; Hall, A. S.; Farrar, J.; Varshneya, R.; Yang, Y.; Kaner, R. B., A One-Step, Solvothermal Reduction Method for Producing Reduced Graphene Oxide Dispersions in Organic Solvents. *ACS Nano* **2010,** *4* (7), 3845-3852.
274. Shuck, C. E.; Sarycheva, A.; Anayee, M.; Levitt, A.; Zhu, Y.; Uzun, S.; Balitskiy, V.; Zahorodna, V.; Gogotsi, O.; Gogotsi, Y., Scalable Synthesis of Ti3C2Tx MXene. *Adv. Eng. Mater.* **2020,** *22* (3), 1901241.
275. Naguib, M.; Kurtoglu, M.; Presser, V.; Lu, J.; Niu, J.; Heon, M.; Hultman, L.; Gogotsi, Y.; Barsoum, M. W., Two-Dimensional Nanocrystals Produced by Exfoliation of Ti3AlC2. *Advanced Materials* **2011,** *23* (37), 4248-4253.
276. Wagh, N. K.; Kim, D.-H.; Kim, S.-H.; Shinde, S. S.; Lee, J.-H., Heuristic Iron–Cobalt-Mediated Robust pH-Universal Oxygen Bifunctional Lusters for Reversible Aqueous and Flexible Solid-State Zn–Air Cells. *ACS Nano* **2021,** *15* (9), 14683-14696.
277. Shinde, S. S.; Lee, C. H.; Jung, J.-Y.; Wagh, N. K.; Kim, S.-H.; Kim, D.-H.; Lin, C.; Lee, S. U.; Lee, J.-H., Unveiling dual-linkage 3D hexaiminobenzene metal–organic frameworks towards long-lasting advanced reversible Zn–air batteries. *Energy Environ. Sci.* **2019,** *12* (2), 727-738.
278. Tam, T. V.; Kang, S. G.; Kim, M. H.; Lee, S. G.; Hur, S. H.; Chung, J. S.; Choi, W. M., Novel Graphene Hydrogel/B-Doped Graphene Quantum Dots Composites as Trifunctional Electrocatalysts for Zn-Air Batteries and Overall Water Splitting. *Adv. Energy Mater.* **2019,** *9* (26), 1900945.
279. Guo, Y.; Yuan, P.; Zhang, J.; Xia, H.; Cheng, F.; Zhou, M.; Li, J.; Qiao, Y.; Mu, S.; Xu, Q., Co2P–CoN Double Active Centers Confined in N-Doped Carbon Nanotube: Heterostructural Engineering for Trifunctional Catalysis toward HER, ORR, OER, and Zn–Air Batteries Driven Water Splitting. *Adv. Funct. Mater.* **2018,** *28* (51), 1805641.
280. Wagh, N. K.; Shinde, S. S.; Lee, C. H.; Jung, J.-Y.; Kim, D.-H.; Kim, S.-H.; Lin, C.; Lee, S. U.; Lee, J.-H., Densely colonized isolated Cu-N single sites for efficient bifunctional electrocatalysts and rechargeable advanced Zn-air batteries. *Appl. Catal. B* **2020,** *268*, 118746.
281. Wu, Z.; Wang, H.; Xiong, P.; Li, G.; Qiu, T.; Gong, W.-B.; Zhao, F.; Li, C.; Li, Q.; Wang, G.; Geng, F., Molecularly Thin Nitride Sheets Stabilized by Titanium Carbide as Efficient Bifunctional Electrocatalysts for Fiber-Shaped Rechargeable Zinc-Air Batteries. *Nano Letters* **2020,** *20* (4), 2892-2898.
282. Shinde, S. S.; Lee, C. H.; Yu, J.-Y.; Kim, D.-H.; Lee, S. U.; Lee, J.-H., Hierarchically Designed 3D Holey C2N Aerogels as Bifunctional Oxygen Electrodes for Flexible and Rechargeable Zn-Air Batteries. *ACS Nano* **2018,** *12* (1), 596-608.
283. Liu, P.; Gao, D.; Xiao, W.; Ma, L.; Sun, K.; Xi, P.; Xue, D.; Wang, J., Self-Powered Water-Splitting Devices by Core–Shell NiFe@N-Graphite-Based Zn–Air Batteries. *Adv. Funct. Mater.* **2018,** *28* (14), 1706928.
284. Li, Y.; Zhong, C.; Liu, J.; Zeng, X.; Qu, S.; Han, X.; Deng, Y.; Hu, W.; Lu, J., Atomically Thin Mesoporous Co3O4 Layers Strongly Coupled with N-rGO Nanosheets as High-Performance Bifunctional Catalysts for 1D Knittable Zinc–Air Batteries. *Adv. Mater.* **2018,** *30* (4), 1703657.
285. Shinde, S. S.; Jung, J. Y.; Wagh, N. K.; Lee, C. H.; Kim, D.-H.; Kim, S.-H.; Lee, S. U.; Lee, J.-H., Ampere-hour-scale zinc–air pouch cells. *Nat. Energy* **2021,** *6* (6), 592-604.